

POLITECNICO DI MILANO

Semi-Analytical Mono-Dimensional Modelling of Cathodeless Plasma Thrusters

**School of Industrial and Information Engineering
Department of Aerospace Science and Technology
MSC in Space Engineering**

Author:
Matteo GUAITA
920513

Supervisor:
Prof. Michèle LAVAGNA
Coadvisors:
Mirko MAGAROTTO
Marco MANENTE

Abstract

This thesis concerns the development and description of mono-dimensional and semi-analytical models capable of determining the characteristics and propulsive properties of cathodeless plasma thrusters. In particular two algorithms for the description of the plasma source of such thrusters are presented and developed: a mono-dimensional one, and a volume averaged one. Three different models for the plasma expansion in the magnetic nozzle are also described and integrated with the source models. Finally four different criteria used to determine the detachment of the plasma from the magnetic field lines, and an algorithm capable of calculating the divergence of the plasma beam and the consequent decrease in the thrust, are also proposed.

All of the proposed models are verified and compared between themselves, allowing a critical analysis of their capabilities and characteristics. The combinations of the algorithms are then validated against experimental data taken from three different cathodeless plasma thrusters, in order to verify the qualitative and quantitative accuracy of the developed models. Finally a sensitivity analysis on a range of design parameters of the main propulsive properties and plasma characteristics of a cathodeless plasma thruster is carried out by means of the presented algorithms.

Sommario

Questa tesi tratta lo sviluppo e la presentazione di modelli monodimensionali e semianalitici per la descrizione di motori al plasma privi di catodi. In particolare vengono presentati e sviluppati due algoritmi per la modellazione della sorgente dove viene prodotto il plasma: un modello monodimensionale, ed uno a nodo singolo. Inoltre vengono delineati tre modelli differenti per la descrizione dell'espansione del plasma nell'ugello magnetico, che vengono poi integrati con gli algoritmi per la modellazione della sorgente. Infine si propongono quattro criteri utilizzati per la determinazione del punto di separazione tra le particelle del plasma e le linee di campo magnetico, insieme ad un algoritmo per il calcolo della divergenza del flusso di plasma ed il conseguente calo nella spinta prodotta.

Tutti i modelli proposti sono stati verificati e confrontati tra di loro, permettendo un'analisi critica delle loro caratteristiche e capacità. La combinazione degli algoritmi è poi stata validata tramite il confronto con dati sperimentali tratti da tre motori al plasma differenti, in modo da determinarne la corrispondenza qualitativa e quantitativa con i dati reali. Infine è stata prodotta un'analisi di sensitività, sulle variabili di progetto, delle principali proprietà propulsive dei motori considerati e delle caratteristiche del plasma prodotto, utilizzando i modelli presentati.

Ringraziamenti

Un vecchio saggio un giorno mi ha detto che la tesi non è altro che una elaborata e laboriosa scusa per ringraziare le persone che si amano, che ci hanno accompagnato, e ci accompagneranno, in un lungo percorso di crescita. Non so quanto le istituzioni sarebbero d'accordo con questa affermazione, ma io voglio comunque cogliere l'occasione per porgere quei meritatissimi ringraziamenti di cui non sono forse stato abbastanza prodigo in questi anni. Per *par condicio*, per camuffare il mio imbarazzo di fronte a questa manifestazione di affetto, e prima che qualcuno si monti eccessivamente la testa, però, permettetemi anche di elencare coloro nonostante i quali ho raggiunto questo traguardo.

Grazie a...

Il più grande e sincero grazie va alla mia famiglia. Grazie per avermi cresciuto e plasmato nell'uomo che sono, di cui spero voi siate fieri almeno quanto lo sono io. Grazie per avermi sopportato, per avermi sostenuto quando necessario e per avermi permesso di crescere coi miei soli mezzi quando opportuno. Grazie a mia madre per il suo infallibile senso della giustizia e del dovere, per tutti i piccoli e grandi impegni che si prende ogni giorno per permetterci di crescere con felicità e serenità, e per il tiramisù più buono del mondo. Grazie a mio padre per l'inturbabile serenità ed allegria con cui affronta ogni giornata. Anche quelle in cui si parla di spirulina. Grazie per avermi trasmesso il tuo approccio alla vita leggero, scientifico e curioso che è alla base di tutti i miei successi. Voglio ringraziare anche Tommaso, per avermi aperto la strada con il suo esempio e con la sua precisione e per avermela alleggerita con le sue prese in giro. E poi dove avrei scritto questa tesi se fosse ancora a Milano? Infine devo ringraziare Giacomo, più per sfinimento che per merito: non so se mi sarei ricordato di scrivere questi ringraziamenti senza di lui. Grazie per le discussioni assurde sui tombini di Barcellona, grazie per la tua opinione sempre fastidiosamente più corretta della mia, grazie per il tuo senso dell'umorismo e per la tua compagnia in questo mondo di *boomer*.

Vorrei ringraziare anche tutti gli amici che mi hanno accompagnato in questo percorso. Grazie ad Ale per avermi insegnato il significato della Determinazione, non so se oggi starei tagliando questo traguardo se non ti avessi conosciuta anni fa. Grazie al Mane per avermi insegnato l'Onestà e grazie a Gueri per avermi insegnato l'Entusiasmo. Grazie ad Emi per avermi dimostrato cosa significhi l'Amicizia ed a Jack per avermi aiutato a scoprire l'Avventura. Grazie a Tia per la Costanza, a Giada per l'Affetto, a Marco per l'Allegria, a Teo per l'Eloquenza, a Gloria per il Sorriso, ad Alice per l'Energia, e a Dave per l'Ascolto. Ringrazio Andrea per la sua incrollabile ed interminabile presenza nonostante i 500 metri che ci separano oggi, ed i 14'000 chilometri che ci hanno diviso in passato. Ringrazio Marta per la sua immutabile fiducia in quello che sono e nelle mie possibilità. Grazie per aver sempre visto la mia versione migliore, anche quando io stesso facevo fatica a scorgerla. Infine grazie agli amici di serie b: Sergio, Giovanni, Ilaria ed anche Massi. Grazie per le serate spensierate e per i discorsi seri. Grazie a Sergio per l'onestà e la determinazione che pone in tutto ciò che fa, a Giovanni per la passione e l'imprevedibilità che lo caratterizzano, ed alla Borgo per il suo affetto e le sue premure.

Un doveroso ringraziamento va anche a Mirko e a Marco che mi hanno seguito ad ogni passo

di questo lavoro, consigliandomi e guidandomi lungo il percorso. Senza i vostri insegnamenti e le vostre correzioni di rotta questa tesi non sarebbe mai diventata quello che è oggi. Infine ringrazio la professoressa Lavagna per avermi dato l'opportunità di lavorare su di un argomento che da anni mi appassiona.

Nonostante...

Sostenere che tutti coloro che ho ringraziato siano stati solo un punto di forza del lavoro svolto sarebbe un'utopia. Questa tesi è stata completata nonostante le partite di *Dota* di Giacomo nell'altra stanza, nonostante l'imperativa necessità di saldare immediatasubito le cuffie, nonostante gli "allora li hai scritti i ringraziamenti?". Ogni parola è stata composta attraverso le inondazioni di alghe e di oscillatori marini che provenivano dalla sala. Ho dovuto combattere con gli stracci e le aspirapolveri pronti a scacciarmi dalla mia postazione di lavoro e ho dovuto lasciare a metà alcuni lunghi integrali perché "Matteo! Si è incatagnato di nuovo il tubo della botte!". Meglio non nominare neanche l'ipocondria contagiosa di Tommaso prima che uno dei due sviluppi qualche altra patologia.

Questa tesi è arrivata a termine nonostante il frigorifero perennemente munito di birra dell'Ale e nonostante i suoi continui tentativi di avvelenarmi col caffè. Con ogni probabilità anche la perdita di neuroni causata dalla compagnia del Mane e di Emi, lo stato d'ansia perenne generato dalla consapevolezza di abitare nella stessa città di Sergio, e l'impegno eccessivo necessario a spiegare a Giovanni come vive una persona normale non hanno aiutato. Nel caso della Borgo posso solo invocare la perdita di produttività dovuta ai lunghi silenzi passati a guardarci negli occhi poiché non avevamo argomenti in comune. E poi come dimenticare il sole e la *Grignetta* che quotidianamente facevano capolino alla mia finestra, le polente cotte nel té della Laura, e le insistenti ed allettanti proposte di fare un giro all'aria aperta di Marta e Marco?

A tutti voi un ultimo e grande Grazie, perché forse in assenza di tutto ciò questa tesi sarebbe venuta un po' più precisa ed un po' più bella, ma io non mi sarei mai divertito altrettanto a scriverla e, in mancanza di persone con cui dividerla, non ne sarei altrettanto fiero. Un ultimo Grazie perché senza tutto ciò che mi date quotidianamente oggi non sarei la persona che sono.

Contents

Abstract	iii
Sommario	v
Ringraziamenti	vii
Contents	x
List of Figures	xii
List of Tables	xiii
List of Symbols	xiv
1 Introduction	1
1.1 Cathodeless Thrusters	1
1.2 Modelling of the cathodeless plasma thruster	4
1.2.1 Fluid Codes	5
1.2.2 Kinetic Codes	5
1.2.3 Particle Codes	5
1.2.4 Hybrid Codes	6
1.2.5 Semi-Analytical Source Models	6
1.2.6 Semi-Analytical Magnetic Nozzle Models	7
1.3 Work Statement	7
2 Nozzle and Source Models	9
2.1 Magnetic Nozzle Models	9
2.1.1 Laffeur Model	10
2.1.2 Martinez-Sanchez Model	11
2.1.3 Modified Martinez-Sanchez Model	20
2.1.4 Detachment Criteria	21
2.1.5 Divergence Efficiency	26
2.2 Plasma Source Models	27
2.2.1 Laffeur Source Model	27
2.2.2 Global Source Model	33
3 Model Verification and Comparison	49
3.1 Verification	49
3.1.1 Laffeur Models	49
3.1.2 Martinez-Sanchez Model	50
3.1.3 Modified Martinez-Sanchez Model	54
3.1.4 Global Source Model	56

3.2	Comparison	59
3.2.1	Source Models	59
3.2.2	Nozzle Models	61
3.2.3	Detachment Criteria	65
4	Model Validation against Experiments	69
4.1	Thruster A	69
4.2	Thruster B	72
4.3	Thruster C	77
4.4	Validation Results	81
5	Sensitivity to Design Parameters	83
6	Conclusions and Future Developments	95
6.1	Conclusions	95
6.2	Future Developments	96
	Bibliography	100

List of Figures

1.1	Typical structure of a cathodeless plasma thruster.	2
2.1	Graphical representation of the ion distribution function before and after the minimum in the maximum magnetic moment.	13
2.2	Graphical representation of the electron distribution function for particles with an initial energy lower or higher than the total potential drop.	14
2.3	Geometry of the magnetic field produced by rings of radial magnets.	42
3.1	Comparison between the computed results and the ones presented in Reference [1]	50
3.2	Normalized magnetic induction (β) and corresponding adimensional potential (Φ) along the nozzle.	51
3.3	Comparison between the computed normalized plasma density and velocity and the data-points of Ref. [2].	52
3.4	Kinetic energy fluxes along the nozzle.	53
3.5	Verification of Equation 3.2.	54
3.6	Normalized electron specific kinetic energy and average perpendicular velocity along the nozzle.	54
3.7	Comparison between the outputs of the Modified Martinez-Sanchez and the Martinez-Sanchez models.	55
3.8	Comparison between the velocities computed by the MS and MMS models. . .	56
3.9	Density ratios between the source axis and the outer radial walls computed with different perpendicular diffusion coefficients.	57
3.10	Comparison between the computed plasma radial profile and the experimental data.	58
3.11	Comparison between the different ionization and elastic scattering reaction rates found in the literature.	59
3.12	Plasma properties predicted by the Lafleur source model.	60
3.13	Comparison between the products of the plasma density and electron temperature found by the source models.	61
3.14	Properties of the expanding plasma along the nozzle according to nozzle models.	62
3.15	Comparison between the plasma thrust forces computed by the Lafleur, MS, and MMS models.	64
3.16	The divergence efficiency and its effect on the thrust.	65
3.17	Detachment locations found by the four detachment criteria proposed along the magnetic nozzle, and the corresponding thrust.	66
4.1	Comparison between the computed and measured plasma properties inside the plasma source of Thruster A.	71
4.2	Comparison between the computed and measured total thrust provided by Thruster A.	71
4.3	Specific impulse and thrust efficiency of Thruster A.	72

4.4	Magnetic geometry of Thruster B compared with the ideal magnetic nozzle obtained from a single current ring.	73
4.5	Comparison between the computed and measured plasma properties inside the plasma source of Thruster B.	74
4.6	Comparison between the computed thrust, without divergence efficiency, and the measured thrust for Thruster B.	75
4.7	Comparison between the computed thrust, with divergence efficiency, and the measured thrust for Thruster B.	76
4.8	Specific impulse and thrust efficiency of Thruster B	77
4.9	Comparison between the plasma properties in Thruster C computed by the presented models and a higher fidelity model.	78
4.10	Comparison between the computed thrust, without divergence efficiency, and the measured thrust for Thruster C.	80
4.11	Comparison between the computed thrust, without divergence efficiency, and the measured thrust for Thruster C.	81
4.12	Specific impulse and thrust efficiency of Thruster C	82
5.1	Behaviour of the plasma properties and propulsive characteristics as a function of the source radius (R_s).	84
5.2	Behaviour of the plasma properties and propulsive characteristics as a function of the source length (L_s).	85
5.3	Behaviour of the plasma density (n) in function of the source length (L_s) in the case of a strong confining magnetic field $B = 1500$ G.	86
5.4	Behaviour of the plasma properties and propulsive characteristics as a function of the exhaust radius (R_f).	87
5.5	Behaviour of the plasma properties and propulsive characteristics as a function of the mass flux.	88
5.6	Behaviour of the plasma properties and propulsive characteristics as a function of the magnetic field and the number of cusps.	89
5.7	Behaviour of the plasma properties and propulsive characteristics as a function of the total power (P_T) provided to the thruster.	90
5.8	Behaviour of the plasma properties and propulsive characteristics as a function of the ion temperature (T_i) in the plasma source.	91
5.9	Behaviour of the plasma properties and propulsive characteristics as a function of the temperature of the neutral particles (T_n) in the plasma source.	92
5.10	Local sensitivity (S) of the electron temperature (in blue), plasma density (in red) and total thrust (in green) on the design parameters.	94

List of Tables

1.1	Properties of existing cathodeless thruster prototypes	4
2.1	Adimensional variables and adimensionalisation parameters.	16
2.2	Expressions for the reaction rates and cross-sections of the considered reactions [3]	38
3.1	Thruster parameters used to validate the Lafleur models	50
3.2	Source parameters used to validate the computed plasma radial profile.	58
3.3	Thruster parameters used to compare the Global source model and the Lafleur Source model.	59
3.4	Plasma properties predicted by the source models for the thruster characterised in Table 3.3	60
3.5	Plasma parameters used to run the magnetic nozzle models	62
3.6	Plasma and magnetic nozzle parameters used to compare the detachment criteria.	66
3.7	Divergence efficiencies corresponding to each detachment criteria.	67
4.1	Characteristics of thruster A	70
4.2	Characteristics of Thruster B	72
4.3	Characteristics of Thruster C.	78
5.1	Nominal value and evaluation range of the design parameters.	83
5.2	Plasma characteristics and propulsive properties of the modelled thruster in nominal conditions.	84

List of Symbols

Uppercase

A	—	Plasma column cross-section.
A_{cusps}	—	Cusp loss area.
A_{eff}	—	Effective loss area.
A_s	—	Source area.
A_{th}	—	magnetic throat area.
B	—	Magnetic induction.
E_e	—	Electron specific kinetic energy.
E_i	—	Ion specific kinetic energy.
E_{tot}	—	Total kinetic energy.
F_{MN}	—	Thrust increment due to the magnetic nozzle.
F_n	—	Thrust due to the neutral particles.
F_{tot}	—	Total thrust.
K	—	Error weight.
K_{cx}	—	Charge exchange reaction rate.
K_{El}	—	Elastic scattering reaction rate.
K_{ex}	—	Excitation reaction rate.
K_{iz}	—	Ionization reaction rate.
K_L	—	Langevin scattering reaction rate.
L_s	—	Source length
M	—	Mach number.
M_{ex}	—	Mach number of the neutral particles at the exhaust.
M_{det}	—	Mach number of the plasma at detachment.
P_{abs}	—	Power absorbed by the plasma.
P_{ex}	—	Power lost through the exhaust.
P_{wall}	—	Power lost at the walls.
P_{react}	—	Power lost due to reactions and collisions.
P_T	—	Total input power.
$R_{95\%}$	—	Radius of the filed tube containing 95% of the mass flux inside the source.
R_{Ar}	—	Gas constant of Argon.
R_{cur}	—	Radius of curvature of the field line.
R_f	—	Radius of the exhaust hole.
R_r	—	Radius of the current ring producing the magnetic nozzle.
R_s	—	Source radius.
$S_{x/p}$	—	Sensitivity of the output x on the parameter p .
T_e	—	Electron temperature.
T_i	—	Ion temperature.
T_n	—	Temperature of the neutral species.

Lowercase

e	—	Elementary charge.
f	—	radial density distribution.
f_e	—	Electron distribution function, electrostatic force acting on ions and electrons.
f_i	—	Ion distribution function.
f_m	—	Magnetic force.
f_p	—	Pressure force.
h_L	—	Ratio between the plasma density at the centre of the source and at the axial extremities.
h_R	—	Ratio between the plasma density at the centre of the source and at the radial extremities.
j	—	Prescribed current density.
j_e	—	Electron current density.
j_i	—	Ion current density.
k	—	Boltzmann constant.
m_{Ar}	—	Argon mass.
m_e	—	Electron mass.
m_i	—	Ion mass.
m_R	—	Reduced mass.
n	—	Plasma density.
n_{4P}	—	Density of neutral atoms excited to the 4P orbital.
n_{4S}	—	Density of neutral atoms excited to the 4S orbital.
n_e	—	Electron density.
n_i	—	Ion density.
n_n	—	Neutral density.
\dot{n}	—	Density variation.
\dot{n}_{ex}	—	Density variation due to the exhaust of particles.
\dot{n}_{wall}	—	Density variation due to wall neutralization.
\dot{n}_{react}	—	Density variation due to plasma reactions.
p	—	Design parameter.
p_e	—	Electron pressure.
p_i	—	Ion pressure.
r	—	radial coordinate.
$r_{95\%}$	—	Radial coordinate of the field line containing 95% of the mass flux.
r_{ce}	—	Electron cyclotron radius.
r_{ci}	—	Ion cyclotron radius.
r_s	—	radial coordinate at which the fluid element left the source.
r_{ce}	—	Electron cyclotron radius.
t	—	Time.
u_b	—	Bohm velocity.
v	—	Plasma velocity.
v_e	—	Electron velocity.
v_g	—	Neutral gas velocity.
v_i	—	Ion velocity.
v_n	—	Velocity of neutral particles.
x	—	Model output.
\dot{y}	—	Number of reactions per second and unit volume.
z	—	Axial coordinate.

Greek letters

α	—	Inclination of the field lines.
α_0	—	Bohr atomic radius.
α_p	—	Polarizability.
β	—	Normalized magnetic induction.
δ	—	Dirac delta.
ϵ_{el}	—	Energy transferred in elastic collisions.
ϵ_{ex}	—	Excitation energy.
ϵ_{iz}	—	Ionization energy.
ε_{exp}	—	Expansion ratio of the physical nozzle.
$\dot{\epsilon}_e$	—	Specific electron kinetic energy flux.
$\dot{\epsilon}_i$	—	Specific ion kinetic energy flux.
γ	—	Specific heat ratio of Argon.
Γ_0	—	Total propellant particle flux.
μ_e	—	Electron magnetic moment.
μ_{em}	—	Maximum electron magnetic moment.
μ_{eT}	—	Minimum of the maximum electron magnetic moments.
μ_i	—	Ion magnetic moment.
μ_{im}	—	Maximum ion magnetic moment.
μ_{iT}	—	Minimum of the maximum ion magnetic moments.
η_d	—	Propellant utilisation efficiency.
η_{div}	—	Divergence efficiency.
η_{rf}	—	Wave coupling efficiency.
η_{th}	—	Thrust efficiency.
Φ	—	Electrostatic potential.
λ	—	Coefficient used to compute the radially averaged plasma density.
ν_e	—	Electron collision frequency.
ν_i	—	Ion collision frequency.
ψ	—	Field line constant.
Ψ_{out}	—	Normalized total potential drop.
ρ	—	Normalized radial coordinate.
σ	—	Cross-section.
ω_e	—	Electron cyclotron frequency.
ω_i	—	Ion cyclotron frequency.
θ_e	—	Angle defining the electron distribution function.
θ_i	—	Angle defining the ion distribution function.

Acronyms

ECR	—	Electron Cyclotron Resonance.
BC	—	Electro-Magnetic.
HPT	—	Helicon Plasma Thruster.
MN	—	Magnetic Nozzle.
MMS	—	Modified Martinez-Sanchez.
MS	—	Martinez-Sanchez.
VASIMR	—	Variable Specific Impulse Magnetoplasma Rocket.

Chapter 1

Introduction

1.1 Cathodeless Thrusters

The growth and new challenges that have characterised the space sector in recent years have led to a very active research activity in the electric propulsion field. In particular the search for technologies that could respond to the low volume, power, and complexity requirements of the nano-satellite field, as well as overcome the durability limits of the existing electric thrusters, has been a strong driver in the development of new propulsive solutions. Amongst these, cathodeless thrusters have received an increasingly optimistic attention. [4]

These thrusters are characterised by an exhaust that results, when averaged over the period of operation, free of charge, removing the need for an external neutralising cathode; and can be subdivided, according to the way in which the propelling plasma is accelerated, into gridded and magnetic nozzle thrusters. The former make use of polarized grids and employ an acceleration mechanism fundamentally similar to gridded ion thrusters: the plasma particles are drawn towards the exhaust by imposing an electrostatic potential difference between the plasma and the acceleration grids. In this case, however, the grid potential is alternated, so that both positive and negative particles are, in turn, ejected from the engine [5], [6]. The latter make use of magnetic nozzles: slowly diverging magnetic fields that, much like physical De Laval nozzles, convert the internal energy of the plasma into axially-directed kinetic energy [7]. They are therefore both cathodeless and electrodeless. In thrusters that make use of this acceleration principle the production of a dense and hot plasma is of primary importance, as the plasma enthalpy is the energy source that, through the magnetic nozzle, produces the thrust. These plasma characteristics are typically obtained by exciting the particles in a neutral gas with electromagnetic (EM) waves and promoting ionization by electron collision until a high density plasma is formed. Technologies adopting this mechanism are called cathodeless thrusters. [4]

The structure of cathodeless thrusters may be typically subdivided into three distinct sections, schematically represented in Figure 1.1: the propellant storage and feeding system, the plasma source, and the acceleration region. The propellant storage and feeding system is similar to those of classical electrical thrusters: a pressurised tank contains and drives a single, gaseous propellant towards the thruster inlet. The plasma source, where the propellant is ionized and the plasma produced, is typically composed of a dielectric cylindrical vessel into which the neutral gas flow is fed at a controlled rate. The source is surrounded by the RF-antenna capable of inducing the electromagnetic waves that excite and generate the plasma, and immersed in a confining magnetostatic field that can be produced by means of permanent magnets or electromagnets and that reduces diffusion to the outer walls and allows an efficient coupling of the EM wave with the particle dynamics. The choice between the type of magnets depends on the trade-off between a series of advantages and disadvantages: while permanent magnets require no electrical power to function they also result heavier and bigger, and cannot be switched off,

inducing a potentially disturbing magnetic field for the rest of the spacecraft [8]. The acceleration region contains, instead, a magnetic nozzle usually formed by the naturally-diverging field lines of the magnetic field in the source, that may also be surrounded by a physical De Laval nozzle that aids the expansion and thrust contribution of the part of the propellant that remain unionised [9]. In this region the plasma expands and accelerates axially into a plume that can be divided into two separate regions, according to the phenomena that govern the plasma dynamics. In the near region the geometry of the magnetic field and the collisions between the particles drive the plasma behaviour, while in the far region it is influenced mostly by the ambipolar diffusion and thermal pressure. Here detachment from the magnetic field is of paramount importance: if the plasma particles were to faithfully follow the closed field lines, in fact, they would necessarily invert their direction of motion and return to the thruster, resulting in a null momentum flux leaving the system, and in zero thrust. The function of the magnetostatic field generated by the magnets is, therefore, threefold: it allows the efficient transfer of the electromagnetic energy into the plasma, it confines the charged particles inside the source, decreasing diffusion to the outer walls and permitting the production of denser plasmas, and it provides the magnetic nozzle effect that converts the thermal energy into axial acceleration and thrust. [9] [4]

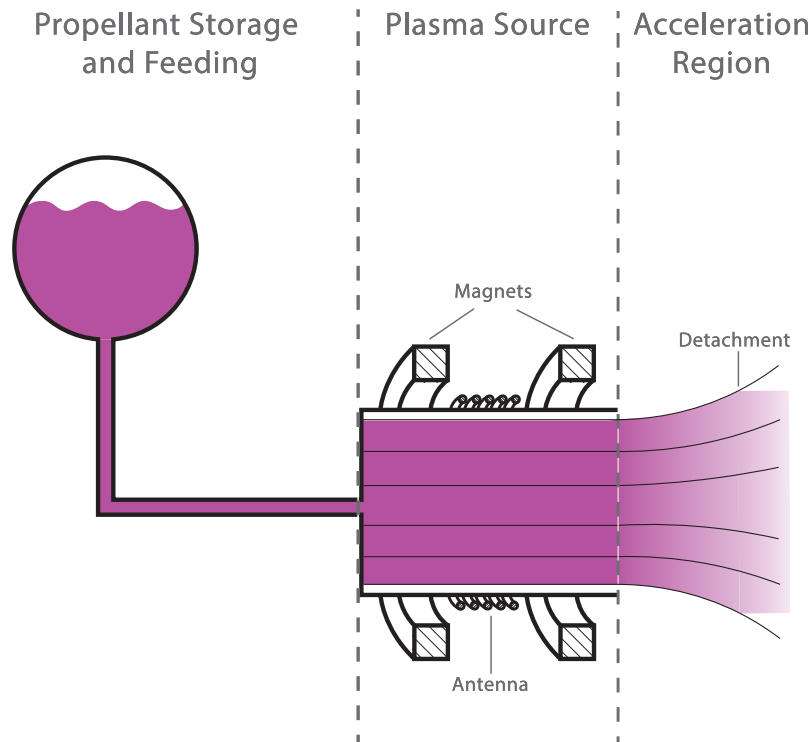


Figure 1.1: Typical structure of a cathodeless plasma thruster.

Cathodeless thrusters may be subdivided into Helicon Plasma Thrusters (HPTs) or Electron Cyclotron Resonance (ECR) plasma thrusters according to the frequency of the wave used to excite the plasma. Helicon waves are whistler waves that propagate inside a magnetically confined plasma. They are right handed, circularly polarized electromagnetic waves with a frequency in the MHz range, that rotate while propagating axially, leading the electrons on a helical trajectory and giving them their name. Helicon Plasma Thrusters make use of these waves to excite the free electrons in the propellant that then ionize the neutrals by colliding with them. These waves are of particular interest because the presence of a magnetic field allows their propagation within the plasma column, permitting a very efficient energy deposition. Indeed, the energy absorption rate results more than 1000 times faster than the one theoretically

attributable to collisional processes [10]. On the other hand, ECR thrusters make use of a microwave field in the GHz range to heat electrons by resonant absorption and to create a high density plasma. By inducing a wave with a frequency similar to the gyro-frequency of the electrons, in fact, it is possible to couple over 95% of the incident microwave power into the plasma [11]. The heated electrons then collide with the neutral particles ionizing them. [12]

Cathodeless thrusters possess a number of undeniable strengths: their structure and components are simple, resulting in low production costs, the absence of electrodes immersed and in direct contact with the plasma grants reduced erosion of the components and a long operational lifetime, and the globally neutral exhaust plume removes the necessity of a neutralising cathode. Furthermore the flexibility of these thrusters is of strong interest, as it allows them to work equally efficiently both at the power values required for CubeSat station-keeping (~ 50 W) [9] and at those necessary for interplanetary propulsion (~ 200 kW) [13]. The variety of utilizable propellants, such as Iodine [14], Argon, or Xenon [15], and the extensive range of possible mass fluxes (from 0.1 mgs^{-1} [9] to 100 mgs^{-1}) [13] also add to the flexibility and attractiveness of this technology. Finally, the plasma densities obtained, ranging from ion and electron densities of 10^{18} m^{-3} to 10^{20} m^{-3} [10], result in line, if not superior, to the ones obtained in thrusters that use electron discharges triggered by cathodes to produce the plasma. On the other hand the major disadvantage of cathodeless thrusters is the relatively low thrust efficiency that does not exceed 20% [11]. The electromagnetic power of the EM wave is not, in fact, completely converted into propulsive power: part of it is lost in the excitation of neutral atoms or in the process of ion neutralization. While step ionization is, in fact, the most efficient ionization procedure, it requires the intermediate production of excited neutral species. Before the full ionization can be reached the excited neutrals, however, may also either undergo radiative de-excitation or be ejected from the source. In the former case the excitation energy is lost under the form of an electromagnetic wave that is seldom reabsorbed by the plasma, in the latter the excitation energy doesn't contribute to the thrust production, as the neutral particle cannot be accelerated by the magnetic nozzle. Furthermore, the number of ionizations that occur inside the source is much greater than the number of ions ejected in the plume: before reaching the acceleration region, in fact, ions may either impact electrons inside the plasma or reach the source walls by diffusion, leading to neutralization. The amount of energy used to ionize the plasma typically becomes, therefore, roughly two times higher [8] than what would be strictly necessary, decreasing the thruster's efficiency. While a confining magnetostatic field reduces diffusion to the walls, mitigating this problem, ion neutralization remains one of the biggest loss mechanisms responsible of the low thrust efficiency. [9]

The first research on Helicon Plasma thrusters was carried out by Boswell and the space plasma propulsion group at the Australian National University in the early 2000s [16]. Today many other research centres and companies have given their contribution to the development of the technology. At the University of Padua a 50 W HPT has been designed and tested during the HPH.COM project [17], while a 1 kW thruster is being developed in the frame of the SAPERE-STRONG project [18]. Building on this knowledge a CubeSat propulsion platform, REGULUS, is also under development at Technology for Propulsion and Innovation SpA (T4i), a spin-off of the aforementioned university [9]. The University of Madrid, along with SENER Aeroespacial, is also designing and testing a 1 kW thruster during the HIPATIA project [19], while the universities of Stuttgart and Manchester have been working on an atmosphere-breathing HPT to be used in Very Low Earth Orbit [20]. The Tokyo University [21], the Massachusetts Institute of Technology [22], the Michigan Institute of Technology [23], and the Washington University have also worked and contributed to the HPT concept. [24]

ECR thrusters were first theorized in the 1960s by two groups of researchers: one guided by General Electric in the USA and one centred at the University of Tokyo [25]. Because of the massive and voluminous microwave sources, however, further research on this technology was interrupted until the 1990s. Today several research groups work on the ECR thruster concept.

	Technology	Propellant	Power [W]	Thrust [mN]	Specific Impulse [s]	Thrust Efficiency [%]
REGULUS [9]	HPT	Xenon	55	0.85	850	7
HPH.COM [17]	HPT	Argon	8	0.5	422	13
HPT-05M [19]	HPT	Xenon	450	5.6	1100	9
MINOTOR [27]	ECR	Xenon	30	0.98	993	16

Table 1.1: Properties of existing cathodeless thruster prototypes

At the Plasma dynamics & Electric Propulsion Laboratory at the University of Michigan a thruster that makes use of the Gasdynamic Mirror (ECR-GDM) for high thrust generation is being developed [26]. The ECR-GDM employs the magnetic mirror confinement system to heat the electrons by cyclotron resonance for a period of time and then accelerate the plasma with a magnetic nozzle to produce the thrust. The Physics and Instrumentation Department at Onera, instead, is currently performing research on an ECR plasma thruster in collaboration with the universities of Madrid and Giessen in the frame of the European MINOTOR project [27]. Other institutes, such as the University of Tokyo [28] and the Massachusetts Institute of Technology [29] are also contributing to the research on this technology [11]. To provide an initial sensibility on the plausible characteristics and performances of the cathodeless plasma thruster technology, the properties of the most recent and advanced prototypes developed have been summarised in Table 1.1.

Before analysing in deeper detail the modelling of a cathodeless plasma thruster, the main focus of this thesis, it is also worth mentioning the Variable Specific Impulse Magnetoplasma Rocket (VASIMR) under development by NASA. This ambitious projects aims at the realization of a high-power (200 kW), cathodeless, electric thruster for interplanetary missions, consisting of three main components: a low energy Helicon plasma source, an Ion Cyclotron-Resonance Heating (ICRH) section, and a magnetic nozzle. In the first section the fuel is ionized by the electrons, that are energized by the Helicon wave, while in the second stage the EM-power is deposited into the plasma by coupling it with the ion cyclotron frequency. Finally the ionized and heated propellant is accelerated and ejected through the magnetic nozzle. [13]

1.2 Modelling of the cathodeless plasma thruster

Describing and modelling the production and behaviour of the plasma inside a cathodeless plasma thruster is a complex and challenging task. A complete model should in fact be able to capture the plasma chemistry, including collision reactions and spontaneous de-excitation. It should also provide a self-consistent solution capable of conjugating the dynamics of the plasma particles with the electromagnetic fields externally imposed and induced by the presence and the movement of the particles themselves. Furthermore, a precise description of the expansion of the plasma in the magnetic nozzle requires the ability to compute the effects of various, non-Maxwellian particle populations, as well as the collisionless plasma cooling. It should also be mentioned that for a truly complete modelling of the thruster the electromagnetic wave propagation and energy deposition should be accurately described. This last point, however, is beyond the scope of this thesis, and it shall be simply assumed that a given fraction of the

electromagnetic energy is transferred to the plasma, while focusing instead on its dynamics and collisional processes. [30] [24]

Unsurprisingly, then, the most precise and effective models presented in the literature make use of numerical codes used to simulate the dynamics of the ions, electrons and neutrals that compose the plasma. These can be subdivided in fluid, kinetic and particle codes, while their combination, of increasingly common use, falls under the category of hybrid codes. Analytical or semi-analytical solutions, instead, become rapidly extremely complex when attempting to fully capture the physics of the problem. However, when simplified with appropriate hypotheses, they can offer a very useful insight on the physical mechanisms governing the plasma, as well as a rapid and effective, albeit rough, tool for a first design approach. [30]

1.2.1 Fluid Codes

This approach neglects the movement of individual particles, focusing on the behaviour of fluid elements. The plasma properties and their variation in space and time are obtained through the integration of the magnetohydrodynamic mass, momentum and energy balances. To do this, however, appropriate and approximated transport coefficients must be assumed, as well as a Maxwellian distribution of the particles, since choosing to ignore their individual dynamics means that all information on their distribution function is lost. As a consequence fluid models cannot account for non-local kinetics, which become increasingly important in low-pressure plasmas (below 1 mTorr) [30]. Despite this, fluid models are widely used because of their relatively low computational cost and consequent high speed, along with the capability of considering a large number of species without significantly lowering the code's velocity. [30] [24]

1.2.2 Kinetic Codes

This approach, based on a statistical mechanics model, obtains a self-consistent distribution function in the six-dimensional phase space for each considered species by solving simultaneously the Boltzmann and Maxwell equations. Once the ion and electron distribution functions are known the macroscopic plasma properties such as density, velocity and temperature may be obtained by computing their adequate moments. While this technique is capable of offering detailed simulations, capturing also the interactions between species whose distributions largely deviate from a Maxwellian one, the solution to the Boltzmann and Maxwell equations is not guaranteed, even with high computational times and power. For this reason kinetic codes are mainly applied under simplifying hypotheses, such as the reduction of the dimensions of the domain or the assumption that the magnetic field is unaltered by the particle dynamics. [31]

1.2.3 Particle Codes

Particle codes follow the trajectories of the single particles by integrating their dynamics, while simultaneously considering the presence of a self-consistent electromagnetic field, dependent on the position and motion of the particles themselves. Of course tracking all of the particles present in a plasma implies enormous computational costs and so mitigating techniques, such as implicit movers, longer ion time steps, different weights for electrons and ions or for low and high-energy particles, and code parallelization; along with limiting hypotheses, like the reduction of the dimensions of the domain or the assumption of fixed magnetic fields, are often adopted [30]. While still resulting more cumbersome than fluid codes these models grant a realistic and detailed description of many physical problems involving plasmas, and are particularly suited for the simulation of low-pressure discharges where the number of particles is relatively low and the presence of non-local effects may exclude the use of fluid models.

Particle In Cell (PIC) models are a subset of particle codes in which super-particles are used to group the particles of the same species in a single element of increased mass and charge,

thus reducing the computational cost. By then discretising the spatial domain by means of a grid the self-consistent electromagnetic field, and the consequent forces acting on the super-particles, may be computed. The time step and space resolution is constrained by instability problems and artificial heating, limiting the time-span and spatial dimensions that this method can tackle. Nevertheless these algorithms are finding ample success in the simulation of plasma sources and magnetic nozzles. [30] [32] [24]

1.2.4 Hybrid Codes

Hybrid codes use a Particle In Cell approach to model ion dynamics, while reducing the computationally expensive complexity of the electrons' motion by means of a fluid model. While reducing the overall accuracy of the code (especially due to the common use of isothermal or polytropic models for fluid closure [30]), this allows to reduce noticeably the computational time by greatly increasing the integration time-step without risking instabilities. Furthermore, while PIC codes must solve the Poisson equation for the electric field to implicitly impose quasi-neutrality, hybrid codes can assume it directly, reducing the number of computations. For these reasons, at present, these codes represent an appealing compromise in terms of accuracy, complexity and computational costs in the simulation of plasma sources and magnetic nozzles. [33]

1.2.5 Semi-Analytical Source Models

Modelling the phenomena of plasma production, diffusion and neutralization that take place in the source of a cathodeless plasma thruster with semi-analytical equations proves to be an extremely challenging task. Because of the nature of the magnetohydrodynamic equations an analytical solution can only be reached by means of strong simplifying hypotheses, typically including: stationary conditions, paraxial magnetostatic fields, axial symmetry that allows to reduce the dimensions of the domain, isothermality for fluid closure and absence of momentum exchange and loss via collisions [1]. In particular this last hypothesis is quite limiting, as the collisional nature of the plasma in the source is fundamental to its own production. Furthermore, the complexity of the mechanisms governing the cross-field diffusion and the radial profile of the plasma properties leads to the common utilisation of empirical and heuristic relations to compute these quantities. Boundary conditions are typically enforced by imposing the presence of a stationary plasma sheath and the Bohm criterion at the edges of the domain [34]. Ultimately these codes offer useful qualitative information on the behaviour of the plasma source, but should be used only for very rough quantitative considerations. [1]

A semi-analytical tool that has become popular recently in the modelling of many types of discharges is the global source model. It has, in fact, proven itself sufficiently precise for initial rough evaluations, albeit the many simplifying hypotheses that it implies [35]. In global, or volume averaged, codes the spatial domain is reduced to a single node by averaging plasma and field properties over the full volume considered. Indeed the spatial variation of the plasma properties is only considered, by means of empirical, heuristic or analytical solutions to the diffusion equations, in the imposition of the boundary conditions but is not, strictly speaking, an output of the model. The strong simplifications linked to a zero-dimensional domain and a uniform, paraxial magnetostatic field, allow the creation of a mathematical environment where the complex chemistry and physical processes that govern a plasma can be comfortably and directly tackled. The zero-dimensional balances of mass and energy, complete of the contributions of reactions, collisions and diffusion to the edges of the domain, can in fact be numerically integrated in time with small computational effort, yielding a relatively accurate qualitative and quantitative estimate of the density and temperature of the plasma. The plasma velocity, instead, is imposed through the Bohm criterion at the domain boundaries. meaning that the momentum conservation equation is not needed. [36] [37]

1.2.6 Semi-Analytical Magnetic Nozzle Models

Similarly to the description of the source, the analytical modelling of the behaviour of the plasma in the acceleration region is a complex and challenging task. However, thanks to the reduced density present in this region and the consequent reduction in the collisional frequency between the particles, it is possible to consider a collisionless and reactionless plasma [34] [2], allowing for a noticeable simplification of the governing equations. Typically the system is simplified by using a quasi-mono-dimensional model and a paraxial magnetostatic field, along with the assumptions of quasi-neutrality, no cross-field diffusion and no collisions. Two strategies are then commonly used to compute the plasma properties: either the analytical integration of the simplified continuity, momentum and energy balances [34], or the definition of the particles' distribution functions and the integration of their moments to obtain the average plasma properties [38]. In the former case fluid closure is obtained by assuming isothermality or by empirically deriving a polytropic index associated with the expansion. In the latter strong hypotheses on the initial distribution function of the particles (e.g. Maxwellian or mono-energetic) [2] result necessary to permit an analytical tracking of the distribution functions' evolution along the nozzle. Finally a location at which plasma detachment is assumed, and where the expansion is therefore terminated, is determined by means of a number of possible criteria. As will be later described in further detail, however, the complexity of the detachment phenomenon and its inherent bi-dimensionality means that a criterion which reaches the consensus of the scientific community has not been identified yet [39]. Analytical magnetic nozzle models can give, especially in the regions close to the source outlet, relatively precise qualitative and quantitative predictions of the plasma properties. The modelling of the dynamics in the far field, together with the definition of the detachment point and divergence efficiency, instead, result much more challenging and may have a noticeable influence on the uncertainties in the computation of a thruster's propulsive properties. The low computational cost and physical intuitiveness of these algorithms, however, make them exceptionally apt for qualitative considerations and for an initial design approach. [1] [2] [40]

1.3 Work Statement

The objectives of this thesis are strictly linked to the panorama of the existing modelling approaches used to describe cathodeless plasma thrusters. In particular a comparison and critical analysis of the semi-analytical source and magnetic nozzle models presented in the literature has been carried out. These models have then been extended, with the implementation and comparison of various detachment criteria and by proposing an algorithm used to compute the divergence efficiency of the plume. A global source model has also been implemented and assembled coherently with the magnetic nozzle models analysed, producing a full cathodeless plasma thruster model with low computational times, the presence of which, to our knowledge, is scarce in the literature. Finally, the outputs of the obtained algorithms have been compared with experimental data and considerations for the preliminary design have been formulated by analysing the behaviour of the propulsive properties (e.g. thrust, specific impulse, and thrust efficiency) in function of the main design variables (e.g. geometry of the source and intensity of the magnetostatic field).

The rest of the thesis is structured as follows. Chapter 2 presents the mathematical formulation of three magnetic nozzle models, coupled with four detachment criteria, as well as the proposed strategy for the divergence efficiency computation. Two source models are also described and implemented in this Chapter: an analytical and a global source model, that are then combined with the algorithms used to characterize the magnetic nozzle. In Chapter 3 the models are verified, compared and critically analysed. Chapter 4 presents the comparison between the numerical predictions of the developed algorithms and experimental data or

higher-fidelity models. Considerations for the preliminary design have been outlined in Chapter 5, while in Chapter 6 final conclusions are drawn, together with some remarks on the future development of the codes presented.

Chapter 2

Nozzle and Source Models

2.1 Magnetic Nozzle Models

The physical mechanism that allows a magnetic nozzle (MN) to increase the thrust provided by the exhaust of particles from a plasma source is the magnetic force exchanged between the azimuthal currents that develop inside the plume and the magnets that provide the thruster's magnetic field. As shown by Fruchtman et al. in Reference [7], in fact, the thrust given by a Helicon Plasma Thruster can be computed as the sum of the force due to the electron pressure at the rear of the plasma source ($p_e(0, r)$) and the magnetic force arising from the azimuthal currents (J_θ) and the radial component of the magnetostatic field (B_r) present in the plume.

$$F = \int_0^{R_s} p_e(0, r) 2\pi r dr + \int_V J_\theta B_r dV \quad (2.1)$$

Where F is the total thrust and R_s is the source radius. Fruchtman et al. also show that assuming an axis-symmetric domain, small ion inertia in comparison with radial electric and magnetic forces, and a paraxial magnetic field the contribution of the MN to the thrust (F_{MN}) may be rewritten as shown by Eq. 2.2.

$$F_{MN} = \int_{A_s}^{A_e} \langle p_e \rangle dA \quad (2.2)$$

Here A_s is the cross-sectional area of the plasma source, A_e the area of the plasma plume at the considered axial position and $\langle p_e \rangle$ the radially averaged electron pressure at this location. In this form it results apparent that the magnetic nozzle has a role very similar to the physical De Laval nozzle, with the important difference that in this case the average pressure is considered, and not just the one acting on the outer wall as is done in the traditional case. This is because the constraining factor that imposes the expanding electron trajectories is the magnetic field, that acts through the whole volume of the plume. It is here important to mention that while the magnetic force acting on the plasma particles is responsible for their axial acceleration cumulatively no work, and therefore no energy increase, can be exerted by the magnetic field, as by definition the Lorentz force is always perpendicular to the particles' velocity. Any increase of the electron or ion axial kinetic energy, therefore, happens strictly at the expense of the plasma's internal energy.

The plasma dynamics inside the nozzle, however, are more complex than the ones characterizing the flow of a neutral gas through a De Laval nozzle. While the lighter electrons are accelerated rapidly downstream, in fact, the heavier ions tend to fall back. To guarantee

quasi-neutrality, therefore, an ambipolar potential drop must arise [2], accelerating the ions axially and retarding the exhaust of the electrons, so that on a radial average no axial currents are developed in the nozzle. Overall the effect of the MN is to expand the plasma, and transfer its internal energy principally into the axial kinetic energy of the ions [34]. Any mathematical model wishing to describe a magnetic nozzle must take into account these fundamental physical processes.

2.1.1 Lafleur Model

This model, presented and demonstrated initially by Andersen et al. [41] and successively by Ahedo [34] and Lafleur [1], and which will be denominated for brevity the Lafleur MN model, offers a simple closed form solution to the mass, momentum and energy balances governing the plasma behaviour in a simply-divergent magnetic nozzle. The model leans on the following simplifying hypotheses:

- Quasi-mono-dimensional domain
- Stationary conditions
- Electron isothermality
- Magnetized particles
- Cold ions ($T_i = 0$)
- Massless electrons ($m_e = 0$)
- Quasi-neutral plasma ($n_i = n_e = n(z)$)
- Collisionless plasma
- Bohm velocity at the source exhaust

While these assumptions allow an analytical solution of the plasma dynamics, they also limit the model's accuracy and applicability. In particular the absence of electron cooling means that the thermal energy of the plasma does not decrease, leading to an infinite acceleration as the particles progress downstream. This means that if the expansion is not truncated at a given detachment point the resulting computed thrust is infinite. A detachment criterion is therefore mandatory in the utilisation of this model. Furthermore, the use of a quasi-mono-dimensional domain means that all the plasma properties are computed on the nozzle axis and assumed radially and azimuthally constant, so that they are only a function of the axial position ($n(z), \Phi(z), M(z)$). The electromagnetic fields and the plasma velocity are also restricted to a strictly axial dimension, and all the information on the azimuthal and radial behaviour are lost. The divergence of the plasma beam is therefore neglected, and only the increase of the plume cross-section ($A(z)$) is used to capture the multi-dimensional nature of the system. Moreover, as the particles flow downstream and the magnetic induction they encounter decreases, they become less and less magnetized and start to move perpendicularly to the magnetic field lines until complete detachment is reached and the electrons' and ions' motion becomes independent of the magnetic field. The assumption of magnetized particles, therefore, is accurate only in the region near the source exhaust. Finally, a collisionless plasma may not offer a precise description of the conditions at the beginning of the expansion, when the density and collision frequency are still similar to the ones found in the source. Some experiments have also shown that the initial condition of sonic velocity in the magnetic throat may be inaccurate [42].

Following Reference [34] and applying the described hypotheses the particle flux conservation (2.3), the Boltzmann distribution relation (2.4) and the total energy conservation along the nozzle axis (2.5) can be found.

$$A(0)n(0)M(0) = A(z)n(z)M(z) \tag{2.3}$$

$$n(z) = n(0) \exp\left(\frac{e\Phi}{kT_e}\right) \quad (2.4)$$

$$\frac{1}{2}M(z)^2 + \frac{e\Phi(z)}{kT_e} = \frac{1}{2}M(0)^2 \quad (2.5)$$

Where k is the Boltzmann constant, e the elementary charge, and T_e the electron temperature in Kelvin; while $n(z)$, $M(z)$ and $\Phi(z)$ are, respectively, the plasma density, Mach number and potential at the axial coordinate z . In particular the plasma Mach number uses the Bohm velocity $u_B = \sqrt{\frac{kT_e}{m_i}}$ to normalize the speed of the plasma particles, while the potential drop is fixed at zero at the source exhaust. Using Equations 2.3 and 2.4 to express the normalized potential as a function of the plume cross-section and the plasma Mach number. and substituting it into Equation 2.5 the Mach number can be linked directly to the axially-dependent area.

$$\frac{1}{2}(M(z)^2 - 1) - \log(M(z)) = \log\left(\frac{A(z)}{A_s}\right) \quad (2.6)$$

Where the hypothesis of a unitary Mach number at the source exhaust has been utilised. Given an axial coordinate and the corresponding cross-section of the exhaust plume, then, the plasma Mach number found there may be computed using Equation 2.6. Finally, Lafleur has demonstrated that the total thrust granted only by the accelerated plasma and not by remaining neutral particles (F_{plasma}) may be obtained by applying Equation 2.7 [1].

$$F_{plasma} = n_0 k T_e A_s \left(1 + \frac{(M_{det} - 1)^2}{2M_{det}}\right)^2 \quad (2.7)$$

Where n_0 is the maximum plasma density found inside the source, and M_{det} is the Mach number found at the detachment point.

2.1.2 Martinez-Sanchez Model

This model, proposed by Martinez-Sanchez et al. [2], calculates self-consistently the ion and electron distribution functions and the ambipolar electric field throughout a convergent-divergent magnetic nozzle. It captures the collisionless cooling of electrons and yields the full evolution of the properties of the two species, overcoming many of the limits of the previous model. For brevity this model may be referred to as the MS model. The model is based on the following hypotheses and constraints:

- Quasi-mono-dimensional domain
- Magnetic profile starting and ending at zero intensity, with a peak in the middle corresponding to the throat
- Magnetized electrons and ions
- Stationary conditions
- Maxwellian electron distribution at the nozzle entrance
- Existence of a trapped electron population in a portion of the nozzle, arranged in a Maxwellian distribution

- Mono-energetic, isotropic ion distribution at the nozzle entrance
- Quasi-neutrality along the nozzle
- Prescribed net current through the nozzle
- Collisionless plasma

The consequences of the use of a quasi-mono-dimensional domain are very similar to the ones described for the Lafleur MN model: plasma quantities are determined on the nozzle axis and are assumed constant in the other two dimensions, and the electromagnetic fields are assumed to be paraxial, ignoring their radial components. In this case, however, the perpendicular components of the particles' velocities are captured, and allow the computation of the perpendicular temperatures and pressures. Again, the beam divergence is neglected, while its cross-section is computed as a function of the axial position. The assumptions of a collisionless and completely magnetized plasma have the same limitations as previously described, while the capability of the model of capturing electron cooling means that a detachment criteria is not strictly required, as the particles' speed and the total thrust reach an asymptote as they expand to infinity. Finally, the fact that at the source exhaust the ions are assumed mono-energetic and isotropically distributed in the velocity space is quite a light imposition as, in any case, the ion distribution will approach a mono-energetic beam as they advance along the nozzle. The hypothesis of a Maxwellian electron distribution at the nozzle inlet, instead, while necessary for an analytical approach, is more limiting as it has been shown that the presence of different electron populations may have a noticeable effect on the performance of the thruster [43]. Moreover, the existence of the trapped electron population is postulated, but its formation mechanism is not captured. While the presence of these electrons has been confirmed by various experiments [2] [38], the way that they influence the distribution function is still a matter of debate, meaning that the assumption of a full Maxwellian distribution must be considered a source of uncertainties.

The ion distribution function, at the beginning of the expansion, may then be written as follows:

$$f_i = \frac{m_i n_\infty}{4\pi} \left(\frac{m_i}{2E_{i\infty}} \right)^{\frac{1}{2}} \delta(E_i - E_{i\infty}) \quad (2.8)$$

Where f_i is the ion distribution function, m_i the ion mass, n_∞ and $E_{i\infty}$ the ion density and energy at the hypothetical upstream reservoir where the magnetic field is null, and E_i the ion energy at which to evaluate the ion population. Finally δ is the Dirac delta. The distribution function is normalised so that the initial condition is respected: $n_\infty = \iiint f_i d^3v$. As the ions proceed downstream this distribution function will be altered by the magnetic mirror formed by the converging magnetic field lines, removing the ions with a lower axial velocity and bouncing them back towards the source. Invoking the conservation of the first adiabatic invariant, in fact, the maximum possible value at a given axial coordinate of the ion magnetic moment (μ_{im}) may be found using Equation 2.9. This condition is found in those ions that have a null component of their velocity parallel to the magnetic field because they have converted it all, thanks to the Lorentz force acting on them, into the azimuthal direction. Any ion with an initial magnetic moment higher than this maximum will have already been reflected upstream, and will never reach the considered location in the nozzle.

$$\mu_{im} = \frac{E_{i\infty} - e\Phi}{B} \quad (2.9)$$

Where B is the magnetic induction and Φ the electric potential, considered 0 at the reservoir and monotonously decreasing along the nozzle. Because of the expected behaviour of the

electric and magnetic fields μ_{im} will have a minimum somewhere along the convergent of the nozzle, designated with the suffix T. Upstream of this point ions with magnetic moments between the local μ_{im} and μ_{iT} will be found, while downstream of it only the ions with magnetic moments below μ_{iT} will remain, as all the others will have been bounced back. This depicts an ion distribution that is a spherical shell in the velocity space, delimited by the angle θ_i that cuts out the portion of ions with a low parallel component of the velocity, as shown in Figure 2.1. At each point along the expansion the angle θ_i may be computed using Equation 2.10.

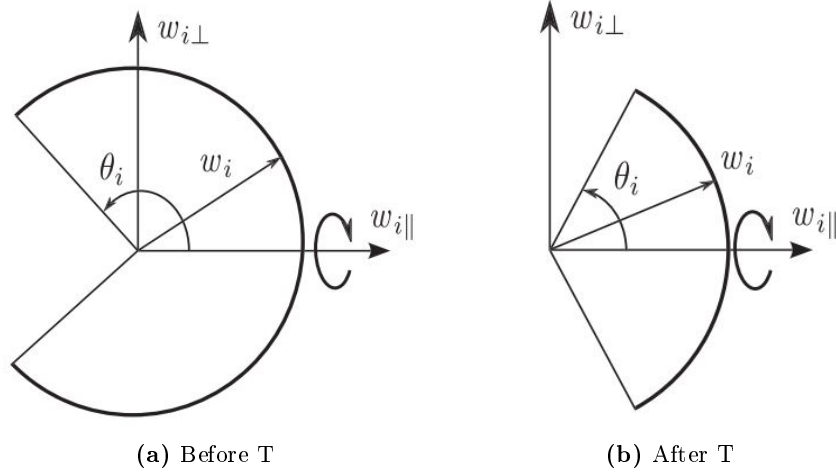


Figure 2.1: Graphical representation of the ion distribution function before and after the minimum in the maximum magnetic moment. $w_{i||}$ is the component of the velocity of the single ion parallel to the magnetic field, $w_{i\perp}$ the component perpendicular to it.

$$\theta_i = \sin^{-1} \left(\sqrt{\frac{\mu_{iT}}{\mu_{im}}} \right) \quad (2.10)$$

The average of any quantity χ_i in a general point along the nozzle can therefore be computed by taking the appropriate moment of the modified ion distribution function, as shown in Equation 2.11.

$$\langle \chi_i \rangle = \frac{n_\infty}{n_i} \frac{1}{4\pi} \left(\frac{m_i}{2E_{i\infty}} \right)^{\frac{1}{2}} \int_0^\infty \int_0^{\theta_i} \chi_i \delta(E_i - E_{i\infty}) 2\pi v_i \sin(\theta) d\theta dE_i \quad (2.11)$$

Where n_i is the ion density in the considered point of the nozzle, while v_i is the modulus of the ion velocity, strongly dependant on the initial energy of the ion.

Similarly it is possible to deduce the electron distribution function throughout the nozzle. In this case, however, an initially Maxwellian distribution is assumed, as shown in Equation 2.12

$$f_e = n_\infty \left(\frac{m_e}{2\pi k T_{e\infty}} \right)^{\frac{3}{2}} \exp \left(-\frac{E_e}{k T_{e\infty}} \right) \quad (2.12)$$

Where the suffix e is used for quantities relative to the electrons and $T_{e\infty}$ is the electron temperature at the reservoir. Again a maximum magnetic moment at each axial coordinate

may be expressed in function of the magnetic field and initial electron energy using Equation 2.13.

$$\mu_{em} = \frac{E_{e\infty} + e\Phi}{B} \quad (2.13)$$

In this case however, due to the monotonously decreasing numerator, the minimum of μ_{em} , if it is at all present, must be found in the diverging part of the nozzle. Furthermore for low values of initial energy the maximum magnetic moment may reach zero before the end of the nozzle. The electrons with these initial energies are therefore completely bounced back towards the source, irrespective of the direction of their initial velocity. Since this may happen after a local minimum in μ_{em} electrons that are generated in the portion of the nozzle between this local minimum and the zero of the maximum magnetic moment corresponding to their energy are trapped, bouncing back and forth between these two points. This model is not capable of capturing the birth and growth of this population of trapped electrons (linked either to the ignition transient or to collisions between particles) and assumes therefore a full Maxwellian distribution in this region. The distribution function delineated by this description is a full Maxwellian for all those electrons with an energy higher than the potential of the considered location and lower than the total potential drop, and a Maxwellian missing a spherical segment of the lower parallel velocities, described by the angle $\pi - \theta_e$, for the electrons with energies higher than the total potential drop. No electrons with energies lower than the potential of the considered location are obviously present, as they would have a negative kinetic energy. The electron distribution function may be more easily visualized and understood with the aid of Figure 2.2, while the angle θ_e can be computed analogously to the ions' one by means of Equation 2.14.

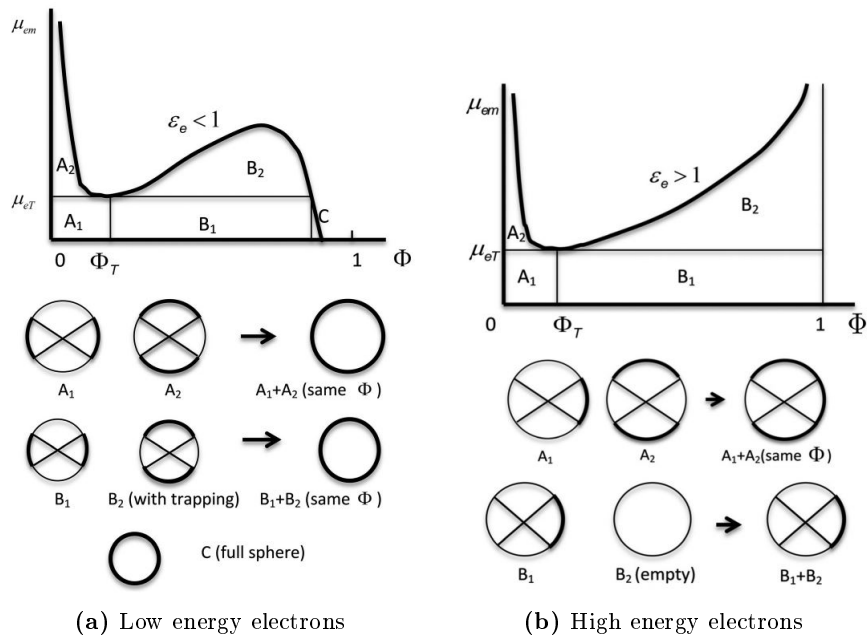


Figure 2.2: Graphical representation of the electron distribution function for particles with an initial energy lower or higher than the total potential drop. ε_e is the ratio between the initial electron energy and the total potential drop through the nozzle.

$$\theta_e = \sin^{-1} \left(\sqrt{\frac{\mu_e T}{\mu_{em}}} \right) \quad (2.14)$$

The average of a generic quantity describing the electron population may then be computed using Equation 2.15

$$\begin{aligned} \langle \chi_e \rangle = & \frac{n_\infty}{n_e} \left(\frac{m_e}{2\pi k T_{e\infty}} \right)^{\frac{3}{2}} \left[\int_{-e\Phi}^{-e\Phi_{out}} \int_0^\pi \chi_e \exp\left(-\frac{E_e}{k T_{e\infty}}\right) 2\pi v_e \sin(\theta) d\theta dE_e \right. \\ & \left. + \int_{-e\Phi_{out}}^\infty \int_0^{\theta_e} \chi_e \exp\left(-\frac{E_e}{k T_{e\infty}}\right) 2\pi v_e \sin(\theta) d\theta dE_e \right] \end{aligned} \quad (2.15)$$

Where Φ_{out} is the total potential drop through the nozzle.

It may be noticed that all the equations derived are functions of the ambipolar potential that arises inside the nozzle, which, however, is unknown. It becomes therefore necessary to assume it, and compute the error in quasi-neutrality and global current that this guess implies. The potential profile may then be used as the free variable to minimise and ideally drive to zero the mentioned errors, yielding a self consistent solution for both the electrostatic field and the plasma properties. Before this is done, however, the equations and physical quantities involved may be normalized, in order to simplify and generalise the computations. The adimensional variables and normalization quantities used from here on are summarised in table 2.1. It should be noted that the definition of a reference temperature ($T_{e\infty}$), magnetic induction (B_{max}), mass (m_i) and density (n_∞) are sufficient to completely normalize the system.

By making use of the adimensional variables and inserting $\chi_i = \chi_e = 1$ into Equations 2.11 and 2.15 the ion and electron densities corresponding to the guessed potential drop can be obtained. Their expressions are presented in Equations 2.16 and 2.17.

$$\tilde{n}_i = \frac{1}{2} \left(\sqrt{1 + \frac{\Psi}{\epsilon_i} \tilde{\Phi}} \pm \sqrt{1 + \frac{\Psi}{\epsilon_i} \tilde{\Phi} - \frac{\Psi}{\epsilon_i} \tilde{\mu}_i T \beta} \right) \quad (2.16)$$

$$\begin{aligned} \tilde{n}_e = & \exp(-\Psi \tilde{\Phi}) \operatorname{erf}\left(\sqrt{\Psi(1 - \tilde{\Phi})}\right) - \frac{2}{\sqrt{\pi}} \exp(-\Psi) \sqrt{\Psi(1 - \tilde{\Phi})} \\ & + \frac{\Psi^{\frac{3}{2}}}{\sqrt{\pi}} \int_1^\infty \left(\sqrt{\epsilon_e - \tilde{\Phi}} \pm \sqrt{\epsilon_e - \tilde{\Phi} - \tilde{\mu}_e T \beta} \right) \exp(-\Psi \epsilon_e) d\epsilon_e \end{aligned} \quad (2.17)$$

Where the \pm symbol is positive before the minimum in μ_{im} or μ_{em} and negative afterwards. Similarly, the specific current densities may be computed through the integration of the distribution functions, as indicated by Equations 2.18 and 2.19.

$$\tilde{j}_i = \tilde{n}_i \langle \tilde{v}_{\parallel i} \rangle = \frac{\Psi}{8\epsilon_i} \beta \tilde{\mu}_i T \quad (2.18)$$

$$\tilde{j}_e = \tilde{n}_e \langle \tilde{v}_{\parallel e} \rangle = \sqrt{\frac{m_{ratio}}{2\pi}} \Psi^2 \beta \int_1^\infty \tilde{\mu}_e T \exp(-\Psi \epsilon_e) d\epsilon_e \quad (2.19)$$

Having thus computed the electron and ion densities and specific currents linked to the guess of the electrical potential it is now possible to compute the error in quasi-neutrality and the deviation from the prescribed current. These deviations are used to compute a scalar error through Eq. 2.20 which, when driven to zero, leads to a self-consistent electrical potential drop.

$$err = \int_0^\infty \left[(\tilde{n}_i(z) - \tilde{n}_e(z))^2 + K (\tilde{j}_i(z) - \tilde{j}_e(z) - \tilde{j})^2 \right] dz \quad (2.20)$$

Variable	Symbol	formula
Magnetic induction	β	$\frac{B}{B_{max}}$
Potential	$\tilde{\Phi}$	$\frac{\Phi}{\Phi_{out}}$
Total potential energy	Ψ	$\frac{e\Phi_{out}}{kT_{e\infty}}$
Ion initial energy	ϵ_i	$\frac{E_i}{kT_{e\infty}}$
Electron initial energy	ϵ_e	$\frac{E_e}{ e\Phi_{out} }$
Ion magnetic moment	$\tilde{\mu}_i$	$\frac{\mu_i}{ e\Phi_{out} }$
Electron magnetic moment	$\tilde{\mu}_e$	$\frac{\mu_e}{ e\Phi_{out} }$
Ion density	\tilde{n}_i	$\frac{n_i}{n_\infty}$
Electron density	\tilde{n}_e	$\frac{n_e}{n_\infty}$
Ion specific current	\tilde{j}_i	$\frac{n_i v_i}{n_\infty \sqrt{\frac{kT_{e\infty}}{m_i}}}$
Electron specific current	\tilde{j}_e	$\frac{n_e v_e}{n_\infty \sqrt{\frac{kT_{e\infty}}{m_i}}}$
Ion velocity	\tilde{v}_i	$\frac{v_i}{\sqrt{\frac{kT_{e\infty}}{m_i}}}$
Electron velocity	\tilde{v}_e	$\frac{v_e}{\sqrt{\frac{kT_{e\infty}}{m_i}}}$
Ion temperature	\tilde{T}_i	$\frac{T_i}{T_{e\infty}}$
Electron temperature	\tilde{T}_e	$\frac{T_e}{T_{e\infty}}$
Ion kinetic energy	\tilde{E}_i	$\frac{E_i}{kT_{e\infty}}$
Electron kinetic energy	\tilde{E}_e	$\frac{E_e}{kT_{e\infty}}$
Ion energy flux	$\dot{\epsilon}_i$	$\frac{\dot{\epsilon}_i}{n_\infty \sqrt{\frac{kT_{e\infty}}{m_i}} kT_{e\infty}}$
Electron energy flux	$\dot{\epsilon}_e$	$\frac{\dot{\epsilon}_e}{n_\infty \sqrt{\frac{kT_{e\infty}}{m_i}} kT_{e\infty}}$
Mass ratio	m_{ratio}	$\frac{m_i}{m_e}$

Table 2.1: Adimensional variables and adimensionalisation parameters.

Here K is a weight used to calibrate the contribution to the error of its two components, while \tilde{j} is the adimensional desired current that the model assumes is flowing through the nozzle, and which in most cases can be fixed at 0. Of course the minimisation of the error cannot be done analytically, and a numerical method must be adopted. To this end the length of the magnetic nozzle may be discretised in a number of evaluation points, corresponding to known values of the magnetic induction and to guessed values of the potential, along with the computed values of the plasma properties. Moreover the integral to infinity present in Eq. 2.19 may be computed numerically by means of an adaptive Gauss-Kronrod quadrature method. Finally, the error can then be minimized employing an interior-point algorithm (e.g. MATLAB's *fmincon* function), that allows to constrain the search for the potential to a monotonously decreasing distribution that starts from zero.

As already mentioned, once the potential drop is known it is possible to integrate the electron and ion distribution functions so as to obtain any macroscopic quantity characterising the plasma flow. Equations 2.21 to 2.26 give, respectively the ion and electron adimensional parallel, perpendicular and total temperatures, while Equations 2.27 and 2.28 give the average of the modulus of the velocity components perpendicular to the magnetic field for the two species. Finally, Equations 2.29 and 2.30 are used to compute the average kinetic energy of respectively ions and electrons, while Equations 2.31 and 2.32 give the adimensional specific energy flux for the two species. Here, again, the integrals in ϵ_e cannot be solved analytically and are tackled numerically using the Gauss-Kronrod algorithms, while the \pm symbol assumes a positive sign upstream of μ_{iT} or μ_{eT} and a negative one downstream. Likewise, in Equations 2.27 and 2.28, the solid angles missing from electron and ion distribution functions θ_i and θ_e correspond to $\theta_i = \pi - \sin^{-1}\left(\sqrt{\frac{\mu_{iT}}{\mu_{im}}}\right)$ and $\theta_e = \pi - \sin^{-1}\left(\sqrt{\frac{\mu_{eT}}{\mu_{em}}}\right)$ before μ_{iT} and μ_{eT} , and to $\theta_i = \sin^{-1}\left(\sqrt{\frac{\mu_{iT}}{\mu_{im}}}\right)$ and $\theta_e = \sin^{-1}\left(\sqrt{\frac{\mu_{eT}}{\mu_{em}}}\right)$ afterwards. Γ and Γ_{up} are respectively the gamma function and the incomplete upper gamma function. These equations are not explicitly demonstrated and presented in Reference [2], and have been therefore manually computed. Due to the complex nature of the computations they have been, therefore, verified as strictly as possible. Section 3.1.2 presents the overall verification of the implementation of the model by comparing the behaviour of the computed potential along the nozzle to the one found in Reference [2], and the more complicated verifications of Equations 2.27 to 2.32. The validation of the other equations, obtained by simple comparison with Figures 5, 6 and 7 of Ref. [2] will not be presented here for the sake of brevity.

$$\tilde{T}_{\parallel i} = \frac{2}{3}\beta\Psi\frac{\tilde{\mu}_{im}^{\frac{3}{2}} \pm (\tilde{\mu}_{im} - \tilde{\mu}_{iT})^{\frac{3}{2}}}{\sqrt{\tilde{\mu}_{im}} \pm \sqrt{\tilde{\mu}_{im} - \tilde{\mu}_{iT}}} \quad (2.21)$$

$$\begin{aligned} \tilde{T}_{\parallel e} = & \frac{2}{3\tilde{n}_e\sqrt{\pi}} \exp(-\Psi\tilde{\Phi}) \left[1 - \Gamma_{up}\left(\Psi - \Psi\tilde{\Phi}, \frac{5}{2}\right) \right] \Gamma\left(\frac{5}{2}\right) \\ & + \frac{1}{3\tilde{n}_e\sqrt{\pi}} \Psi^{\frac{5}{2}}\beta^{\frac{3}{2}} \int_1^\infty \left[\tilde{\mu}_{em}^{\frac{3}{2}} \pm (\tilde{\mu}_{em} - \tilde{\mu}_{eT})^{\frac{3}{2}} \right] \exp(-\epsilon_e\Psi) d\epsilon_e - \frac{\langle\tilde{v}_{\parallel e}\rangle^2}{2m_{ratio}} \end{aligned} \quad (2.22)$$

$$\tilde{T}_{\perp i} = \Psi\beta \left[\tilde{\mu}_{im} - \frac{1}{3}\frac{\tilde{\mu}_{im}^{\frac{3}{2}} \pm (\tilde{\mu}_{im} - \tilde{\mu}_{iT})^{\frac{3}{2}}}{\sqrt{\tilde{\mu}_{im}} \pm \sqrt{\tilde{\mu}_{im} - \tilde{\mu}_{iT}}} \right] \quad (2.23)$$

$$\begin{aligned} \tilde{T}_{\perp e} = & \frac{4}{3\tilde{n}_e\sqrt{\pi}} \exp(-\Psi\tilde{\Phi}) \left[1 - \Gamma_{up}\left(\Psi - \Psi\tilde{\Phi}, \frac{5}{2}\right) \right] \Gamma\left(\frac{5}{2}\right) + \frac{1}{\tilde{n}_e\sqrt{\pi}} \Psi^{\frac{5}{2}}\beta^{\frac{3}{2}} \times \\ & \times \int_1^\infty \left[\frac{2}{3}\tilde{\mu}_{em}^{\frac{3}{2}} \pm \tilde{\mu}_{em}\sqrt{\tilde{\mu}_{em} - \tilde{\mu}_{eT}} \mp \frac{1}{3}(\tilde{\mu}_{em} - \tilde{\mu}_{eT})^{\frac{3}{2}} \right] \exp(-\epsilon_e\Psi) d\epsilon_e \end{aligned} \quad (2.24)$$

$$\tilde{T}_i = \frac{2}{3}\tilde{T}_{\perp i} + \frac{1}{3}\tilde{T}_{\parallel i} \quad (2.25)$$

$$\tilde{T}_e = \frac{2}{3}\tilde{T}_{\perp e} + \frac{1}{3}\tilde{T}_{\parallel e} \quad (2.26)$$

$$\langle \tilde{v}_{\perp i} \rangle = \frac{1}{\tilde{n}_i \sqrt{8\epsilon_i}} \tilde{\mu}_{im} \beta \Psi \left[\theta_i \pm \sqrt{\frac{\tilde{\mu}_{iT}}{\tilde{\mu}_{im}} - \left(\frac{\tilde{\mu}_{iT}}{\tilde{\mu}_{im}} \right)^2} \right] \quad (2.27)$$

$$\begin{aligned} \langle \tilde{v}_{\perp e} \rangle = & \frac{\sqrt{m_{ratio}}}{\tilde{n}_e \sqrt{2\pi}} \left\{ \pi \left[\exp(-\Psi \tilde{\Phi}) - (1 + \Psi - \Psi \tilde{\Phi}) \exp(-\Psi) \right] + \beta \Psi^2 \times \right. \\ & \left. \times \int_1^\infty \left[\theta_e \pm \sqrt{\frac{\tilde{\mu}_{eT}}{\tilde{\mu}_{em}} - \left(\frac{\tilde{\mu}_{eT}}{\tilde{\mu}_{em}} \right)^2} \right] \tilde{\mu}_{em} \exp(-\Psi \epsilon_e) d\epsilon_e \right\} \end{aligned} \quad (2.28)$$

$$\langle \tilde{E}_i \rangle = \epsilon_i + \tilde{\Phi} \Psi \quad (2.29)$$

$$\begin{aligned} \langle \tilde{E}_e \rangle = & \frac{1}{\tilde{n}_e \sqrt{\pi}} \left\{ 2 \exp(-\Psi \tilde{\Phi}) \left[1 - \Gamma_{up} \left(\Psi - \Psi \tilde{\Phi}, \frac{5}{2} \right) \right] \Gamma \left(\frac{5}{2} \right) + \right. \\ & \left. + \Psi^{\frac{5}{2}} \beta^{\frac{3}{2}} \int_1^\infty \left(\sqrt{\tilde{\mu}_{em}} \pm \sqrt{\tilde{\mu}_{em} - \tilde{\mu}_{eT}} \right) \tilde{\mu}_{em} \exp(-\Psi \epsilon_e) d\epsilon_e \right\} \end{aligned} \quad (2.30)$$

$$\dot{\epsilon}_i = \frac{1}{\sqrt{8\epsilon_i \tilde{n}_i}} \Psi^2 \beta^2 \tilde{\mu}_{im} \tilde{\mu}_{iT} \quad (2.31)$$

$$\dot{\epsilon}_e = \frac{1}{\sqrt{2\pi \tilde{n}_e}} \Psi^3 \beta^2 \sqrt{m_{ratio}} \int_1^\infty \tilde{\mu}_{em} \tilde{\mu}_{eT} \exp(-\Psi \epsilon_e) d\epsilon_e \quad (2.32)$$

Finally, once the plasma properties along the nozzle are known, the thrust generated by the plasma may be computed by returning to the dimensional quantities and inserting them into the classical thrust equation.

$$F = \frac{A_{th}}{\beta} (m_i n_i \langle v_{\parallel i} \rangle^2 + m_e n_e \langle v_{\parallel e} \rangle^2 + p_{\parallel e} + p_{\parallel i}) \quad (2.33)$$

Here n_i and n_e are the plasma densities at the axial location where the expansion is assumed to end, radially averaged over the plume cross section, so as to avoid considering the density at the nozzle axis uniform over the whole plume which would lead to an overestimation of the thrust. This can be obtained through a simple constant coefficient used to pass from the axial to the average radial density, as done in Ref. [1]. All the other variables are also evaluated at the given axial location. The plume cross-section has been derived by invoking the conservation of the magnetic flux $B_{max} A_{th} = B(z) A(z)$, with B_{max} and A_{th} respectively the magnetic induction and plasma cross-section at the magnetic throat. Moreover p_{\parallel} is the component of the pressure tensor parallel to the magnetic field. For both species it may be computed using the ideal gas equation:

$$p_{\parallel} = nkT_{\parallel} \quad (2.34)$$

The use of the velocity and pressure components parallel to the magnetic field lines in Equation 2.33 assumes that both these quantities remain directed axially over the full cross-section of the plasma. In reality, however, the plasma flow will increasingly diverge moving from the axis towards the plasma edge. For the pressure term this leads to a minor error since, as will be seen later, the thrust component due to the plasma pressure becomes negligible as the expansion proceeds. The component due to plasma momentum should instead be corrected by means of a divergence efficiency which, when experimentally measured on cathodeless plasma thruster prototypes, has been found to range between 60% and 90% [40]. A numerical method to calculate this efficiency will be proposed in Section 2.1.5.

The algorithm described models, as mentioned, a full convergent-divergent nozzle, where the plasma starts with a null average velocity and magnetic induction at the reservoir, and is then progressively accelerated and expanded along the initially increasing and then decreasing magnetic field. However, the magnetic geometry of real plasma thrusters typically only contains a portion of the convergent, or just a divergent nozzle. A magnetic field is in fact usually already present in the source and the magnetic nozzle cannot, therefore, begin with a null value of the magnetic induction. Taking advantage of the normalization adopted, however, it is possible to utilise this model to simulate an expansion starting in an arbitrary point of a full convergent-divergent nozzle. It is in fact sufficient to compute those stagnation quantities, here denoted with the suffix 0, that should be present in a fictitious reservoir attached to the full convergent-divergent nozzle to find at the real nozzle entrance the plasma characteristics imposed by the real source. Once the stagnation quantities are known the real plasma properties along the nozzle may be found by using them to return to dimensional variables. From table 2.1 it is apparent that the only stagnation quantities needed to fully define the plasma flow are the electron temperature and plasma density. Designating the plasma properties found in the real source with the suffix s , and the adimensional variables at the nozzle entrance with the same suffix and a tilde indicating adimensionality, the stagnation quantities can be easily obtained through Equations 2.35 and 2.36.

$$T_{0e} = \frac{T_{se}}{\tilde{T}_{se}} \quad (2.35)$$

$$n_{0e} = \frac{n_{se}}{\tilde{n}_{se}} \quad (2.36)$$

It is here important to note that this approach encounters one difficulty. The adimensional expansion in the nozzle is dependent on the normalized stagnation ion energy, strictly linked to their temperature ($\epsilon_i = \frac{3}{2}\tilde{T}_{0i}$). This value, however, is not known at the beginning of the calculations, as it is an output of the algorithm. What is known is the ion temperature in the source, and therefore at the beginning of the nozzle. An iterative procedure must be therefore implemented, beginning with a guess of the ion energy that is used to run the model. With the outputs from the algorithm the electron stagnation temperature may be computed by means of Equation 2.35 and, using it to return to physical quantities, the ion temperature at the nozzle entrance can also be found. If this calculated value is bigger than the desired one the guess of the stagnation ion energy should be decreased, while an increase in the ion energy should be made if the computed ion temperature is too small. This procedure may be repeated until the error between the desired and the computed ion temperatures at the nozzle entrance is sufficiently small. As shown in Figures 5 and 6 of Ref. [2], however, for normalized ion energies below 0.01 the sensitivity of the model on ϵ_i becomes negligible, allowing, for most realistic applications in this range, to assume a constant value of the ion kinetic energy.

2.1.3 Modified Martinez-Sanchez Model

This model, hereafter also identified as the MMS model, has been obtained by a simplification of the original MS model presented by Correyero Plaza et al. in Reference [44]. The idea behind this algorithm is to maintain the modelling of the electron behaviour unchanged, but simplify the computations regarding ions by assuming that their thermal energy is much smaller than their kinetic energy downstream of the throat. This assumption proves to be quite accurate, especially in thrusters in which the exciting electromagnetic wave is coupled with the electron dynamics, leaving the ions relatively cold. However, it implies that the model is restricted to the simulation of simply divergent nozzles, and that most of the ion properties cannot be computed, as they are linked to their thermal energy. The hypotheses behind this model are therefore identical to the ones presented in Section 2.1.2 with the addition of a negligible ion thermal energy, and the limitation to simply diverging geometries. Since the expansion does not start from a still reservoir but at the nozzle throat the initial kinetic energy of the ions must be assumed. While an energy corresponding to a sonic inlet velocity is the most justified hypothesis due to the classical assumption of a unitary Mach number at the magnetic throat, higher energies may also be used following the indications in recent experiments of slightly supersonic speeds at the throat [42].

The equations used to compute any quantity relative to the electrons are the ones found in Section 2.1.2, and will not be repeated here. As for the ions, by neglecting their thermal energy, they are all found to have exactly the same velocity vector. Using the same normalizations summarised in table 2.1, and assuming an initial kinetic energy normalized by the electrons' thermal energy ($\epsilon_{kin i} = \frac{E_{kin i}}{kT_{e\infty}}$), the energy conservation may be expressed by means of Eq. 2.37.

$$\frac{1}{2}\tilde{v}_i^2 - \Psi\tilde{\Phi} = \epsilon_{kin i} \quad (2.37)$$

By then inverting it the ion velocity may be computed at each point of the nozzle using Equation 2.38.

$$\tilde{v}_i = \sqrt{2\left(\epsilon_{Kin i} + \Psi\tilde{\Phi}\right)} \quad (2.38)$$

By now invoking the conservation of the magnetic flux to express the plume cross-section in function of the magnetic field, the total ion flux conservation can be written as follows:

$$\frac{\tilde{n}_i\tilde{v}_i}{\beta} = \sqrt{2\epsilon_{Kin i}} \quad (2.39)$$

Inverting Eq. 2.39 it is then possible to compute the ion density, as shown in Equation 2.40.

$$\tilde{n}_i = \frac{\beta\sqrt{2\epsilon_{Kin i}}}{\tilde{v}_i} \quad (2.40)$$

The ion current density is then trivially computed as $\tilde{j}_i = \tilde{n}_i\tilde{v}_i$. The algorithm then proceeds identically as the original Martinez-Sanchez code, described in Section 2.1.2, searching for the potential profile that minimises the quasi-neutrality and plasma current errors. The macroscopic properties of the electron population may again be computed using the equations

found in Section 2.1.2, while the information on the perpendicular velocity and temperature of the ions is lost due to the assumption of a negligible thermal energy. The ion average energy and energy flux may instead be computed through Equations 2.41 and 2.42.

$$\tilde{E}_i = \epsilon_{Kin i} + \tilde{\Phi}\Psi \quad (2.41)$$

$$\dot{\epsilon}_i = \tilde{E}_i \tilde{v}_i \quad (2.42)$$

Once again the thrust may then be computed by returning to dimensional quantities and using them to evaluate Equation 2.43. This equation is identical to the one used in the MS model, except for the omission of the ion pressure. This term is in fact unknown, since it depends on the ion thermal energy. In any case this is an acceptable approximation as the ion temperature and pressure tend to zero as they descend the nozzle [34]. Here again the ion and electron densities should be averaged radially to account for a non-uniform radial distribution of the density.

$$F = A (m_i n_i \langle v_i \rangle^2 + m_e n_e \langle v_{\parallel e} \rangle^2 + p_{\parallel e}) \quad (2.43)$$

2.1.4 Detachment Criteria

As already mentioned the detachment of the plasma particles from the magnetic field lines is of paramount importance in the production of a net thrust. Indeed, if the particles were to remain magnetized they would follow the field lines, which are necessarily closed due to the solenoidal nature of the magnetic field, back to the plasma source. In this case no net momentum flux would exit the system, and no thrust would be produced. The detachment of the plasma from the field lines is a complex physical phenomena which is still under discussion in the scientific community. Various theories have been advanced to explain detachment in current-free, diverging plasma jets, amongst which the most popular propose mechanisms centred on plasma resistivity [45], electron inertia [46] or stretching of the field lines by means of an induced magnetic field [47]. The most accredited theory, to date, sheds light on a complexly structured phenomenon. Detachment would, in fact, take place in a two part process. The first part sees a demagnetization of the ions due to their larger inertia, and a breaking down of the conservation of their magnetic moment [39]. These ions are however not yet able to escape from the field lines, as an ambipolar electric field prevents them from separating from the electrons. The second part involves the formation of a turbulent plume and consequently of high-frequency electric fields, that for sufficiently low values of magnetic induction or sufficiently high ion momentums enable cross-field electron transport [39]. These electric fields dissipate only once the particles' trajectories have become ballistic and the detachment may be considered complete. It is important to note that plasma detachment does not occur at a specific point in the nozzle: the plasma in fact gradually separates, starting from the outer field lines and virtually never detaching from the nozzle axis. Imposing a complete separation from the field lines at a precise axial location is therefore a rough, albeit necessary, approximation of the real physical behaviour of the plasma. Likewise, the detachment criteria presented in the following Sections do not model the real mechanisms that govern the separation from the field lines, but propose simple conditions used to identify a location at which the plasma can be considered completely detached. [48] [49]

Lafleur Criterion

This criterion is used by Lafleur et al. in Reference [1] to determine an axial coordinate at which to cease the nozzle expansion. The criterion identifies the detachment of the plasma from the magnetic field lines with the demagnetization of the ions, caused by their high inertia. Ion demagnetization is here assumed to be complete when their Larmor radius becomes comparable with the characteristic scale length of the magnetic nozzle, in this case assumed to correspond to the radius of the plasma beam. The criterion is summarised by Equation 2.44.

$$\frac{m_i \langle v_{\perp i} \rangle}{eB} \approx \sqrt{\frac{A}{\pi}} \quad (2.44)$$

Where A is the area of the plasma beam cross-section. In the case of the Lafleur MN model in which the perpendicular velocity of the ions is not directly known it can be approximated with the thermal velocity, associated to a constant ion temperature, as shown in Equation 2.45.

$$\frac{\sqrt{m_i k T_i}}{eB} \approx \sqrt{\frac{A}{\pi}} \quad (2.45)$$

While this method does indeed identify, for sufficiently large initial electron temperatures, a location downstream of the nozzle throat at which a separation between the plasma flow and the field lines may be considered, it is inconsistent with the assumption of a constant ion magnetic moment. Indeed, under this assumption, the plume radius increases and the ion temperature and consequently their gyro-radius decrease as the expansion proceeds, and so the terms in Equation 2.44 may only become comparable if initially the ion Larmor radius is bigger than the plume radius. This, however, would imply already demagnetized ions, as their gyration orbits would lead them outside of the exhaust. On the other hand, if the ions were initially sufficiently cold to have a gyro-radius smaller than the radius of the plume, they would never, under the assumption of a constant magnetic moment, reach detachment according to this criterion. A different definition of the characteristic dimension of the magnetic nozzle can however be adopted to overcome this inconsistency.

Modified Lafleur Criterion

A different characteristic scale of the magnetic nozzle, proposed in Reference [39], has been used for this criterion. The characteristic length ($L_{character}$) can in fact be computed as shown in Eq. 2.46, where the magnetic field and its derivatives are computed on the nozzle axis, while the approximation is a consequence of the assumption of a paraxial magnetic field, made in all the nozzle models presented.

$$L_{character} = \frac{\|\nabla B\|}{B} \approx \frac{dB}{dz} \quad (2.46)$$

To employ this equation the dependence of the magnetic induction on the axial coordinate must be known. To this end the assumption of a magnetic nozzle produced by a single ring of current of radius R_r has been made. The magnetic nozzles of plasma thrusters are in fact, typically, produced by either a ring of magnets or an induction solenoid, the field of which can be sufficiently accurately modelled in this way. For this simple case the magnetic field lines may be found through the use of Equation 2.47. [50]

$$\psi(\tilde{z}, \tilde{r}) = \frac{\frac{\tilde{r}^2}{2}}{(1 + \tilde{r}^2 + \tilde{z}^2)^{\frac{3}{2}}} \quad (2.47)$$

Where ψ is constant along the flux tubes and \tilde{r} and \tilde{z} are the radial and axial coordinates, normalized by the radius of the current ring generating the magnetic field. The value of ψ_{out} corresponding to the outer field line can therefore be computed by evaluating Eq. 2.47 in $\tilde{r} = \frac{R_f}{R_r}$, with R_f the radius of the source exhaust, and $\tilde{z} = 0$, where the considered flux tube exits the source. Since ψ_{out} must be constant along the whole outer field line its radial and axial coordinates are implicitly related through Eq. 2.48. Furthermore the magnetic induction can be written as a function of the radial coordinate by means of the conservation of the magnetic flux, as shown in Equation 2.49.

$$\frac{\frac{\tilde{r}^2}{2}}{\left(1 + \tilde{r}^2 + \tilde{z}^2\right)^{\frac{3}{2}}} = \psi\left(0, \frac{R_f}{R_r}\right) = \frac{\frac{\left(\frac{R_f}{R_r}\right)^2}{2}}{\left(1 + \left(\frac{R_f}{R_r}\right)\right)^{\frac{3}{2}}} \quad (2.48)$$

$$B = B_{th} \left(\frac{1}{\tilde{r}} \frac{R_f}{R_r}\right)^2 \quad (2.49)$$

By using Eq. 2.49 to write B in function of \tilde{r} and Eq 2.48 to express \tilde{r} in function of \tilde{z} , the magnetic induction can therefore be linked implicitly to the axial coordinate and, consequently, the derivative of the magnetic field with respect to z may be computed by means of the central finite differences algorithm. The criterion then assumes detachment in the position along the nozzle in which the ion gyro-radius becomes greater than the characteristic length computed, as shown in Eq. 2.50. Again, in the case of the Lafleur MN model, Eq. 2.51 may be used.

$$\frac{m_i \langle v_{\perp i} \rangle}{eB} > L_{character} \quad (2.50)$$

$$\frac{\sqrt{m_i k T_i}}{eB} > L_{character} \quad (2.51)$$

Merino criterion

This criterion has been derived starting from the studies of Merino et al. on the complex bi-dimensional mechanisms that lead to plasma detachment from magnetic field lines. It states that when the maximum centrifugal forces acting on the ions following the stream tube containing 95% of the mass flux become comparable with the maximum centripetal forces, complete detachment may be assumed [49]. Because the detachment mechanism described has an inherently bi-dimensional nature, due to the presence of radial magnetic forces, only the complete Martinez-Sanchez model captures sufficient information on the plasma properties to make use of this criterion. In any case, a series of very rough hypotheses and approximations must be made to apply it to a mono-dimensional model. These are summarised below:

- Given normalized radial density profile in the plasma source $f\left(\frac{r}{R_s}\right)$.
- Ions and electrons are assumed to follow faithfully the field lines until detachment. This implies a self-similar radial density profile throughout all of the nozzle.
- The magnetic nozzle geometry is produced by a single ring of current, located at the source exhaust.
- The azimuthal velocity of a species is approximated with its computed average velocity perpendicular to the magnetic field lines.

- Negligible electron inertia.
- Cold ions.
- Radially uniform modulus of the plasma velocity.

The criterion assumes complete detachment at the axial coordinate in which the centrifugal forces become bigger than the centripetal forces acting on the ions, as expressed by Equation 2.52. Where the left hand side of the equation contains the inertial forces due to the radial curvature of the considered field line, with $\langle v_{\parallel i} \rangle$ the mean ion velocity parallel to the magnetic field at a given axial coordinate, and R_{cur} the radius of curvature of the field line at the axial coordinate considered. The right hand side is instead formed, from left to right, by the force generated by the electrostatic field (f_e), the magnetic forces, and the inertial forces due to the ions' azimuthal rotation. Here $\langle v_{\theta i} \rangle$ is the average azimuthal velocity of the ions and $r_{95\%}$ is the radial coordinate of the field line containing 95% of the mass flux at the considered axial coordinate. As mentioned, since the ions demagnetize before the electrons, an ambipolar potential forms inside the plasma generating an electrostatic force (f_e) on both ions and electrons, that imposes quasi-neutrality and freezes them onto the field lines, until the electrons are also demagnetized. Since the azimuthal velocity cannot be calculated by the quasi-mono-dimensional model of the magnetic nozzle it has been approximated with the particles' velocity perpendicular to the nozzle axis. This is a very rough assumption, as the perpendicular velocity computed by the MS model is a thermal excitation velocity and is only loosely linked to the average azimuthal velocity of the ions. Finally, in Eq 2.52, the forces due to the pressure gradient have been neglected, due to the assumption of cold ions.

$$\frac{m_i \langle v_{\parallel i} \rangle^2}{R_{cur}} < -f_e + e \langle v_{\theta i} \rangle B + \frac{m_i \langle v_{\theta i} \rangle^2}{r} \approx -f_e + e \langle v_{\perp i} \rangle B + \frac{m_i \langle v_{\perp i} \rangle^2}{r_{95\%}} \quad (2.52)$$

The electrostatic force f_e is known to act centrifugally on the ions, and to attract the electrons with identical intensity towards the nozzle axis [49]. It may therefore be computed by imposing the equilibrium of forces on the electrons, which are assumed to faithfully follow the field lines until detachment, through Equations 2.53, 2.54 and 2.55 .

$$f_e = f_m + f_p \quad (2.53)$$

$$f_p = kT_e \frac{d(\ln n_e)}{d\hat{i}_{\perp}} \quad (2.54)$$

$$f_m = -e \langle v_{\theta e} \rangle B \approx -e \langle v_{\perp e} \rangle B \quad (2.55)$$

Here f_p is the force caused by the pressure gradient acting orthogonally to the field line, computed as the derivative in the direction perpendicular to the field line of the density logarithm [49]. f_m instead is the magnetic force due to the electron azimuthal velocity, which has again been approximated with the velocity component perpendicular to the magnetic field.

All of the quantities in Eqs. 2.52 to 2.55 must be computed on the field tube containing 95% of the mass flux. To identify this stream tube it is necessary to assume the radial density profile in the plasma source. Normalized radial density profiles are typically empirical expressions or simple analytical solutions to the diffusion equations such as the first Bessel function of order zero [1] [34]. In general a radial density distribution can be expressed as a function of the radial

coordinate, normalised by the source radius, so that the expression of the plasma density can be written as:

$$n(z, r) = n(z, 0) f\left(\frac{r}{R_s}\right) \quad (2.56)$$

Where f is the normalized radial distribution and $n(z, 0)$ is the density found on the axis of symmetry at the considered axial coordinate. Thanks to the assumption of a radially uniform plasma velocity the radial coordinate inside the source ($R_{95\%}$) of the wanted stream tube can then be identified by solving numerically Equation 2.57.

$$\int_0^{R_{95\%}} f\left(\frac{r}{R_s}\right) r dr = 0.95 \int_0^{R_s} f\left(\frac{r}{R_s}\right) r dr \quad (2.57)$$

By considering that the magnetic nozzle is produced by a current ring of radius R_r positioned at the source exit it is possible to implicitly link the radial coordinate of the field line ($r_{95\%} = r_{95\%}(z)$) to the axial coordinate through Eq. 2.58 [50], analogously to what has been done in Eq. 2.48 for the modified Lafleur detachment criterion.

$$\frac{\frac{\left(\frac{r_{95\%}}{R_r}\right)^2}{2}}{\left(1 + \left(\frac{r_{95\%}}{R_r}\right)^2 + \left(\frac{z}{R_r}\right)^2\right)^{\frac{3}{2}}} = \frac{\frac{\left(\frac{R_{95\%}}{R_r}\right)^2}{2}}{\left(1 + \left(\frac{R_{95\%}}{R_r}\right)^2\right)^{\frac{3}{2}}} \quad (2.58)$$

The inclination of the field line ($\alpha(z)$) at a given axial coordinate may now be computed through Equation 2.59.

$$\alpha(z) = \arctan\left(\frac{dr_{95\%}(z)}{dz}\right) \quad (2.59)$$

The radius of curvature R_{cur} of the considered field line may also easily be computed numerically for any axial coordinate as explained by Reference [51].

Finally, to compute the derivative in Equation 2.54, a strict definition of the plasma density present in the whole domain of the magnetic nozzle is necessary. Given the normalized axial and radial coordinates of a position in the nozzle (\tilde{z}, \tilde{r}), the local density may be defined by retracing the field line passing through this point back to the thruster, so as to find the radial coordinate r_s at which the fluid element had left the source, by means of the numerical solution of Equation 2.60.

$$\frac{\frac{\tilde{r}^2}{2}}{\left(1 + \tilde{r}^2 + \tilde{z}^2\right)^{\frac{3}{2}}} = \frac{\frac{\left(\frac{r_s}{R_r}\right)^2}{2}}{\left(1 + \left(\frac{r_s}{R_r}\right)^2\right)^{\frac{3}{2}}} \quad (2.60)$$

Once r_s is known, in fact, the density in the considered point may be computed through Eq. 2.56, by multiplying the density distribution evaluated in r_s by the density on the nozzle axis

at the considered axial coordinate. By then using finite central differences, and defining δ as an arbitrarily small length, Equation 2.54 may be approximated as:

$$f_p(z) \approx kT_e(z) \frac{\ln [n(z - \delta \cos(\alpha(z)), r_{95\%}(z) + \delta \sin(\alpha(z)))]}{2\delta} - \frac{\ln [n(z + \delta \cos(\alpha(z)), r_{95\%}(z) - \delta \sin(\alpha(z)))]}{2\delta} \quad (2.61)$$

All of the terms in Equation 2.52 are now computable for any axial coordinate that precedes the turning point of the considered field line (where the numerical computations incur into singularities), and the detachment location given by the Merino criterion can therefore be identified.

Arefiev Criterion

Arefiev, instead, proposes to identify the detachment location by imposing the equality between the specific magnetic and kinetic energies in the plasma [52]. This condition is linked to the capability of the charged particles to induce a magnetic field of sufficient magnitude to stretch the existing field lines to infinity. The particles, in this scenario, do not strictly speaking detach from the field lines, but stretch them so that they do not turn back towards the thruster. The insertion of the plasma particles onto ballistic trajectories is therefore assumed when the condition presented in Equation 2.62 is verified.

$$\frac{B^2}{2\mu_0} < n(E_i + E_e) \quad (2.62)$$

Where μ_0 is the magnetic void permeability and E_i and E_e are respectively the ion and electron kinetic energies.

2.1.5 Divergence Efficiency

As mentioned, when computing the thrust by means of the classical thrust equation, the momentum term should be corrected by introducing a divergence efficiency that takes into account the fact that the plasma velocity is not axial along the whole cross section of the plasma beam. The divergence efficiency at a given axial position ($\eta_{div}(z)$) can in fact be defined as the ratio between the local axial momentum and total momentum fluxes, as shown in Equation 2.63. Where $r_{out}(z)$ is the radial coordinate of the most external field line, which can again be implicitly expressed as a function of z through Equation 2.48

$$\eta_{div}(z) = \frac{\int_0^{r_{out}(z)} n(z, r)v(z, r)^2 \cos(\alpha(z, r)) r dr}{\int_0^{r_{out}(z)} n(z, r)v(z, r)^2 r dr} \quad (2.63)$$

Here $n(z, r)$ and $v(z, r)$ are respectively the plasma density and the modulus of the velocity at the given position in the nozzle. While the former may be computed as explained in Section 2.1.4, the latter is assumed to be equal to the velocity computed by the MN model on the nozzle axis at the same axial position. Finally, $\alpha(z, r)$ is the inclination of the local velocity vector with respect to the axial direction. By assuming that the particles are perfectly magnetized up to the detachment point, and that no deviation of the velocity occurs at detachment, this angle may be considered identical to the inclination of the field line passing through the given location. Given a generic field line, identified by the constant $\psi(z, r)$ determined through Eq.

2.47, the angle between its tangent at a given axial coordinate and the axial direction may be expressed using Equation 2.64.

$$\alpha(z, r) = \arctan\left(\frac{dr(\Psi, z)}{dz}\right) \quad (2.64)$$

By using central finite differences to evaluate α in Eq. 2.64, and a trapezoidal algorithm to compute the integrals in Equation 2.63, the divergence efficiency may be obtained for any axial position along the nozzle. Given a detachment location (z_{det}), therefore, the thrust equation may, in general, be corrected as shown by Eq. 2.65.

$$F = \dot{m}v(z_{det})\eta_{div}(z_{det}) + A_e(z_{det})p_{\parallel}(z_{det}) \quad (2.65)$$

It should be noted that this correction considers the deviation of the velocity parallel to the magnetic field lines from the axial direction, but doesn't consider the fact that the perpendicular velocity might consequently have a component directed axially. This contribution to the total thrust is however negligible, since the modulus of the perpendicular velocity becomes irrelevant proceeding with the expansion, as shown by Figure 7 of Reference [2]. It is also important to remark here that the assumption made according to which the plasma velocity is always tangent to the magnetic field lines causes an inconsistency with the nozzle models presented. All the models in fact consider the plasma velocity directed axially over the whole cross section of the plume. Changing this hypothesis leads to a breakdown of the particle flux conservation, as, instead of being constant over the planes orthogonal to the nozzle axis, as assumed by the presented MN models, it becomes constant over the surfaces orthogonal to the field lines. However, when considering a sufficiently slender geometry of the magnetic nozzle, this approximation may become acceptable. It is also worth mentioning that recent studies have shown that the plasma detachment does not happen tangentially to the field lines, but a slight inward deviation of the velocity is present. For a first estimation of the divergence efficiency, however, the assumption of tangential detachment can be made. [49]

2.2 Plasma Source Models

The plasma source is where the neutral propellant gas is ionized and the plasma is produced. Electrons in the gas are in fact excited using radio-frequency waves and their collision with the neutral atoms produce excited neutrals, ions, and more electrons. The behaviour of the plasma in this region is complex and of complicated modelling. The coupling between the electromagnetic wave and the plasma, the collisions and reactions between the particles, the spontaneous de-excitation of excited atoms, the energy diffusion and transfer between the particles and between the species that compose the plasma, the plasma diffusion orthogonal and parallel to the induced magnetic field, along with the behaviour and dynamics of the neutral species are all intertwined phenomena that influence the plasma production in this region. Two mathematical models are proposed in Sections 2.2.1 and 2.2.2 with the intent of modelling this section of a cathodeless plasma thruster. Particular attention has been posed to the plasma chemistry and dynamics, while the introduction of the electromagnetic energy into the plasma has not been precisely modelled: a fraction, determined empirically, of the total available energy has simply been considered to be transferred into the plasma.

2.2.1 Lafleur Source Model

This semi-analytical model, proposed by Lafleur in Reference [1], is capable of describing the plasma behaviour in the source by reducing the system to a quasi-mono-dimensional domain

and by making strong simplifying hypotheses on the plasma dynamics. The assumptions made are summarised below:

- Uniform, paraxial magnetic field
- Constant electron temperature along the source
- Cold ions
- Massless electrons
- Quasi-neutral plasma
- Maxwellian electron distribution
- Empirically imposed radial distribution of the plasma density, self similar along the source
- Negligible radial momentum losses
- Radially uniform longitudinal velocity
- Constant neutral gas velocity
- Bohm velocity at source walls and at the exhaust section
- No momentum exchange between the particles because of collisions

These assumptions must be thoroughly commented, as their influence on the plasma properties predicted by the model proves to be important. The accuracy of the assumptions linked to the magnetic geometry varies according to the thruster to be modelled. While a roughly uniform and paraxial magnetic field was initially adopted in the design of Helicon and ECR plasma thrusters, recent research indicates that an increase in the magnetic induction near the source exhaust may increase the thruster performances [53]. This type of geometry necessarily requires also non-axial components to the magnetic field. However, because of the assumption of a uniform paraxial magnetic field the Lafleur source model is not capable of capturing the beneficial effects of non-axial, variable magnetic geometries and must average the magnetic induction in the source in order to impose a constant field as representative as possible of the real one. In stationary conditions, instead, the assumption of isothermal electrons and cold ions is close to the real situation found in a typical Helicon or ECR plasma thruster. Numerous experiments have in fact shown that, once the thruster has reached stationary conditions, the electron temperature results uniform throughout the plasma source while the ions find an equilibrium at temperatures one order of magnitude lower [1] [54] [55]. Their contribution to the plasma entalpy, along with the pressure forces in their dynamics, may therefore be neglected. Similarly the assumption of negligible electron inertia forces and of quasi-neutrality cause small deviations from the real plasma physics found in the source. The assumption of a Maxwellian electron distribution, instead, while it results inevitable in order to analytically model the reactions that produce and characterise the plasma, may not accurately capture the true conditions of the electron population. The electron distribution in cathodeless plasma thrusters is in fact not necessarily Maxwellian, and the influence of different electron distributions on the propulsive properties of plasma thrusters is still an open question in the scientific community [43] [56]. Likewise the empirically determined radial density distribution is fundamental to the implementation of the model, as it allows to consider plasma neutralization at the source walls, a phenomenon that greatly influences the plasma density and energy. However, while the distribution considered has been shown to faithfully model the radial density profile for intense confining magnetic fields (e.g. 4000 G) [1] its application to the weaker fields typically present in cathodeless plasma thrusters (~ 300 G) should be further verified. Furthermore, the radial momentum losses in a plasma source have been recently measured experimentally and proven to be small, allowing to neglect them in the overall momentum budget of the plasma. Similarly the hypothesis of a radially uniform longitudinal velocity causes only small errors in the model's predictions, due to the small dimensions of the plasma sheath compared to the radius of the source. On the other hand, while the assumption of the Bohm velocity at the

source's physical boundaries is classically used to model stationary plasma sheaths, its imposition over the exhaust section may lead to relevant errors, as some experiments have shown that the magnetic throat of a MN does not necessarily coincide with a sonic velocity [42]. Finally, while neglecting the particle collisions in the momentum balances of ions and electrons is necessary to find a closed form solution to the equations, it strongly affects the accuracy of the model's predictions, as will be shown in Chapter 3. The computed velocity of the plasma, unhindered by particle collisions, can in fact be expected to reach higher values than the ones present in a collisional plasma, and consequently, as will be explained, the model has been found to overestimate the plasma temperature.

The radial distribution of the density is assumed to follow the following empirical fitting, proposed in Ref [1]:

$$n(z, \rho) = n(z, 0) \left[1 - (1 - h_R^{\frac{1}{6}}) \rho^2 \right]^6 \quad (2.66)$$

In this case the origin of the axes is placed at the back of the source and on the axis of symmetry. Here $\rho = \frac{r}{R_s}$ is the radial coordinate normalised by the source radius, $n(z, \rho)$ the plasma density at the given axial and radial coordinates, and h_R is the ratio between the density on the source axis and that at the source walls, again found experimentally to be [1]:

$$h_R = \frac{0.4}{\sqrt{1 + 0.68 \left(\frac{R_s}{r_{ci}} \right)^2}} \quad (2.67)$$

Here $r_{ci} = \frac{\sqrt{kT_i/m_i}}{\omega_{ci}}$ is the average ion gyro-radius, approximated by considering the ion thermal velocity equal to the average velocity perpendicular to the magnetic field. While in the momentum and energy balances the ion temperature is considered null, for this particular computation it has been empirically fixed at a constant value T_i . By integrating Eq. 2.66 over the source section the average density may be determined to be $\langle n(z) \rangle = n(z, 0) \lambda$ with:

$$\lambda = \frac{1 - h_R^{\frac{7}{6}}}{7(1 - h_R^{\frac{1}{6}})} \quad (2.68)$$

The λ parameter can be used, in any point of the source or of the nozzle, to pass from the on-axis plasma density to the average density over the full cross-section of the plasma thanks to the assumption made in all the nozzle models of perfectly magnetized plasma particles. In particular it can be used to obtain the radially averaged plasma densities used in Equations 2.33 and 2.43, while the radial distribution expressed in Equation 2.66 may be inserted in Equation 2.63 to compute the divergence efficiency of a thruster.

Having defined the radial distribution of the density, the electron temperature, considered constant along the source, may be determined by solving the system of Equations 2.69. These equations have been obtained by Lafleur by integrating the continuity and momentum conservation equations for electrons and ions, simplified with the presented hypotheses, and imposing sonic boundary conditions at the axial extremities of the source [1]. A generalisation of the system can be made so as to include subsonic exhaust conditions, while a supersonic one is beyond this model's capabilities because of the singularity in Equation 14 of Ref. [1] at the

unitary Mach number, and that cannot therefore be integrated into the supersonic region.

$$\left\{ \begin{array}{l} \gamma + 2 + \xi \ln \left(\frac{1 - \xi}{1 + \xi} \right) - 2\sqrt{1 - \xi^2} \left[\arctan \left(\frac{1 - \xi}{\sqrt{1 - \xi^2}} \right) - \arctan \left(\frac{-1 - \xi}{\sqrt{1 - \xi^2}} \right) \right] = 0 \\ \gamma = a \frac{K_{iz}}{u_b} - b \\ \xi = \frac{\eta_d}{1 - \frac{u_b}{K_{iz}} \frac{b}{a}} \\ a = \frac{\Gamma_0 L_s}{v_g} \\ b = \frac{2h_R L_s}{\lambda R_s} \end{array} \right. \quad (2.69)$$

Here K_{iz} is the ionization rate for the considered propellant, that can be obtained by integrating the ionization cross-section multiplied by the relative impact velocity over the assumed Maxwellian electron distribution, as done in Equation 2.70. u_b is the Bohm velocity, Γ_0 the propellant particle flux per unit area flowing through the source, L_s the length of the source, and v_g the neutral gas velocity, considered constant throughout the source. η_d is the propellant utilisation efficiency, defined as the ratio between the plasma mass flux at the exhaust over the total mass flux. η_d has to be hypothesised to begin the computations but, as will be shown later, it is strictly linked to the power required by the thruster and can therefore be iteratively determined. Both the ionization rate and Bohm velocity strongly depend on the electron temperature, as shown in Equations 2.70 and 2.71. Because of this the system of Equations 2.69 has no analytical solution and must be solved numerically.

$$K_{iz} = 2\sqrt{\frac{2\pi}{m_e}} \left(\frac{1}{kT_e} \right)^{\frac{3}{2}} \int_{\epsilon_{iz}}^{\infty} \sigma(\epsilon, T_e) \exp \left(-\frac{\epsilon}{kT_e} \right) \epsilon d\epsilon \quad (2.70)$$

$$u_b = \sqrt{\frac{kT_e}{m_i}} \quad (2.71)$$

Here m_e and m_i are the ion and electron masses, k is the Boltzmann constant, ϵ the electron kinetic energy and ϵ_{iz} the first ionization energy. Finally T_e is the electron temperature. Empirical fittings of the behaviour of the ionization cross-section in function of the electron temperature may be found in References [57] and [58] for Argon and Xenon respectively. The cross-section fittings are found to follow the experimental data in an electron temperature range between 5 eV and 30 eV, meaning that the presented model cannot describe a plasma discharge that exceeds these temperature ranges. In this case the expression of the cross-sections would have to be changed to ones valid in the temperature range considered.

As explained previously, the hypothesis made in the demonstration of Eq. 2.69 of no momentum transfer or loss because of collisions in the plasma, is expected to lead to an overestimated plasma velocity at the extremities of the source tube. As a consequence the use of Equation 2.69 yields an excessively high electron temperature. By imposing a unitary Mach number at the source efflux and back wall, in fact, the Bohm velocity is enforced equal

to the large speeds found in these regions by the integration of the momentum and continuity equations, resulting in high electron temperatures.

Once the temperature is known the plasma velocity at any point of the source axis may be computed using Equation 2.72, again obtained through the integration of the continuity and momentum balance equations, with ξ and γ corresponding to the newly calculated temperature.

$$\gamma \bar{z} + 1 + M(z) + \xi \ln \left(\frac{1 - 2\xi M(z) + M(z)^2}{2 + 2\xi} \right) - 2\sqrt{1 - \xi^2} \left[\arctan \left(\frac{1 - \xi}{\sqrt{1 - \xi^2}} \right) - \arctan \left(\frac{-1 - \xi}{\sqrt{1 - \xi^2}} \right) \right] = 0 \quad (2.72)$$

Where $M(z)$ is the plasma Mach number along the source axis and $\bar{z} = \frac{z}{L_s}$ is the axial coordinate normalised by the full length of the source. The dimensional velocity of the plasma may be easily retrieved by multiplying the Mach number by the Bohm velocity $v(z) = M(z)u_b$. As demonstrated in Ref. [1], the maximum plasma density in the source (n_0) will be found where the velocity is zero, and can be computed as shown in Equation 2.73. Thanks to the conservation of axial momentum, deriving from the assumptions made, the density distribution along the source axis may then be obtained through Equation 2.74.

$$n_0 = \frac{2\eta_d \Gamma_0}{\lambda u_b} \quad (2.73)$$

$$n(z, 0) = \frac{n_0}{1 + M(z)^2} \quad (2.74)$$

Finally the neutral gas density in the source, considered radially uniform, may be determined using Equation 2.75.

$$n_g(z) = \frac{\Gamma_0 - \lambda n(z, 0)v(z)}{v_g} \quad (2.75)$$

The source characteristics are thus fully determined, as the electron temperature, plasma density and velocity, and the neutral gas velocity are all known in all points of the source. These quantities are all function of the hypothesised propellant utilisation efficiency, that can however be determined by means of an energy balance. The energy fluxes leaving the thruster through the back wall (P_{back}) and radially through the lateral walls (P_{side}) may be computed using the systems of Equations 2.76 and 2.77.

$$\left\{ \begin{array}{l} P_{back} = \frac{1}{2} q \lambda n_0 u_B A_s (\epsilon_c + \epsilon_{ib} + \epsilon_{eb}) \\ \epsilon_c = \epsilon_{iz} + \frac{K_{exc}}{K_{iz}} \epsilon_{exc} \\ \epsilon_{ib} = \frac{kT_e}{2q} \\ \epsilon_{eb} = 2 \frac{kT_e}{q} + \frac{kT_e}{2q} \ln \left(\frac{m_i}{2\pi m_e} \right) \end{array} \right. \quad (2.76)$$

$$\left\{ \begin{array}{l} P_{side} = 2\pi q R_s h_R \left(\int_0^{L_s} n dz \right) u_B (\epsilon_c + \epsilon_{is} + \epsilon_{es}) \\ \epsilon_c = \epsilon_{iz} + \frac{K_{exc}}{K_{iz}} \epsilon_{exc} \\ \epsilon_{is} = \frac{T_e}{2} \\ \epsilon_{es} = 2T_e + \frac{T_e}{2} \ln \left(\frac{m_i}{2\pi m_e} \right) \end{array} \right. \quad (2.77)$$

Where ϵ_c is the collisional energy loss due to ionization and excitation, ϵ_{ib} and ϵ_{is} are the kinetic energies of ions respectively at the back and side walls. ϵ_{eb} and ϵ_{es} are, instead, the kinetic energies of electrons in the same locations. Finally ϵ_{exc} and ϵ_{iz} are the excitation and ionization energies in eV, while K_{exc} and K_{iz} are the excitation and ionization rates. As before these may be obtained through the use of Equation 2.70 and the regressions of the excitation and ionization cross-sections presented in references [57] [58].

The expression for the energy flux exiting the source through the nozzle depends, instead, on the magnetic nozzle model considered. When considering the Lafleur MN model, in fact the energy flux leaving through the thruster exhaust (P_{exit}) may be computed through the system of equations Equations 2.79.

$$\left\{ \begin{array}{l} P_{exit} = \frac{1}{2} q \lambda n_0 u_B A_s (\epsilon_c + \epsilon_{ie} + \epsilon_{ee}) \\ \epsilon_c = \epsilon_{ion} + \frac{K_{exc}}{K_{iz}} \epsilon_{exc} \\ \epsilon_{ie} = \frac{T_e}{2} \\ \epsilon_{ee} = 2T_e + \frac{1}{2} M_{det}^2 T_e \end{array} \right. \quad (2.78)$$

Where ϵ_{ie} and ϵ_{ee} are the ion and electron kinetic energies at the source exhaust, while M_{det} is the plasma Mach number at the detachment point identified through one of the detachment criteria. When instead the MS model or the MMS model are used the energy flowing out of the nozzle may be computed as:

$$\left\{ \begin{array}{l} P_{exit} = \frac{1}{2} q \lambda n_0 u_B A_s \epsilon_c + k T_e \lambda n u_b A_s (\dot{\epsilon}_i + \dot{\epsilon}_e) \\ \epsilon_c = \epsilon_{ion} + \frac{K_{exc}}{K_{iz}} \epsilon_{exc} \end{array} \right. \quad (2.79)$$

Where $\dot{\epsilon}_i$ and $\dot{\epsilon}_e$ are the specific adimensional ion and electron energy fluxes computed by the considered MN model at the nozzle entrance, while A_s is the source cross-section. T_e and n are respectively the electron temperature and the plasma density by which the quantities computed by the considered model are normalized. For the MMS model, therefore, they are the density

and temperature computed by the source model at the source exhaust, while for the MS model they correspond to the stagnation temperatures obtained through Equations 2.35 and 2.36. The full expansion through a convergent-divergent nozzle considered by the Martinez-Sanchez model cannot, in fact, be utilised, and the use of stagnation quantities results necessary. Indeed, the presence of a magnetic field inside the source means that the expansion cannot start from a null magnetic induction. Likewise, u_b is the Bohm velocity corresponding to the normalizing temperature.

Assuming stationary conditions the energy flux exiting the thruster must be equal to the one entering and so the power deposited into the plasma by the radio-frequency wave (P_{abs}) may be trivially computed using Equation 2.80. By concentrating the wave-plasma interaction and the efficiency of the antenna's electric circuit in a single, empirically determined, efficiency (η_{rf}), with values ranging between 60% and 95%, the total power required by the thruster (P_{tot}) is found through Equation 2.81. As already said the total power used by the engine is strictly dependent on the electron temperature, which is in turn strongly linked to the propellant utilisation efficiency. It is therefore possible to vary this input until the desired power consumption is obtained.

$$P_{abs} = P_{back} + P_{side} + P_{exit} \quad (2.80)$$

$$P_{tot} = \eta_{rf} P_{abs} \quad (2.81)$$

Finally, the thrust deriving from remaining neutral atoms must be computed to fully characterize the propulsive properties of the modelled thruster. To this end the condition in which no ionization reactions are present in the source has been considered. While this is a strong and limiting assumption it is mitigated by the low ionization ratio present in typical cathodeless plasma sources (usually lower than 0.15 [8]), and by the small contribution given to the thrust by the neutral particles in comparison to the charged ones accelerated in the MN nozzle. Under this assumption the thrust provided by the neutral flow out of the source (F_n) may be computed using Equation 2.82 [1]. Where \dot{m} is the total mass flux flowing through the thruster and T_g and v_g are respectively the neutral gas temperature and its velocity. Both of these quantities can be assumed constant, with $T_g = 0.026$ eV, corresponding to ambient temperature, and v_g the sonic velocity in the considered gas at this temperature.

$$F_n = \dot{m} v_g \left(1 + \frac{e T_g}{m_i v_g} \right) \quad (2.82)$$

If the geometry, magnetic field, power consumption and mass flux of a thruster are known its propulsive properties can now be completely defined. By guessing a propellant consumption efficiency, in fact, the source characteristics may be computed through the presented model and then used to define the starting conditions of one of the three MN models presented. The modelled power consumption linked to the chosen η_d can then be found and a new guess of the propellant consumption efficiency may be formulated, until a power usage corresponding to the desired one is found. Once η_d is known the source and nozzle are completely characterized, and the propulsive properties of the thruster may be computed.

2.2.2 Global Source Model

Based on the work done in References [36], [35] and [37] a global source model has been developed. The source domain has been therefore reduced to a single node, onto which the

particle and energy equilibriums have been imposed and integrated. The model obtained is capable of describing the neutral gas dynamics and the thrust produced by neutral particles in function of the thruster geometry and plasma production. It also models the reactions between the charged and neutral particles in an Argon discharge (to which the model is limited, no other propellants may be considered), by taking into account the single and step-wise excitation to the 4S and 4P orbitals as well as collisional de-excitation, direct and step-wise ionization and neutralization, elastic scattering of electrons, Coulomb elastic scattering, Langevin scattering of ions and charge exchange between ions and neutrals. Further detail on the plasma collisions and a comparison of the reaction rates found in the literature can be found in the dedicated paragraph in this Section and in Section 3.1.4. The model also computes the parallel and transversal diffusion coefficients by means of analytical solutions to the diffusion equations, from which it extrapolates the plasma density at the source boundaries using heuristic relations. The possibility of considering a magnetic field geometry formed by a set of radially directed magnets and therefore provided of cusp lines along the outer walls of the source has also been included [3] [8]. Finally, the global source model has been coupled with the nozzle models presented in Section 2.1 in order to compute the particle and energy fluxes out of the exhaust as well as the propulsive properties of the modelled thruster. The main hypotheses and constraints onto which the model is based are summarised below:

- Argon propellant
- Constant temperature of the neutrals inside the source
- Isentropic expansion of the neutrals in the nozzle
- Constant ion temperature in the source
- Paraxial, uniform magnetic field in the source, except at the cusp regions
- Bohm criterion at the source walls
- Maxwellian ion and electron distribution

Having imposed the temperature of ions and neutrals at the fixed values of respectively $T_i = 0.2 \text{ eV}$ [1] and $T_n = 300 \text{ K}$, the state of the plasma inside the source can be completely identified by means of the density of the neutral unexcited atoms (n_n), the density of the neutral atoms with the outer electron excited to the 4S orbitals (n_{4S}), the density of the neutral atoms with the outer electron excited to the 4P orbitals (n_{4P}), the density of ions (n_i), the density of electrons (n_e) and the electron temperature (T_e). These quantities may be grouped as show below:

$$\left\{ \begin{array}{l} \underline{n} = \begin{bmatrix} n_n \\ n_{4S} \\ n_{4P} \\ n_i \\ n_e \end{bmatrix} \\ T_e = T_e \end{array} \right. \quad (2.83)$$

The evolution of the state of the system thus defined may be easily described by imposing the particle conservation on all of the species that compose the plasma, and the energy equilibrium on the electrons in order to capture the behaviour of their temperature. The equations that

govern the system are presented in the system of Equations 2.84

$$\begin{cases} \dot{n} = \dot{n}_{react} + \dot{n}_{walls} + \dot{n}_{ex} \\ \dot{T}_e = \frac{2(P_{abs} - P_{react} - P_{wall} - P_{ex}) - 3T_e\dot{n}_e}{3n_e} \end{cases} \quad (2.84)$$

Where \dot{n}_{react} , \dot{n}_{walls} , \dot{n}_{ex} are the variations in time per unit volume of the number of particles in each species due to, respectively, the plasma reactions, the neutralization and de-excitation at the source walls and the exhaust through the plume. P_{abs} , P_{react} , P_{wall} , P_{ex} are instead the power transferred to the electron population by the electromagnetic waves, and the power leaving the electron population in the source through reactions, neutralization at the source walls, and through the nozzle. All the powers are measured in eVs^{-1} while the electron temperature is measured in eV. The maximum power absorption and the coupling of the electric circuit to the antenna is simply linked to the total power provided to the thruster (P_{tot}) by means of an efficiency determined empirically: $P_{abs\ max} = \eta_{rf}P_{tot}$. Typical values of the power transfer efficiency lie between 60% and 95% [1]. Once all of the terms in the system of Equations 2.84 are known at each time step the governing equations may be integrated in time, by means of a variable step, variable order integration method based on the numerical differentiation formulas (i.e. the MATLAB function *Ode15s*), until steady state conditions are reached. A note on the introduction of the absorbed power is here mandatory. To aid the numerical stability of the integration the power absorbed by the electron population has not been introduced as a constant from the start of the integration. This, in fact, would lead to an overshooting of the electron temperature due to the high power inputs into a scarce electron population. The absorbed power has therefore been introduced following a time dependent exponential law presented in Equation 2.85.

$$P_{abs}(t) = P_{abs\ max} \left(1 - \exp\left(-\frac{t}{\tau}\right) \right) \quad (2.85)$$

With τ a time scale usually assumed equal to 10^{-4} . This is of course not only a numerical strategy but also a physically more accurate representation of the introduction of the power into the plasma: when the electron population is scarce the coupling between it and the electromagnetic wave is necessarily less efficient. It should however be underlined that there is no pretence of physical accuracy in the adoption of Equation 2.85: no interest is in fact given, at least to the ends of this thesis, to the transient at the thruster ignition and only the accuracy of the equilibrium reached in stationary conditions is considered.

In the following subsections the quantities necessary for the integration of Equation 2.84 are determined, starting from the initial conditions required to start the integration.

Initial Conditions

The initial conditions of the plasma inside the source are determined by assuming that the neutral particles expand through the thruster like they would do in a cold gas thruster with an isentropic, sonically choked expansion in the nozzle. Given the mass flux inserted into the thruster (\dot{m}) and the radius of the source outlet section (R_f), where sonic conditions are assumed and that is not necessarily equal to the source radius, the density of the neutral gas before the electromagnetic waves are induced into the source (n_{n0}) may be determined via

Equation 2.86.

$$n_{n0} = \frac{\dot{m}}{\pi R_f^2} \frac{\left(\frac{\gamma+1}{2}\right)^{\frac{\gamma+1}{2(\gamma-1)}}}{\sqrt{m_{Ar} \gamma k T_n}} \quad (2.86)$$

Where γ is the heat capacity ratio of Argon, roughly equal to 1.665 and m_{Ar} is the average mass of Argon isotopes, corresponding to 6.63×10^{-26} kg. Equation 2.86 can be easily obtained determining the density found at the nozzle throat and retracing it into the source by means of the isentropic expansion equations. These are of course valid when an adiabatic expansion can be assumed in the nozzle, which considering the low temperatures of the expanding gas is a sufficiently accurate description, and in the presence of a converging geometry capable of accelerating the gas to a unitary Mach number. The equation may however lose validity in the case of a very rarefied gas inside the source, whose behaviour is better modelled through the movement of its single particles than via fluid elements. Nevertheless, Equation 2.86 has been used to model the gas dynamics in the source because it is, in any case, the most accurate and simple description of the neutral gas expansion available and because the initial conditions are of relatively small importance, since the stationary equilibrium computed by the model shows a very small dependence on them. Once the initial density of the neutral gas is known the initial state of the system $(\underline{n}_0, T_{e0})$ can be determined through Equation 2.87

$$\left\{ \begin{array}{l} \underline{n}_0 = \begin{bmatrix} n_{n0} \\ 0 \\ 0 \\ \alpha_0 n_{n0} \\ \alpha_0 n_{n0} \end{bmatrix} \\ T_e = T_{e0} \end{array} \right. \quad (2.87)$$

With α_0 a proportionality coefficient usually assumed equal to 10^{-4} and $T_{e0} = 2$ eV the initial electron temperature. Once again these initial conditions have little pretence of physical accuracy: both the electron temperature and ion and electron densities are too high to correspond to an inert Argon gas. However they allow the accurate computation of the stationary plasma equilibrium, which is the output of interest of this model.

Plasma Reactions

As mentioned the reactions considered by the model are excitation and de-excitation, ionization and neutralization, and scattering. Argon is the eighteenth element in the periodic table, which means that its electrons fill up completely all of the inner orbitals including the 3P ones. Excitation therefore happens when one of the outer electrons absorbs energy and jumps into one of the higher orbitals. The energy gained by the electron during the excitation may come from the collision with any particle present in the plasma or from irradiation. Here, however, only collisions with electrons are considered, since they are by far the most energetic species in the plasma considered and since no waves capable of exciting Argon are present in the modelled thrusters. Furthermore, only excitations to the 4S and 4P orbitals are considered, provided that they are sufficient to predict the main plasma properties (i.e. density and temperature), and in turn the thrust. The 4S and the 4P orbitals in reality are composed of respectively four and ten energy levels, depending on which of the orbitals is considered and on the spin of the electron. For simplicity and brevity, however, the quantities regarding the

excitation the the 4S and 4P orbitals have been averaged over these energy levels, so that only two excited states may be taken into account. Three excitation reactions are therefore possible: the one that bring the outer electron from the ground state to the 4S orbitals, the one from the ground state to the 4P orbitals and the one from the 4S to the 4P orbitals. Of course all of the inverse de-excitation reactions have also been considered. Again, it has been supposed that de-excitation happens only via electron collision. While these collisions, because of the high electron temperatures, are much more frequent than the ones with the other species in the gas, which can therefore be neglected, spontaneous de-excitation might pay an important role in determining the equilibrium condition of the plasma and it therefore represents a direction of future development for the code. Spontaneous de-excitation, in fact, releases the energy under the form of electromagnetic radiation of a wavelength to which the Argon plasma is mostly transparent. This energy is therefore lost and gives the Argon plasma its characteristic blue glow. [3]

Likewise ionization is assumed to happen only because of electron collisions with neutral particles. Because of the presence of the excited species in the plasma ions can be formed in three ways: either by freeing an electron in the 3P orbitals, or by freeing an already excited electron in the 4S or 4P orbitals. Neutralization of the ions has instead been considered only at the source walls and not in the bulk of the plasma, since the flux of charged particles to the source boundaries is much more copious than the spontaneous collisions between ions and electrons. [8]

Finally various forms of elastic scattering have been considered. These reactions do not change the composition of the plasma since no new particles are formed, but they transfer energy from one species to another. Since the neutral and ion temperatures are considered constant only electron scattering is of interest from this point of view. Electrons may be scattered by elastic collisions with neutrals or by Coulomb scattering with other charged particles. In both cases, considering the collisions as perfectly elastic, the energy transferred from the electron to the target particle is of simple analytical computation: $\epsilon_{scat} = \frac{3m_e T_e}{m_{Ar}}$, with both the collision energy and the electron temperature expressed in electronVolts. [3] Other forms of collisions, namely the Langevin scattering and the charge exchange, have been included in the model in order to compute the ions' collision frequency. The former of these interactions sees the trajectory of an ion deviated by the electric dipole that its proximity forms in a neutral atom. The latter is a non-elastic collision between an ion and a neutral in which the ion steals an electron form the neutral atom. The total plasma composition, therefore, remains unvaried by this reaction, since the total number of neutrals and ions remains identical, but some energy is exchanged between the two particles. Table 2.2 contains all of the analytical expressions adopted to model the reaction rates (K), or collision cross-sections (σ) of the reactions described. Here Ar represents Argon at the ground state, Ar_{4S} and Ar_{4P} Argon with an electron excited into respectively the 4S and 4P orbitals, and Ar^+ the Argon atom singularly ionized. e in this context represents an electron. The ionization, excitation, de-excitation and elastic scattering reaction rates have been taken from fittings to empirical data presented in Reference [3] and valid for electron temperatures from 1 to 7 eV. The reaction rate of ion Langevin scattering has instead been modelled according to the analytical description found in Ref. [3], while the charge exchange cross-section has been calculated according to an empirical expression presented in the same Reference, and valid for ion velocities between $1 \times 10^3 \text{ m s}^{-1}$ and $1 \times 10^6 \text{ m s}^{-1}$. Finally the Coulomb scattering reaction rate, not present in Table 2.2, has been integrated, by means of the *Bolsig+* algorithm [59], assuming a Maxwellian electron distribution function from the empirical database of Reference [60]

In the expression for the Langevin reaction rate α_p is the polarizability of the atom, that for Argon assumes a value of roughly $\alpha_p = 11.08\alpha_0^3$, with α_0 the Bohr radius. Moreover ϵ_0 is the electric vacuum permittivity and $m_R = \frac{m_{Ar}}{2}$ the reduced mass. Finally v_i in the equation for the charge exchange cross section is the ion velocity. All the temperatures and energies in the

	Type	Formula	Characteristic Energy [eV]
$Ar + e \rightarrow Ar_{4S} + e$	Reaction rate [m^3s^{-1}]	$K_{G4S} = 5 \times 10^{-15} T_e^{0.74} \exp\left(\frac{-11.56}{T_e}\right)$	$\epsilon_{G4S} = 11.54$
$Ar_{4S} + e \rightarrow Ar_{4P} + e$	Reaction rate [m^3s^{-1}]	$K_{4S4P} = 8.9 \times 10^{-13} T_e^{0.51} \exp\left(\frac{-1.59}{T_e}\right)$	$\epsilon_{4S4P} = 1.36$
$Ar + e \rightarrow Ar_{4P} + e$	Reaction rate [m^3s^{-1}]	$K_{G4P} = 1.4 \times 10^{-14} T_e^{0.71} \exp\left(\frac{-13.2}{T_e}\right)$	$\epsilon_{G4P} = 12.9$
$Ar_{4S} + e \rightarrow Ar + e$	Reaction rate [m^3s^{-1}]	$K_{4SG} = 4.3 \times 10^{-15} T_e^{0.74}$	$\epsilon_{4SG} = 11.54$
$Ar_{4P} + e \rightarrow Ar_{4S} + e$	Reaction rate [m^3s^{-1}]	$K_{4P4S} = 3 \times 10^{-13} T_e^{0.51}$	$\epsilon_{4P4S} = 1.36$
$Ar_{4P} + e \rightarrow Ar + e$	Reaction rate [m^3s^{-1}]	$K_{4PG} = 3.9 \times 10^{-16} T_e^{0.71}$	$\epsilon_{4PG} = 12.9$
$Ar + e \rightarrow Ar^+ + 2e$	Reaction rate [m^3s^{-1}]	$K_{iz} = 2.34 \times 10^{-14} T_e^{0.59} \exp\left(\frac{-17.44}{T_e}\right)$	$\epsilon_{iz} = 15.76$
$Ar_{4S} + e \rightarrow Ar^+ + 2e$	Reaction rate [m^3s^{-1}]	$K_{iz4S} = 6.8 \times 10^{-15} T_e^{0.67} \exp\left(\frac{-4.20}{T_e}\right)$	$\epsilon_{iz4S} = 4.22$
$Ar_{4P} + e \rightarrow Ar^+ + 2e$	Reaction rate [m^3s^{-1}]	$K_{iz4P} = 1.8 \times 10^{-13} T_e^{0.61} \exp\left(\frac{-2.61}{T_e}\right)$	$\epsilon_{iz4P} = 2.86$
Elastic scattering	Reaction rate [m^3s^{-1}]	$K_{El} = 2.336 \times 10^{-14} T_e^{1.609} \exp(0.0618(\ln T_e)^2 - 0.1171(\ln T_e)^3)$	$\epsilon_{El} = \frac{3m_e T_e}{m_{Ar}}$
Langmuir scattering	Reaction rate [m^3s^{-1}]	$K_L = \left(\frac{\pi \alpha_p e^2}{\epsilon_0 m_R}\right)^2$	-
Charge Exchange	Cross-section [cm^2]	$\sigma_{cx} = \frac{1}{\epsilon_{iz}} (1.58 \times 10^{-7} - 7.24 \times 10^{-8} \ln(v_i))^2$	-

Table 2.2: Expressions for the reaction rates and cross-sections of the considered reactions [3]

table are expressed in electronvolts.

For every time instant, then, given the electron temperature the reaction rates of the collisions that modify the plasma composition or that change the energy in the electron population may be computed. The number of reactions per unit volume and time can then be obtained by multiplying them by the densities of the particles involved, as shown in Equation 2.90

$$\underline{\dot{y}} = \begin{bmatrix} \dot{y}_{G4S} \\ \dot{y}_{4S4P} \\ \dot{y}_{G4P} \\ \dot{y}_{4SG} \\ \dot{y}_{4P4S} \\ \dot{y}_{4PG} \\ \dot{y}_{iz} \\ \dot{y}_{iz4S} \\ \dot{y}_{iz4P} \\ \dot{y}_{El} \\ \dot{y}_C \end{bmatrix} = \begin{bmatrix} n_e n_n K_{G4S} \\ n_e n_{4S} K_{4S4P} \\ n_e n_n K_{G4P} \\ n_e n_{4S} K_{4SG} \\ n_e n_{4P} K_{4P4S} \\ n_e n_n K_{G4P} \\ n_e n_n K_{iz} \\ n_e n_{4S} K_{iz4S} \\ n_e n_{4P} K_{iz4P} \\ n_e (n_n + n_{4S} + n_{4P}) K_{El} \\ n_e n_i K_C \end{bmatrix} \quad (2.88)$$

The variation in the plasma composition due to the reactions may then be computed by multiplying the vector containing the number of collisions per second by an appropriate matrix, describing the species involved in each reaction, as shown in Equation 2.89.

$$\underline{\dot{n}}_{react} = \begin{bmatrix} -1 & 0 & -1 & 1 & 0 & 1 & -1 & 0 & 0 & 0 & 0 \\ 1 & -1 & 0 & -1 & 1 & 0 & 0 & -1 & 0 & 0 & 0 \\ 0 & 1 & 1 & 0 & -1 & -1 & 0 & 0 & -1 & 0 & 0 \\ 0 & 0 & 0 & 0 & 0 & 0 & 1 & 1 & 1 & 0 & 0 \\ 0 & 0 & 0 & 0 & 0 & 0 & 1 & 1 & 1 & 0 & 0 \end{bmatrix} \cdot \underline{\dot{y}} \quad (2.89)$$

Finally, by grouping the reaction energies, taken positive when the energy is given to the electrons and negative when it is taken from the electrons, in a vector, as shown in Equation 2.90 the energy variation in the electron population per unit time and volume due to the reactions can be computed.

$$\underline{\epsilon}_{react} = \begin{bmatrix} \epsilon_{G4S} \\ \epsilon_{4S4P} \\ \epsilon_{G4P} \\ -\epsilon_{4SG} \\ -\epsilon_{4P4S} \\ -\epsilon_{4PG} \\ \epsilon_{iz} \\ \epsilon_{iz4S} \\ \epsilon_{iz4P} \\ \epsilon_{El} \\ \epsilon_C \end{bmatrix} \quad (2.90)$$

$$P_{react} = \underline{\dot{y}} \cdot \underline{\epsilon}_{react} \quad (2.91)$$

Wall Losses

Another point in the source where there is a loss of charged and excited particles, as well as electron energy, are the source's lateral walls. The particles, in fact, by diffusing perpendicularly or along the confining magnetic field, reach respectively the radial or back and front walls of the source tube. All of the ions and electrons that reach the walls are considered to be neutralized, forming neutral, unexcited Argon atoms, and their energies are assumed to be lost. Similarly all of the excited particles that collide with the outer walls are assumed to return to the ground state, losing their energy. In order to model the neutralization of the charged particles at the walls the plasma diffusion along and across the field lines must first be described. [8]

With the scope of computing the diffusion coefficients of ions and electrons immersed in a magnetic field their collision frequencies must first be computed. In the ions' case Langevin scattering, charge exchange and Coulomb scattering have been considered as the reactions that most influence the mean free path and the total collision frequency, while for the electrons the elastic scattering has been considered, due to the low ionization ratios reached inside the source, as the type of reaction that constitutes the great majority of their collisions. All of the other impacts that involve the electron population have therefore been neglected. By considering the reaction rates corresponding to the temperatures of the particles considered the ion and electron collision frequencies (ν_i and ν_e) may then be computed using Equations 2.92 and 2.93.

$$\nu_i = (n_n + n_{4S} + n_{4P})(K_L(T_i) + K_{cx}(T_i)) + n_e K_C(T_e) \frac{v_i}{v_e} \quad (2.92)$$

$$\nu_e = (n_n + n_{4S} + n_{4P})K_{El}(T_e) \quad (2.93)$$

Where the charge exchange reaction rate (K_{cx}) has been obtained by integrating the cross-section presented in Table 2.2 over a Maxwellian distribution centred in the ion thermal energy [3]. Moreover v_i and v_e are the average electron and ion velocities, that have been assumed equal to the mean speed in a Maxwellian distribution: $v = \sqrt{\frac{8kT}{\pi m}}$ with T the particle's temperature in Kelvin and m its mass. These velocities are used in Equation 2.92 to pass from the collisional frequency due to Coulomb scattering perceived by the electrons to the one seen by the ions. With the knowledge of the collisional frequencies the diffusion and mobility coefficients parallel or perpendicular to the magnetic field (D, μ, D_{\perp} and μ_{\perp} respectively) can be computed for both electrons and ions using Equations 2.94 - 2.97.

$$D = \frac{kT}{m\nu} \quad (2.94)$$

$$\mu = \frac{e}{m\nu} \quad (2.95)$$

$$D_{\perp} = \frac{D}{1 + \left(\frac{eB}{m\nu}\right)^2} \quad (2.96)$$

$$\mu_{\perp} = \frac{\mu}{1 + \left(\frac{eB}{m\nu}\right)^2} \quad (2.97)$$

Where B is the magnetic induction assumed uniform and paraxial inside the source. The global plasma diffusion, however, is a more complex phenomenon than the diffusivity of the single particles taken independently. To maintain quasi-neutrality and enforce an equal diffusion of the two species towards the walls, in fact, an ambipolar electric field arises inside the plasma. Along the field lines, where the different magnetization of ions and electrons has no constraining effect on their mobility the ambipolar diffusion coefficient may be computed as shown in Equation 2.98. In the direction perpendicular to the magnetic field, instead, the diffusion coefficient is of more complex determination. At high magnetic fields, in fact, due to their lower mass the electrons are strongly confined by the field lines and their perpendicular diffusion is strongly inhibited. At the limit condition, therefore all of the electrons will diffuse axially along the field lines, while only ions will be able to cross the field lines and diffuse to the outer radial walls. This condition can be roughly modelled using the diffusion coefficient computed in Equation 2.99 and demonstrated in Reference [3] (hereafter denoted the Lieberman diffusion coefficient). When the magnetic induction is low, however, both ions and electrons become capable of diffusing perpendicularly to the field lines, and the corresponding diffusion coefficient becomes similar to the one found in the axial direction, as presented in Equation 2.100. To capture both of these conditions the two diffusion coefficients have been merged and weighed using Equation 2.101. Here λ_D is a weighing coefficient found empirically to be, as will be discussed in Chapter 3 0.8 for fields below the 200 G mark and unitary for fields of higher intensity.

$$D_{a\parallel} = \frac{\mu_i D_e + \mu_e D_i}{\mu_i + \mu_e} \quad (2.98)$$

$$D_{L\parallel} = \mu_{i\perp} T_e \quad (2.99)$$

$$D_{a\perp} = \frac{\mu_{i\perp} D_{e\perp} + \mu_{e\perp} D_{i\perp}}{\mu_{i\perp} + \mu_{e\perp}} \quad (2.100)$$

$$D_{tot\perp} = exp[(1 - \lambda_D) \ln(D_{a\perp}) + \lambda_D \ln(D_{L\perp})] \quad (2.101)$$

Having determined the diffusion coefficients that characterize the plasma its density at the source boundaries may now be computed. To do this the Godyak expressions for a cylindrical geometry presented in Ref. [3] have been adopted. These relations join heuristically the solutions to the diffusion equations found for the collisionless, variable mobility and constant diffusion regimens, so as to compute the plasma density at its boundaries in function of the diffusion coefficient. Through the Godyak expressions, presented in Eqs 2.102 and 2.103, the ratio between the plasma density at the centre of the source and that at its radial boundaries (h_R) and axial boundaries (h_L) may be found.

$$h_R = \frac{0.8}{\left[4 + \frac{R_s}{\lambda_i} + \left(\frac{0.8 R_s u_b}{\chi_{01} J_1(\chi_{01}) D_{tot\perp}}\right)^2\right]^{\frac{1}{2}}} \quad (2.102)$$

$$h_L = \frac{0.86}{\left[3 + \frac{L_s}{2\lambda_i} + \left(\frac{0.86 L_s u_b}{\pi D_{a\parallel}}\right)^2\right]^{\frac{1}{2}}} \quad (2.103)$$

Where $\lambda_i = \frac{v_i}{\nu_i}$ is the ion mean free path, χ_{01} is the first zero of the zero order Bessel function and J_1 is the first order Bessel function. Before using this result to compute the losses linked to the particle fluxes to the walls, however, the modelling of eventual cusp lines must be tackled.

The magnetic field inside the source, in fact, can be produced in several ways. One of the most straight forward is to use a series of coils wrapped around the source to induce a constant and roughly axial magnetic field. When using permanent magnets, however, another possibility is to alternate rings of magnets with opposite polarities and with a radial magnetic dipole. The magnetic fields produced by these magnet rings merge inside the source forming, at a small distance from the outer walls, a constant axial field as shown in Figure 2.3 [8].

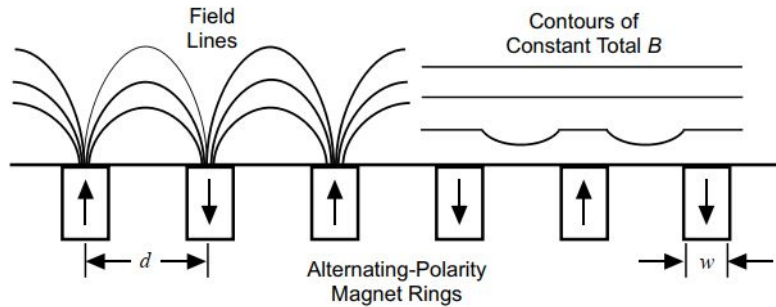


Figure 2.3: Geometry of the magnetic field produced by rings of radial magnets.

As can be seen, however, in proximity of the magnets the magnetic field forms a cusp, where the field lines are oriented radially. The diffusion in this region will therefore not be impeded by the confining magnetic field since the particles will not have to cross the field lines to reach the radial wall, and a different diffusive model will be necessary. To this end the thickness of the cusp region in the axial direction can be computed, as demonstrated by Refs. [3] and [8] following Equation 2.104.

$$d_{cusp} = 4\sqrt{r_{ci}r_{ce}} \quad (2.104)$$

Where r_{ci} and r_{ce} are the ion and electron Larmor radii, computed using the mean speeds of the two species. Given the number of magnet rings used to generate the magnetic field inside the source (n_{cusps}), the area of the radial wall where the field lines can be assumed to be directed radially (A_{cusps}) can be calculated using Equation 2.105. The plasma density found in the cusp regions may then be computed using the radial Godyak expression in function of the parallel ambipolar diffusion coefficient $D_{a||}$ to determine h_{cusp} .

$$A_{cusps} = n_{cusps}d_{cusp}2\pi R_s \quad (2.105)$$

Finally, an effective loss area (A_{eff}) that includes the plasma density at the source walls can be computed by means of Equation 2.106, and, imposing the Bohm criterion, used in Eq. 2.107 to determine the number of ions and electrons neutralized at the source walls per unit volume and time ($\dot{n}_{i\ wall}$, $\dot{n}_{e\ wall}$).

$$A_{eff} = h_L(2\lambda\pi R_s^2 - \lambda\pi R_f^2) + h_R(2\pi R_s L_s - A_{cusps}) + h_{cusp}A_{cusps} \quad (2.106)$$

$$\dot{n}_{i\ wall} = \dot{n}_{e\ wall} = \frac{n_i u_B A_{eff}}{\pi R_s^2 L_s} \quad (2.107)$$

The coefficient λ employed in Eq. 2.106 has been used to pass from the plasma density on the source axis to the radially averaged density, and can be computed by inserting the h_R coefficient determined into Equation 2.68. The use of the ion or electron density in Eq. 2.107 is indifferent as, due to their origin and loss mechanisms, the two densities must be equal.

Considering a Maxwellian distribution and a uniform density profile the flow of excited atoms towards the source walls, and therefore the number of de-excitations per unit time and volume may also be computed by means of Equations 2.108 and 2.109. Here $v_{wall} = \frac{v_n}{4}$ is the mean flow velocity of the excited species in any given direction, corresponding to a quarter of the mean velocity module.

$$\dot{n}_{4S\,wall} = \frac{n_{4S}v_{wall}(2\pi R_s L_s + 2\pi R_s^2 - \pi R_f^2)}{\pi R_s^2 L_s} \quad (2.108)$$

$$\dot{n}_{4P\,wall} = \frac{n_{4P}v_{wall}(2\pi R_s L_s + 2\pi R_s^2 - \pi R_f^2)}{\pi R_s^2 L_s} \quad (2.109)$$

The variation in the plasma composition due neutralizations and de-excitations at the walls therefore corresponds to:

$$\dot{n}_{wall} = \begin{bmatrix} \dot{n}_{i\,wall} + \dot{n}_{4S\,wall} + \dot{n}_{4P\,wall} \\ -\dot{n}_{4S\,wall} \\ -\dot{n}_{4P\,wall} \\ -\dot{n}_{i\,wall} \\ -\dot{n}_{e\,wall} \end{bmatrix} \quad (2.110)$$

Finally, the energy transported to the wall by an ion and electron pair in an ideal stationary plasma sheath can be computed using Equation 2.111 [3]. The energy lost by the electron population per unit time and volume through neutralization at the wall can therefore be calculated through Eq. 2.112. The full energy linked to the ion and electron pair is thus assumed to be taken only from the electron population. This assumption has to be made due to the impossibility of determining what portion of the energy found at the source walls comes from the ion or electron populations using the analytical sheath theory. Because the electrons are by far the more energetic population, however, it results a reasonable hypothesis.

$$\epsilon_{wall} = \left[\frac{5}{2} + \frac{1}{2} \ln \left(\frac{m_i}{2\pi m_e} \right) \right] T_e \quad (2.111)$$

$$P_{wall} = \dot{n}_{i\,wall} \epsilon_{wall} \quad (2.112)$$

Exhaust losses

The last sink that absorbs the plasma particles, reducing their density inside the source, is the thruster exhaust. Its description, however, depends on the magnetic nozzle model adopted. A choked magnetic or physical nozzle, in fact, imposes constant and stationary conditions at the source exit. Four possible magnetic nozzle models have been integrated into the presented global source model: the Lafleur MN model, the Modified Martinez-Sanchez model and two versions of the original MS model: one where the plasma undergoes the full expansion in

the convergent-divergent nozzle and so the plasma density and temperature in the source are used to normalize the plasma properties in the nozzle; and one where the expansion starts in the position along the convergent where the nozzle's magnetic field matches the one found in the source. In this latter case stagnation quantities must be computed and used to return to dimensional quantities in the nozzle. It should be noted that the arrangement in which a simply divergent nozzle is attached to the source is a particular condition of the latter MS model application, in which the magnetic field in the source corresponds to the one found in the magnetic throat.

Lafleur Nozzle Model When the Lafleur MN model is used a stationary plasma sheath has been assumed at the source exhaust, and sonic conditions have been imposed at the nozzle entrance. The computation of the ion and electron flux per unit volume out of the source (\dot{n}_{iex} and \dot{n}_{eex}) is therefore analogous to the one used to determine the fluxes at the source's axial walls, as shown by Equations 2.113.

$$\dot{n}_{iex} = \dot{n}_{eex} = \frac{\lambda h_L n_i u_b \pi R_f^2}{\pi R_s^2 L_s} \quad (2.113)$$

The energy carried out of the source by a single electron and ion pair (ϵ_{ex}) can instead be computed using Eq. 2.114, as demonstrated by Lafleur [1], where M_{det} is the plasma Mach number at the detachment location. Once this is known the energy flux escaping out of the nozzle per unit volume (P_{ex}) can be trivially computed by means of Eq. 2.115.

$$\epsilon_{ex} = \frac{5}{2} T_e + \frac{1}{2} T_e M_{det}^2 \quad (2.114)$$

$$P_{ex} = \dot{n}_{iex} \epsilon_{ex} \quad (2.115)$$

Modified Martinez-Sanchez Model When using the MMS model sonic conditions at the source exit, corresponding to the nozzle throat, have been imposed. While the nozzle model considered requires only the atom mass and their kinetic energy at the nozzle entrance as inputs, which are both known due to the assumption of a unitary Mach number and the knowledge of the Bohm velocity, its outputs are adimensional and the normalization electron temperature and plasma density must be determined to return to dimensional quantities. These are the quantities found at the source exhaust. The normalization electron temperature is therefore the electron temperature in the source, assumed to be uniform in the whole domain, while the plasma density at the source exhaust may be computed as $n_s = h_L n_i$, taking advantage of the previously determined axial density profile. Once again here the use of the ion or electron density is indifferent. Once these quantities are known the particle flux and the energy transported out of the nozzle may be computed using Eqs. 2.116 and 2.117.

$$\dot{n}_{iex} = \dot{n}_{eex} = \frac{\lambda h_L n_i u_b \pi R_f^2}{\pi R_s^2 L_s} \quad (2.116)$$

$$P_{ex} = \frac{\lambda h_L n_i u_b T_e R_f^2 (\dot{\epsilon}_{ith} + \dot{\epsilon}_{eth})}{\pi R_s^2 L_s} \quad (2.117)$$

Where $\dot{\epsilon}_{ith}$ and $\dot{\epsilon}_{eth}$ are the adimensional ion and electron kinetic energy fluxes computed by the MMS model at the nozzle entrance.

Full Martinez-Sanchez Model In the case of the use of the full expansion in the original Martinez-Sanchez model it has been assumed to start at the centre of the source, meaning that the normalization quantities necessary to pass from the adimensional model outputs to physical plasma properties, are the ones computed, instant by instant, by the global model. This implies that the expansion towards the source exhaust considered for this model is not the one described by the computed diffusion coefficients and density ratios, but the one predicted by the MS model inside the convergent portion of the nozzle. As will be seen, however, these two expansions result quite similar from the perspective of the global source model, since they both impose at the source exit a Mach number close to unity and similar plasma densities. A few words should be also spent on the normalized ion energy ϵ_i necessary to run the Martinez-Sanchez model, and that has been hypothesised constant. The iterative procedure described in Section 2.1.2 to determine the exact value of this coefficient was initially implemented at each integration time step, but it resulted in much higher computational times and nearly identical results to the case in which ϵ_i was assumed fixed and constant. This is because, as explained, at values lower than 0.01 this parameter is found to have little influence on the model outputs. For values lower than this threshold, therefore, the normalized ion energy has been assumed constant, and typically equal to 0.008. Once the outputs from the MS model are known the particle and energy fluxes per unit volume escaping through the exhaust can be determined through Equations 2.118 and 2.119. Where \tilde{n}_{ith} , \tilde{v}_{ith} , $\dot{\epsilon}_{ith}$ and $\dot{\epsilon}_{eth}$ are the adimensional ion density, velocity and kinetic energy flux, along with the electron kinetic energy flux, computed by the MS model at the nozzle throat.

$$\dot{n}_{iex} = \dot{n}_{iex} = \frac{\lambda n_i u_b \pi R_f^2 \tilde{n}_{ith} \tilde{v}_{ith}}{\pi R_s^2 L_s} \quad (2.118)$$

$$P_{ex} = \frac{\lambda n_i u_b \pi R_f^2 T_e (\dot{\epsilon}_{ith} + \dot{\epsilon}_{eth})}{\pi R_s^2 L_s} \quad (2.119)$$

Partial Martinez-Sanchez Model Finally, the case in which the MS model is used, but with the expansion starting from the point in the convergent where the magnetic induction matches the one found in the source. is analogous to the case previously described but with the additional necessity of computing stagnation quantities (T_{0e} and n_{0e}) with which to return to dimensional quantities from the normalized model outputs. To this end the stagnation temperature can be calculated through the use of Equation 2.35, where T_{se} is the electron temperature in the source. The electron density at the nozzle entrance (n_{se}) may then be computed via Equation 2.120, where M_s is the Mach number at the nozzle entrance, calculated as $M_s = \frac{\tilde{v}_s \sqrt{\frac{eT_{0e}}{m_i}}}{u_b}$, with \tilde{v}_s the adimensional velocity found by the model at the nozzle entrance. The stagnation density may then be computed through Equation 2.36.

$$n_{se} = \frac{n_e}{1 + M_s^2} \quad (2.120)$$

Once the stagnation density and temperature are known the particle and energy flux out of the nozzle may be computed using Eqs. 2.121 and 2.122, where $u_{b0} = \sqrt{\frac{eT_{0e}}{m_i}}$ is the Bohm velocity computed at the stagnation temperature.

$$\dot{n}_{iex} = \dot{n}_{iex} = \frac{\lambda n_{e0} u_{b0} \pi R_f^2 \tilde{n}_{ith} \tilde{v}_{ith}}{\pi R_s^2 L_s} \quad (2.121)$$

$$P_{ex} = \frac{\lambda n_{i0} u_{b0} \pi R_f^2 T_{e0} (\dot{\epsilon}_{ith} + \dot{\epsilon}_{eth})}{\pi R_s^2 L_s} \quad (2.122)$$

Finally, to completely characterize the exhaust losses, the flux of the neutral particles out of the nozzle must be computed. To this end, once again, an isentropic expansion in the physical nozzle at the end of the plasma source has been hypothesised. By using the isentropic expansion relations and employing the quantities relative to the neutral species that is being considered the number of particles per unit time and volume leaving the source through the exhaust may be computed with Equation 2.123.

$$\dot{n} = \frac{n \pi R_f^2 \sqrt{\gamma m_{Ar} k T_n} \left(\frac{2}{\gamma+1} \right)^{\frac{\gamma+1}{2(\gamma-1)}}}{m_{Ar} \pi R_s^2 L_s} \quad (2.123)$$

The variation of the number of particles in the source due to the exhaust may then be grouped as:

$$\dot{n}_{ex} = \begin{bmatrix} \dot{n}_{nex} \\ \dot{n}_{4Sex} \\ \dot{n}_{4Pex} \\ \dot{n}_{iex} \\ \dot{n}_{eex} \end{bmatrix} \quad (2.124)$$

Thrust Computation

Now that all of the particle and energy sinks and sources have been described Equation 2.84 may be integrated, determining the right hand side at each time step in function of the particle densities and electron temperature. This results in a time dependant profile of the system's state, where as already mentioned the result of interest is the steady state equilibrium reached. Once the stationary plasma conditions in the source are known the thrust offered by the complete thruster system may be computed. The thrust component due to the charged particles is obtained as described in Section 2.1 according to the MN model utilized, while the attachment of the models to the source has been done identically to the one described for the determination of the exhaust losses and, for brevity, will not be repeated here. The thrust component due to the neutral particles, instead, can once again be computed by assuming their isentropic expansion inside of a physical nozzle of expansion ratio ϵ_{exp} . As mentioned the isentropic hypothesis reaches its limit in the case of a very rarefied gas, whose behaviour is better modelled by statistical mechanics. However the small contribution of the neutral particles to the total thrust mitigate the errors due to this assumption. The Mach number found at the nozzle exhaust (M_{ex}) can therefore be obtained implicitly through Equation 2.125.

$$\epsilon_{exp} M_{ex} = \left(\frac{2}{\gamma+1} + M_{ex}^2 \frac{\gamma-1}{\gamma+1} \right)^{\frac{\gamma+1}{2(\gamma-1)}} \quad (2.125)$$

The temperature (T_{nex}), velocity (v_{nex}), density (n_{nex}) and pressure (p_{nex}) of the neutral flow at the exhaust of the physical nozzle may then be computed using Equations 2.126 to 2.129.

$$T_{nex} = \frac{T_n}{1 + M_{ex}^2 \frac{\gamma-1}{2}} \quad (2.126)$$

$$v_{n\ ex} = M_{ex} \sqrt{\gamma R_{Ar} T_{ex}} \quad (2.127)$$

$$n_{n\ ex} = (n_n + n_{4S} + n_{4P}) \left(1 + M_{ex}^2 \frac{\gamma - 1}{2} \right)^{\frac{1}{1-k}} \quad (2.128)$$

$$p_{n\ ex} = eT_n (n_n + n_{4S} + n_{4P}) \left(1 + M_{ex}^2 \frac{\gamma - 1}{2} \right)^{\frac{k}{1-k}} \quad (2.129)$$

Finally the thrust due to the neutral particles (F_n) can be found using Equation 2.130, and the total thrust provided by the thruster (F_{tot}) is then trivially found with Eq. 2.131.

$$F_n = \pi R_f^2 \varepsilon_{exp} (m_{Ar} n_{n\ ex} v_{n\ ex}^2 + p_{n\ ex}) \quad (2.130)$$

$$F_{tot} = F_n + F_{plasma} \quad (2.131)$$

Chapter 3

Model Verification and Comparison

The models presented in Chapter 2 have been verified by comparing, where possible, the results obtained to the ones presented in their respective References. Where, instead, no benchmark results were available other verification processes have been considered. In particular the Lafleur nozzle and source models presented in Sections 2.1.1 and 2.2.1 have been verified against the results presented in Reference [1], while the Martinez-Sanchez MN model has been compared with the conclusions of Reference [2] and, where these were not sufficient to validate all of the computations done, with considerations of physical nature. The Modified Martinez-Sanchez model, instead, has been verified against the results of the full MS model of which it is a simplification, checking that the assumptions made have not undermined the accuracy of the algorithm. Finally, while no direct references were available for the global source model developed, some of the main assumptions adopted, namely the expressions for the diffusion coefficients, the empirical radial distribution function, and the collision rates, have been validated against empirical data and compared with alternative expressions. The most relevant verifications have been presented in Section 3.1, while the more straight forward ones, for the sake of brevity, have not been shown.

In Section 3.2, instead, the results of the developed models have been compared and critically analysed. The typical results offered by the detachment criteria and the divergence efficiency algorithm have also been presented here, along with their interaction with the nozzle models and their influence on the computed total thrust. At the end of this Section considerations on the numerical and computational properties of the models have also been made.

3.1 Verification

3.1.1 Lafleur Models

As mentioned the implementation of the Lafleur source model, nozzle model and detachment criteria have been verified against the results presented in Reference [1]. To this end the source model has been run, together with the MN Lafleur model and the detachment criterion with the input parameters presented in Table 3.1. The computed thrust and the propellant utilization efficiency obtained in function of the total input power can be seen in Figure 3.1. Here the continuous lines corresponds to the results obtained by the implemented model, while the full circles are data-points taken from Figures 6 and 8 of Reference [1]. In panel (a) the black line represents the full thrust provided by the modelled thruster while the blue line corresponds to the portion of thrust due to the presence of the magnetic nozzle. As can be seen Lafleur's model roughly predicts a doubling in the propulsive properties of a cathodeless thruster through the addition of the magnetic nozzle.

As can be appreciated in Figure 3.1 the implemented model follows faithfully the benchmark

Parameter	Value	Units
Source radius (R_s)	3.25	cm
Source length (L_s)	12	cm
Mass flux (\dot{m})	0.72	mg s ⁻¹
Source magnetic field (B_s)	171.5	G
Throat magnetic field (B_{th})	269	G
Wave coupling efficiency (η_{rf})	0.9	—

Table 3.1: Thruster parameters used to validate the Lafleur models

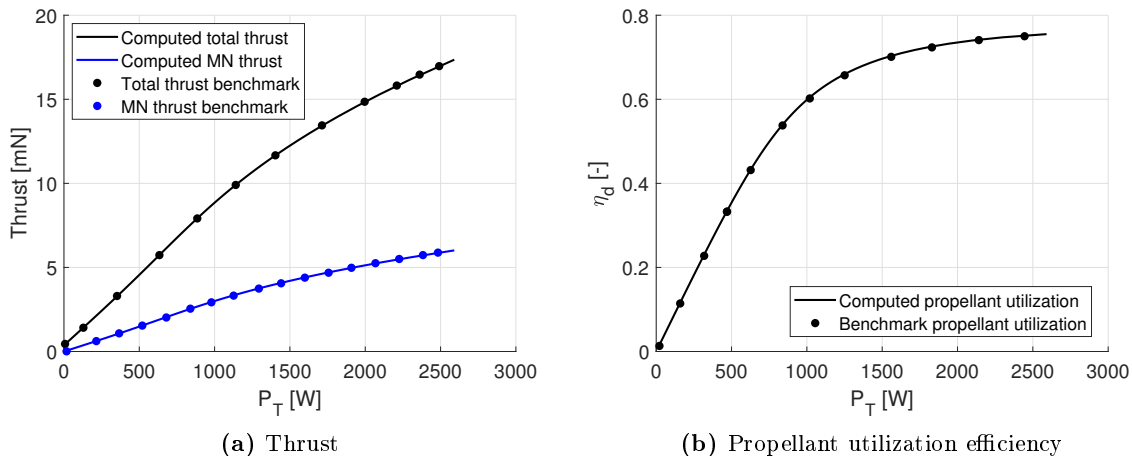


Figure 3.1: Comparison between the computed results and the ones presented in Reference [1]. Panel (a) shows the total thrust (black line) and the thrust provided by the magnetic nozzle (blue line) as function of the total provided power (P_T). Panel (b) plots the propellant utilization efficiency (η_d) against the total provided power. In both panels the continuous lines represent our results and the circular markers the benchmark data.

data-points, with a maximum relative error between the model and the reference values of roughly 0.5%. This implies that all three components of the model have been correctly coded: as explained in Chapter 2, in fact, the Lafleur source model, MN model and detachment criterion all contribute to the computation of both the thrust and the propellant utilization efficiency.

3.1.2 Martinez-Sanchez Model

The Martinez-Sanchez model is the most complex nozzle algorithm presented in this thesis, and it has, therefore, been thoroughly verified. Figures 4, 5, 6 and 7 of Reference [2] have been replicated and compared, in order to validate the computations of the potential, plasma density, velocity, and electron and ion temperatures along the nozzle. Moreover in order to verify Equations 2.27 to 2.32, that have been autonomously derived, the energy conservation principle and the definition of the average kinetic energy have been utilized. Finally, for those cases in which no validation principles have been found some simple physical considerations can be invoked in order to justify the solutions found. For the sake of brevity only the most important and relevant validations of this model are presented here.

The fundamental output of the Martinez-Sanchez model is the ambipolar potential that arises inside the nozzle. This is in fact the variable that grants the minimization of the quasi-neutrality and current errors, and that is then used to compute all of the plasma properties

throughout the expansion. To verify the computation of this important value the model has been evaluated for a value of the normalized initial ion energy $\epsilon_i = 0.1$ and for three mass ratios $m_{ratio} = 10^3, 10^4, 10^5$, imposing a desired net current inside the nozzle $\tilde{j} = 0$ and utilising a weight in the error computation of Eq. 2.20 of $K = 35$. The results have then been compared with data-points taken from Figure 4 of Ref. [2]. As can be seen in Figure 3.2, where the adimensional potential Φ is plotted against the magnetic field along the nozzle normalized by its maximum value (β), the implemented code matches well with the data-points taken from the paper, with a maximum relative error of 3%. The small discrepancies present may be attributed either to the unknown value of the weight K utilised by the authors, to the different optimization algorithms adopted, or to a different initial guess.

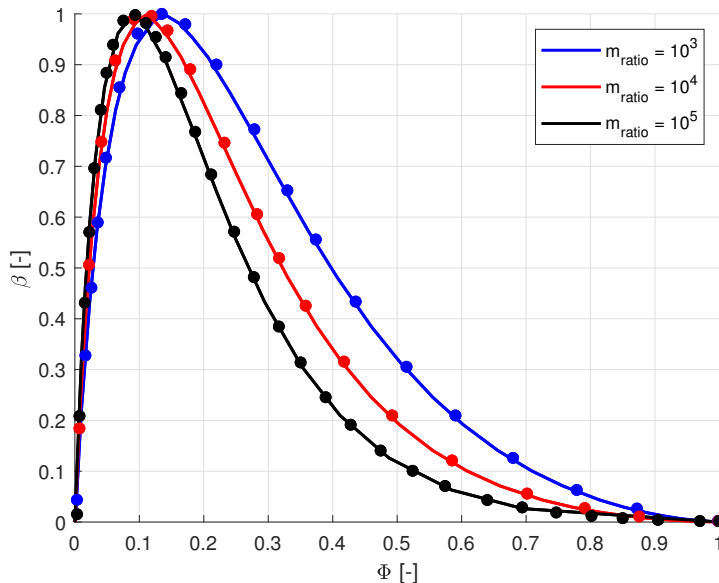


Figure 3.2: Normalized magnetic induction (β) and corresponding adimensional potential (Φ) along the nozzle for the different values of mass ratios considered. The blue, red and black lines represent respectively the results obtained from the implemented model for $m_{ratio} = 10^3, 10^4, 10^5$. The circular markers, of matching colours are the reference data-points.

The other two plasma properties that are fundamental for the correct utilisation of the model, as they directly enter the error to be minimized, and for the computation of the propulsive properties of the thruster are the normalized plasma density and velocity along the nozzle. These have been computed for an initial adimensional ion energy $\epsilon_i = 0.1$ and a mass ratio $m_{ratio} = 10^3$, while the prescribed net current and weight parameter have been fixed at $\tilde{j} = 0$ and $K = 35$. The results, expressed as a function of the normalized potential Φ and compared with the data-points taken from Figure 5 of Ref [2], are shown in Figure 3.3. Once again the computed values have been presented as a continuous line, while the filled circles represent the benchmark data-points. As previously an excellent agreement has been found between the implemented model and the reference data, with maximum relative deviations of 5% for the density, and 1% for the velocity. It is interesting to note that the velocity found by the model at the magnetic throat (marked with a cross in panel (b)), normalized by the Bohm velocity computed in the reservoir, is slightly larger than one. Since the electron temperature decreases along the nozzle the local Mach number at the throat ($M \approx 1.08$) implies a slightly supersonic speed. While this clashes slightly with the classical assumption of a sonic velocity in the nozzle's throat it is in agreement with recent experimental data [42].

Equations 2.31 and 2.32, used to compute the kinetic energy fluxes of ions and electrons, cannot be compared with any of the results presented by Martinez-Sanchez, but can be val-

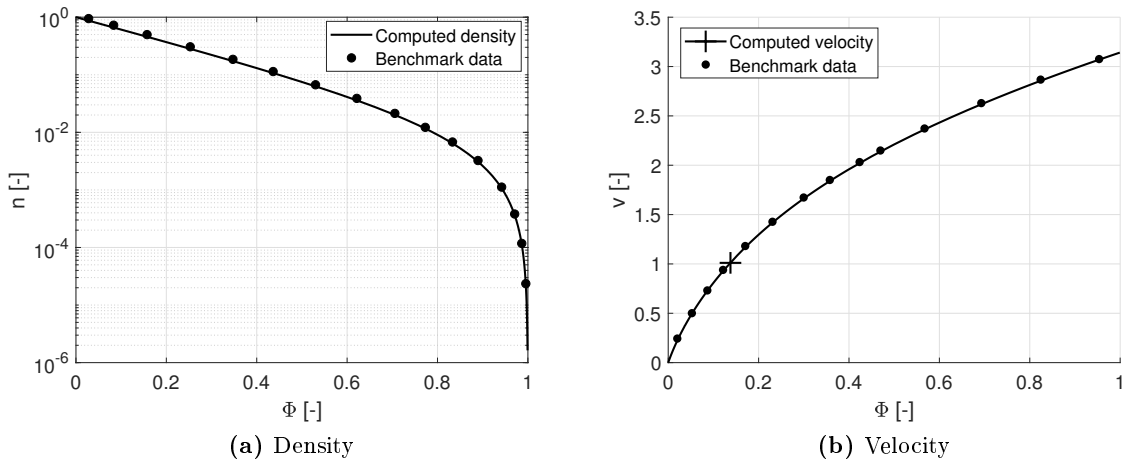


Figure 3.3: Normalized plasma density (n) and velocity (v) in function of the adimensional electric potential (Φ). In both panels the continuous line represents the obtained results and the circular markers the reference data. In panel (b) the cross-shaped marker indicates the magnetic throat and the corresponding velocity normalized by the Bohm velocity in the source.

idated by verifying that the conservation of energy is respected. Indeed, since the magnetic nozzle does not impart any work onto the plasma beam, because the magnetic forces are always by definition perpendicular to the particles' velocities, the total energy flux computed in each point of the nozzle must be constant. Once again to verify this the model has been run with $\epsilon_i = 0.1$, $m_{ratio} = 10^3$, $\tilde{j} = 0$ and $K = 35$. As shown by Figure 3.4, where the black and red lines represent respectively the specific ion and electron kinetic energy fluxes ($\dot{\epsilon}_i$ and $\dot{\epsilon}_e$) along the nozzle, while the blue line is the total kinetic energy flux (\dot{E}_{tot}), computed by multiplying the total specific energy flux by the local cross-section of the plasma beam as shown in Equation 3.1. Here the area of the plasma beam has been computed by invoking the conservation of the magnetic flux $A = \frac{A_{th}}{\beta}$, where A_{th} is area of the magnetic throat and β is the local magnetic induction, normalized by the magnetic field in the throat. As shown by Figure 3.4 the total kinetic energy flux is constant and the conservation of energy is respected.

$$\dot{E}_{tot} = \frac{A_{th}}{\beta} (\dot{\epsilon}_i + \dot{\epsilon}_e) \quad (3.1)$$

Finally, no benchmark data is available to validate equations 2.27 to 2.30. However, for the ions, it can be demonstrated that Equation 3.2 must hold, where $\langle \tilde{E}_i \rangle$ is the average ion kinetic energy in a given point of the nozzle, while $\langle \tilde{v}_{\parallel i} \rangle$ and $\langle \tilde{v}_{\perp i} \rangle$ are respectively the average parallel and perpendicular ion velocities.

$$\langle \tilde{E}_i \rangle = \frac{1}{2} (\langle \tilde{v}_{\parallel i} \rangle^2 + \langle \tilde{v}_{\perp i} \rangle^2) \quad (3.2)$$

By reverting to the moments of the distribution function (f_i , expressed in Eq. 2.8) and to dimensional physical variables, in fact, Equation 3.2 can be rewritten as:

$$\frac{1}{2} m_i \iiint_{\mathbf{v}} v^2 f_i(\mathbf{v}) d\mathbf{v} \frac{1}{n} = \frac{1}{2} m_i \left[\left(\iiint_{\mathbf{v}} v \cos(\alpha_i) f_i(\mathbf{v}) d\mathbf{v} \right)^2 \frac{1}{n^2} + \left(\iiint_{\mathbf{v}} v \sin(\alpha_i) f_i(\mathbf{v}) d\mathbf{v} \right)^2 \frac{1}{n^2} \right]$$

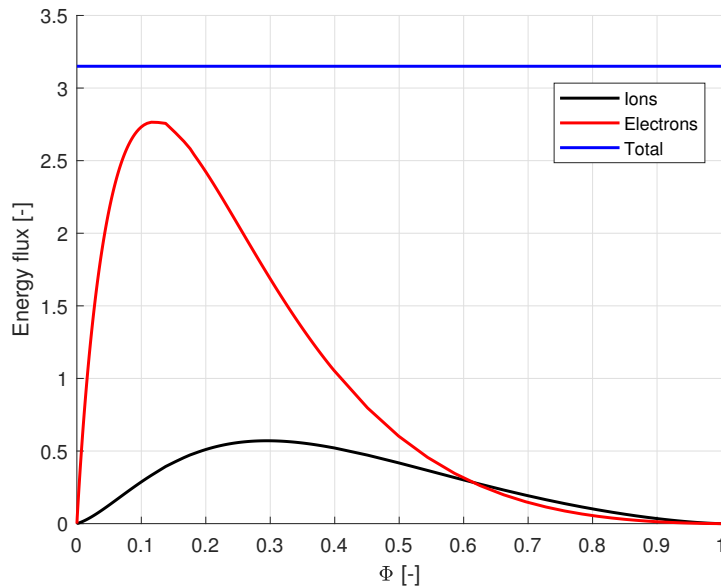


Figure 3.4: Kinetic energy fluxes along the nozzle. The total kinetic energy flowing through the nozzle (blue line), and the local kinetic energy fluxes of ions (black line) and electrons (red line) at each point of the nozzle are plotted against the normalized potential (Φ).

(3.3)

Where α_i is the angle between the velocity vector considered (\underline{v}) and the axial direction. Invoking, now, the orthogonality of sines and cosines, and thanks to the presence of the Dirac delta in the ion distribution function, the exponent may be brought inside the integral and an identity is reached, as shown in Eq. 3.4. The same cannot be done for the electrons because of their much more complex distribution function, which does not allow the passage from Eq. 3.3 to Eq. 3.4. Nevertheless, the validation of the expressions of the ion perpendicular velocity and specific kinetic energy by means of Equation 3.2 can be appreciated in Figure 3.8

$$\frac{1}{2}m_i \iiint_{\underline{v}} v^2 f_i(\underline{v}) d\underline{v} \frac{1}{n} = \frac{1}{2}m_i \iiint_{\underline{v}} v^2 (\cos^2(\alpha_i) + \sin^2(\alpha_i)) f_i(\underline{v})^2 d\underline{v} \frac{1}{n^2} \quad (3.4)$$

While no way has been found to validate Equations 2.28 and 2.30, some physical considerations can be made to justify the results obtained. By running once more the model with the usual parameters ($\epsilon_i = 0.1$, $m_{ratio} = 10^3$, $\tilde{j} = 0$ and $K = 35$) the electron specific kinetic energy (E_e) and the electron average perpendicular velocity ($v_{\perp e}$) presented in Figure 3.6 can be found. The former, found in panel (a), displays a physically intuitive behaviour when considering that it has been normalized by the electron thermal energy in the reservoir. At the start of the expansion, in fact, the kinetic energy results 1.5 times the thermal energy, as expected from a full Maxwellian distribution in three dimensions. As the expansion proceeds, instead, the electrons' kinetic energy decreases due to the presence of a negative potential, that tends to repel them towards the reservoir, but does not reach zero allowing for a non-null particle flux along the nozzle. The average perpendicular velocity, presented in panel (b), can be similarly analysed. Its initial value, in fact, corresponds to the one expected from a perfect Maxwellian distribution, and decreases as the electrons advance downstream and the perpendicular velocity is transferred into the axial direction by the magnetic nozzle effect. At the end of the expansion the perpendicular velocity of the electrons approaches zero, as all of it has been converted into the axial component of the velocity.

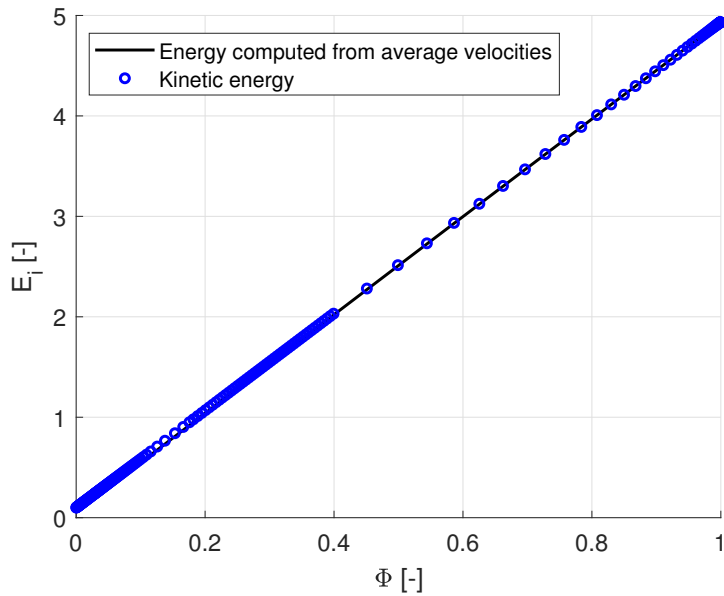


Figure 3.5: Verification of Equation 3.2. The results of the right hand side of the equation (black line), and the normalized specific ion kinetic energy computed by the MS model (blue open circles) are plotted against the normalized local potential (Φ).

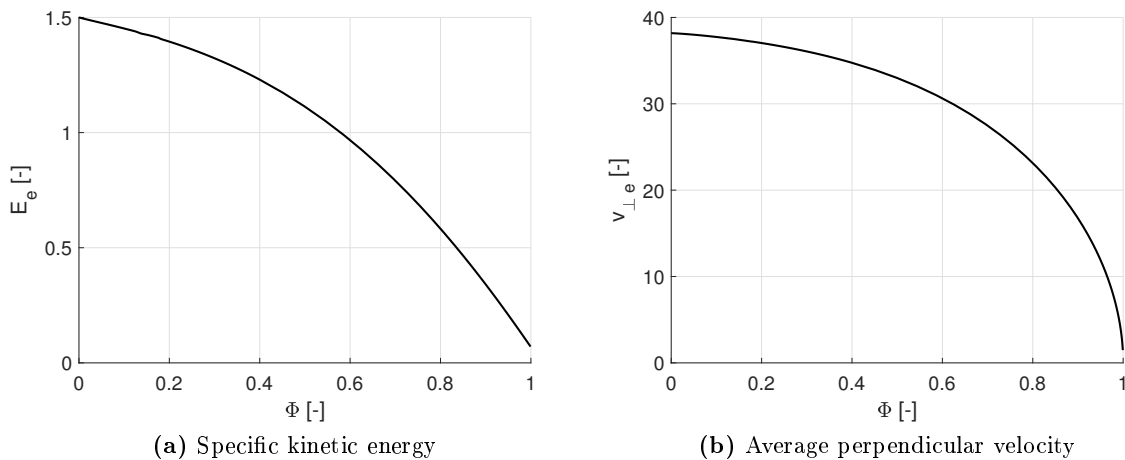


Figure 3.6: Normalized electron specific kinetic energy (E_e) and average perpendicular velocity ($v_{\perp e}$) along the nozzle. The axial coordinate is identified through the normalized local potential (Φ).

3.1.3 Modified Martinez-Sanchez Model

As mentioned the Modified Martinez-Sanchez model has been verified by benchmarking it against the original MS model, checking that under the correct conditions the discrepancy between the models reduces to zero. To this end the MS model has been run with an initial adimensional ion energy of $\epsilon_i = 0.1$, a mass ratio between ions and electrons of $m_{ratio} = 10^3$, a prescribed net current $\tilde{j} = 0$ and an error weight of $K = 20$. On the other hand the MMS algorithm has been run with the same mass ratio, prescribed net current and error weight, but with a normalized kinetic energy at the nozzle throat of 0.5, corresponding to the sonic velocity condition. The resulting output potential, plasma velocity and density obtained from the two models have been compared in Figure 3.7, where for clarity the MMS data has been represented

with blue circles, while the continuous black line corresponds to the MS outputs. Of course, since the Modified Martinez-Sanchez model is limited to the description of a simply divergent nozzle the results had to first be aligned. In all panels, therefore, the potential computed by the full MS model at the magnetic throat has been used to shift the potential distribution found through the modified algorithm, which by assumption would otherwise force the potential to zero at the throat. Likewise the densities displayed in panel (b) have been normalized by the plasma density at the throat, reason for which the MS model computes a normalized density of roughly 2 at the reservoir, instead of 1 as would be expected. By observing Figure 3.7 a nearly perfect agreement can be appreciated between the potential and plasma density (panels (a) and (b)) predicted by the two models. A slight discrepancy, especially in the further regions of the nozzle may instead be noted in the velocity (panel (c)).

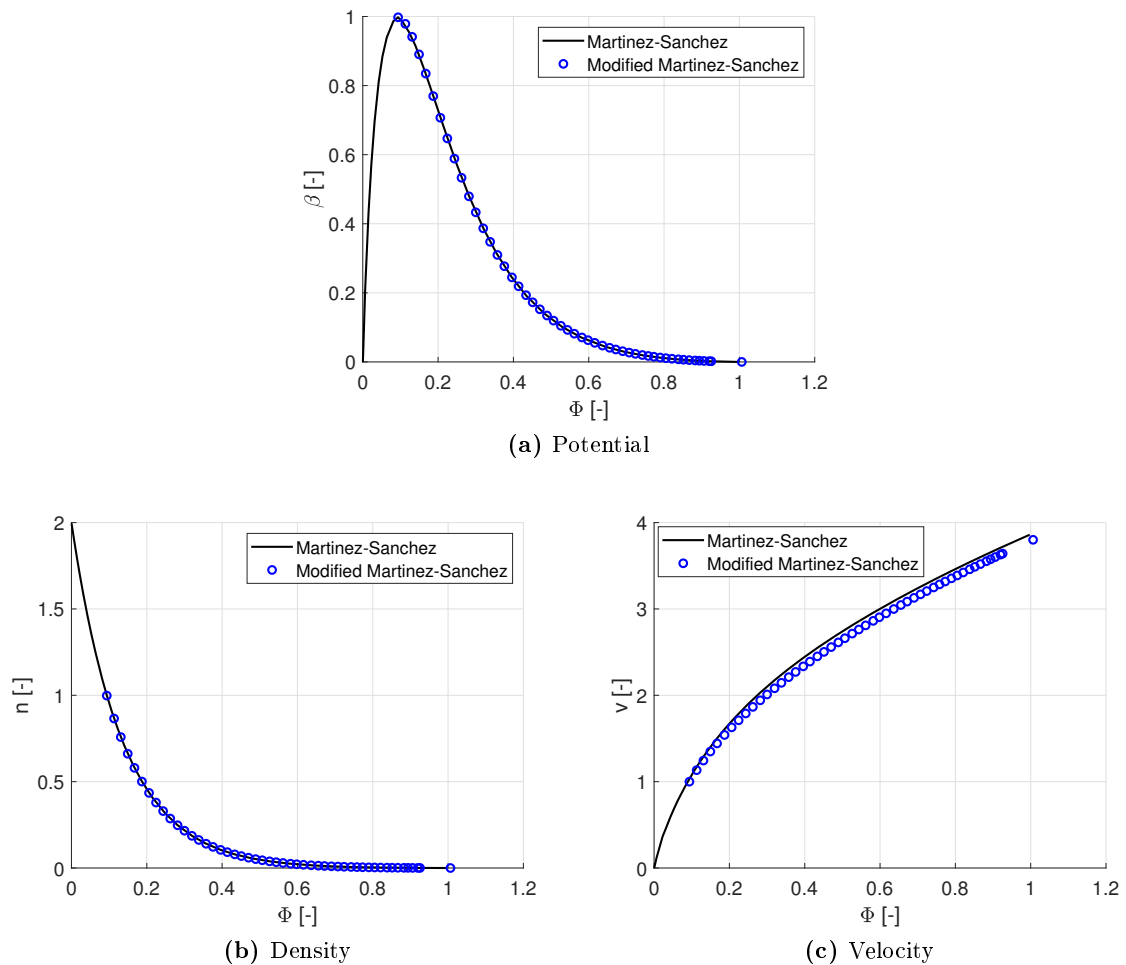


Figure 3.7: Comparison between the outputs of the Modified Martinez-Sanchez (blue open circles) and the Martinez-Sanchez models (continuous black line). The normalized density (n), velocity (v) and magnetic field (β) are plotted against the normalized potential (Φ), used to identify the axial position along the nozzle.

The difference found in the velocity computed by the two models may be attributed to the thermal energy that the ions still maintain at the magnetic throat. While at the throat this energy is indeed stored under the form of a thermal agitation, and therefore averages out in the computation of the average axial plasma velocity, as the expansion proceeds it is converted into axial kinetic energy through the conservation of the first adiabatic invariant. The final velocity computed by the MS model, that takes into consideration this energy source, results therefore higher than the one computed by the Modified Martinez-Sanchez model, that neglects the ion

thermal energy. This interpretation may be verified by running the MMS model with an initial ion kinetic energy equal to the ion energy found by the MS model at the nozzle throat. As shown in Figure 3.8 this approach leads to an overestimation by the MMS model of the axial velocity at the throat, where it considers the ion thermal energy already converted into the axial kinetic energy, but a precise alignment of the results at the end of the expansion, where both models now consider the full ion energy to be directed axially. This analysis implies that, as expected, for a simply divergent geometry the Modified Martinez-Sanchez model is capable of accurately substituting the full MS model for low initial ion thermal energies. For higher ion energies, however, especially in the further regions of the expansion, the model is prone to the underestimation of the plasma velocity. In the case of the cathodeless thrusters considered most of the energy transferred to the plasma is stored into the electron population, meaning that the adimensional initial ion energy is sufficiently low to permit an accurate use of the MMS model. For the typical values of adimensional initial ion energies between $\epsilon_i = 0.01$ and $\epsilon_i = 0.001$, in fact, the maximum relative deviation found at the end of the expansion, where the results of the two models show the biggest discrepancies, did not exceed 5%.

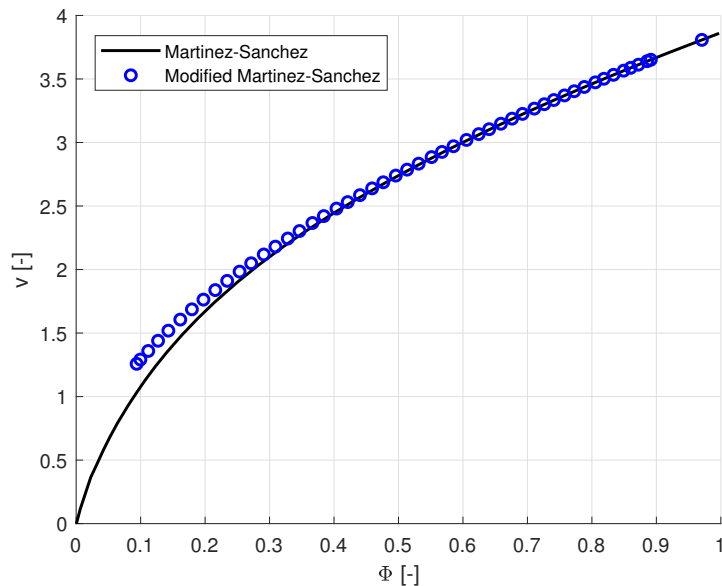


Figure 3.8: Comparison between the velocities computed by the MS and MMS models. The normalized plasma velocity (v) along the nozzle computed by the MS model (black line) and the solution obtained from the MMS model (blue line) in function of the normalized potential (Φ).

3.1.4 Global Source Model

As mentioned no direct verification is available for the Global source model, which has been autonomously developed. Some of the main hypotheses and modelling choices made may however be compared with experimental data in order to verify their accuracy. Amongst these one of the most delicate and complex physical phenomena to model is the ion and electron diffusion towards the radial walls and the consequent ratio between the plasma density on the source axis and the one found at the outer walls (h_R). The determination of this quantity in fact requires the correct modelling of both the plasma reactions, necessary to compute the particles' collision frequencies, and its dynamics, fundamental in the description of the cross-field diffusion. The h_R coefficient, as explained in Section 2.2.2, may be computed analytically by means of the Godyak expressions, starting from the perpendicular diffusion coefficient $D_{tot\perp}$. In the global source model presented this coefficient has been determined by joining heuristically

two diffusion models, as explained, with Equation 2.101, where the coefficient λ_D is taken equal to 0.8 for magnetic inductions below 200 G and to 1 for higher magnetic fields. However other expressions used to determine the perpendicular diffusion coefficient have been proposed in Reference [61], namely the simple ambipolar diffusion (corresponding to Eq. 2.100), the Simon diffusion, the Simon ambipolar diffusion and the Lieberman diffusion (corresponding to Eq. 2.99). The density ratio coefficients h_R obtained through the Godyak expression from these different diffusion coefficients, together with the implemented one, have been computed for different values of magnetic induction and compared with the empirical expression proposed by Lafleur [1] and reported in Eq. 2.67. The results, that have been used to determine the most adequate expression for the perpendicular diffusion coefficient and an empirical value for the coefficient λ_D , have been reported in Figure 3.9, for different values of magnetic induction.

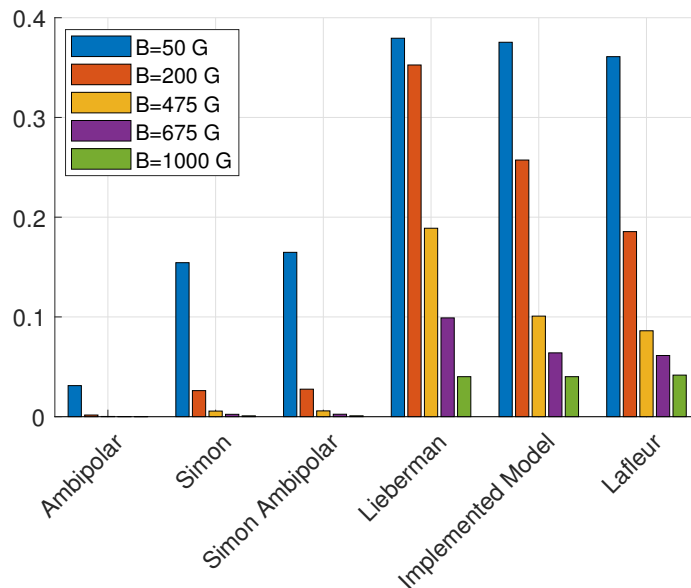


Figure 3.9: Density ratios between the source axis and the outer radial walls (h_R) computed with different perpendicular diffusion coefficients, and for different magnetic inductions. The *Implemented Model* column shows the solutions offered by the heuristic joining of the Ambipolar and Lieberman expressions implemented in the Global source model.

As shown in Figure 3.9 the comparison between the adopted modelling of the radial density ratio h_R and the empirical expression proposed by Lafleur results in quite a good agreement between the two possibilities. On the other hand the ambipolar, Simon and Simon ambipolar expressions proposed for the diffusion coefficient all greatly underestimate the plasma radial diffusion. This can be explained by considering that these expressions assume that both electrons and ions diffuse together towards the radial walls, strongly limiting the diffusion because of the electrons' inferior ability to cross the field lines. The Lieberman expression, instead, considers the radial diffusion of only ions, while the electrons reach the source walls by moving axially along the field lines, and especially for higher magnetic inductions better agrees with the empirical model. To further verify that the model developed is capable of accurately predicting the radial distribution of the plasma the distribution obtained through Equation 2.66 and the computed h_R coefficient has been benchmarked against the experimental data of Reference [62]. To this end the global source model has been run with the source characteristics presented in Table 3.2 and for two values of magnetic induction: $B = 0$ G and $B = 3825$ G. This latter magnetic field intensity is much higher than the typical ones encountered in cathodeless plasma thrusters, and a validation of the radial distribution for lower field intensities would be largely beneficial. No further experimental data of the radial distribution of the density inside the

source for such field values however has been found in the literature. As shown in Figure 3.10 a good agreement has been reached between the Global source model and the experimental data, with maximum relative errors of 10%.

Parameter	Value	Units
Source radius (R_s)	3.2	cm
Source length (L_s)	30	cm
Mass flux (\dot{m})	0.24	mg s^{-1}
Input power (P_T)	600	W
Wave coupling efficiency (η_{rf})	0.85	—

Table 3.2: Source parameters used to validate the computed plasma radial profile.

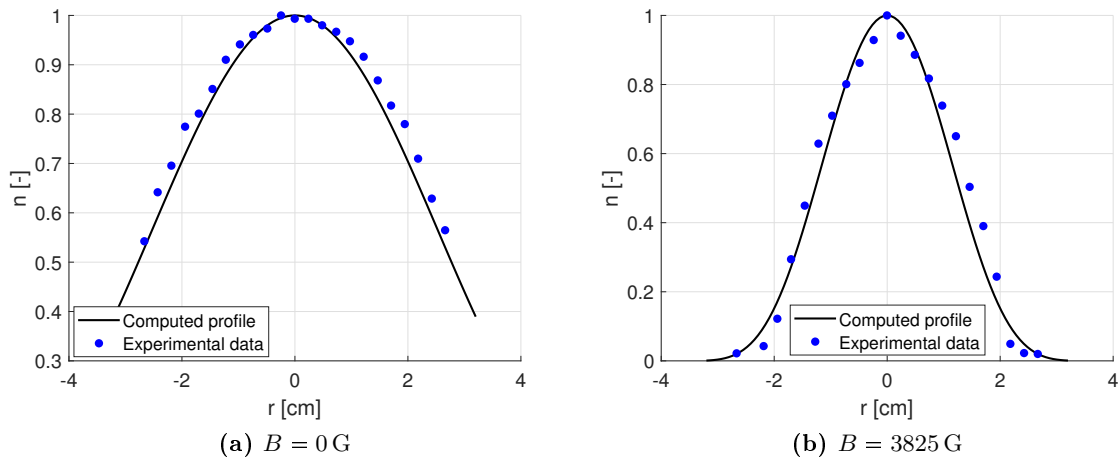


Figure 3.10: Comparison between the computed plasma radial profile (black line) and the experimental data (closed blue circles) from Reference [62].

Finally, the expressions for the ionization and elastic scattering reaction rates (K_{iz} and K_{El}) presented in Table 2.2, have also been compared to other experimental data. Only these reaction rates have been validated because no corresponding experimental data have been found for the other reactions. Most databases, in fact, group excitation and de-excitation reactions in a single coefficient, resulting in reaction rates that are challenging to compare with ones that model these types of collisions separately. Moreover experimental data on the Langevin and Coulomb scattering, along with charge exchange reactions, have not been found in the considered databases. The Lieberman expressions for ionization and elastic scattering reaction rates [3], utilized in the Global source model, have therefore been compared with another set of analytical expressions proposed by Eggarter [63] and with the cross-sections found in the Hayashi [64], Biagi [60] and BSR [65] databases and integrated over a Maxwellian distribution using the *Bolsig+* algorithm [59]. The results, in function of the electron temperature T_e , have been presented in Figure 3.12, where the green line represents the Lieberman analytical expression adopted in the model.

As can be seen in the case of the ionization of Argon from the ground state all of the considered references are in good agreement. The elastic scattering, instead, finds the considered references in slight disagreement. The Lieberman expression, in any case, finds confirmation in the BSR database and in the Eggarter expressions, and has therefore been implemented into the model. It should also be mentioned here that while the Lieberman expressions utilised are formally valid in an electron temperature range between 1 eV and 7 eV it is apparent from Figure 3.12

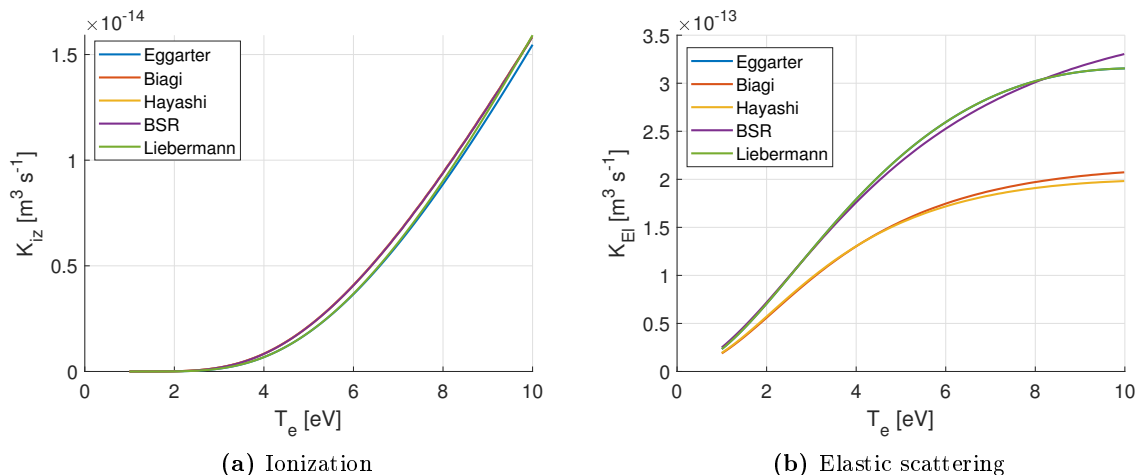


Figure 3.11: Comparison between the different ionization and elastic scattering reaction rates (K_{iz} and K_{El}) obtained from regressions and databases found in the literature in function of the electron temperature T_e . The red, yellow and purple lines represent the values found respectively in the Biagi, Hayashi and BSR databases, while the blue and green lines correspond to analytical fittings proposed by Egarter and Lieberman. This latter expression is the one adopted in the Global source model.

that this validity range may potentially be stretched to higher temperatures.

3.2 Comparison

3.2.1 Source Models

The Global source model and the Lafleur source model have been run with identical input data, summarised in Table 3.3, in order to compare the results obtained through the two algorithms. The assumed thruster characteristics are those of a typical Helicon Plasma Thruster [1]. To better compare the two source models and to make sure that any discrepancy in the results could not be attributed to a different description of the nozzle, the Lafleur MN model has been used to define the boundary conditions at the source exhaust for both models. A simply divergent nozzle, with a magnetic induction at the throat identical to the one found in the plasma source, has been considered, along with Lafleur’s detachment criterion.

Parameter	Value	Units
Source radius (R_s)	3.25	cm
Exhaust radius (R_f)	3.25	cm
Source length (L_s)	12	cm
Mass flux (\dot{m})	0.72	mg s^{-1}
Source magnetic induction (B)	100	G
Total input power (P_T)	600	W
Wave coupling efficiency (η_{rf})	0.85	—

Table 3.3: Thruster parameters used to compare the Global source model and the Lafleur Source model.

The electron temperature and the maximum plasma density computed by the two models can be found in Table 3.4, while the axial profiles of the Mach number and plasma and neutral

densities computed by the Lafleur model are shown in panels (a) and (b) of Figure 3.12. As can be seen from Table 3.4 a strong discrepancy has been found between the models. This difference in results however may not be attributed to a deviation in the way that the plasma losses are computed, as by forcing the same plasma conditions onto the two models the loss terms at the source walls and exhaust result very similar. The cause of the discrepancy between the models is instead to be found in the governing equations adopted. Indeed, as already mentioned in Section 3.12, the disagreement may be attributed to the fact that in the Lafleur source model the collisions are neglected in the momentum equation. This results in an overestimation of the velocity at the exhaust and a consequently high electron temperature (necessary to maintain sonic conditions at the nozzle throat), along with a noticeably low plasma equilibrium density. The high exhaust velocities in fact cause a large number of particles to escape the source, decreasing the density. The results obtained from the Global source model are instead more in line with the expected values. Indeed, thrusters similar to the one modelled have been shown to produce electron temperatures in a range between 3 eV and 6 eV, and plasma densities between $1 \times 10^{18} \text{ m}^{-3}$ and $1 \times 10^{19} \text{ m}^{-3}$ [53].

Model	Maximum plasma density [m^{-3}]	Electron temperature [eV]
Lafleur source model	0.67	13.19
Global source model	1.42	5.93

Table 3.4: Plasma properties predicted by the source models for the thruster characterised in Table 3.3

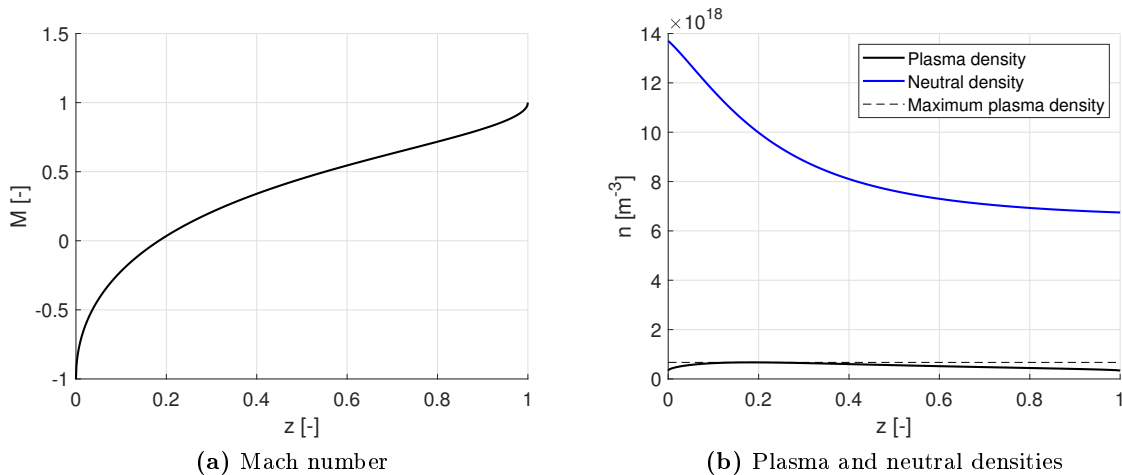


Figure 3.12: Plasma properties predicted by the Lafleur source model for the thruster characterised in Table 3.3. Panel (a) shows the Mach number (M) in function of the normalized axial coordinate (z). In panel (b) the neutral gas density (blue line) and the plasma density (black line) along the source are shown. The dashed black line marks the maximum plasma density.

It should however be mentioned that the Lafleur source model results, in any case, very efficient in the calculation of the propulsive properties of a modelled thruster. Indeed, as shown by Eq. 2.7, the thrust produced can be considered proportional to the product of the plasma density and the electron temperature found inside the source (nT_e). By comparing this quantity computed through the two source models, in Figure 3.13 it is then possible to appreciate their close agreement, especially at lower power and ionization fractions. This leads, in the end, to the computation of similar propulsive properties. Furthermore the Lafleur model does come

with a few advantages, like the possibility of obtaining an axial density and velocity distribution inside the source, as well as the slightly faster computational times. Nevertheless, for the sake of brevity and because of the more accurate physical description of the generated plasma that it offers, only the Global source model will be used to describe the plasma generation stage of cathodeless thrusters in the remaining pages of this thesis.

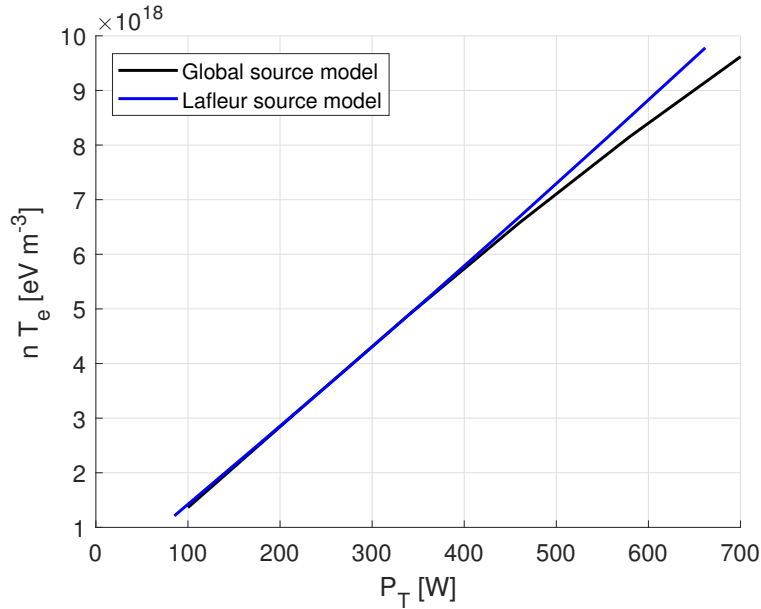


Figure 3.13: Comparison between the product of the plasma density and electron temperature (nT_e) computed by the Global source model (black line) and the Lafleur source model (blue line) in function of the total power provided to the thruster (P_T).

3.2.2 Nozzle Models

Like for the source models, the results obtained from the different nozzle models described in Section 2.1 have been compared. To this end the expansion in a simply convergent nozzle has been modelled using the three proposed algorithms. The nozzle has been considered attached to a reservoir containing a plasma whose characteristics are summarised in Table 3.5, and the zero of the ambipolar potential has been placed at the nozzle throat. For the Lafleur and Modified Martinez-Sanchez algorithms a unitary Mach number has been imposed at the nozzle entrance, while the stagnation quantities have been used for the Martinez-Sanchez model so as to force the plasma properties found in the reservoir in the nozzle throat, albeit the necessary computation of the full convergent-divergent geometry. The plasma potential, density and velocity found by the three models may be seen respectively in panels (a) (b) and (c) of Figure 3.14. Here the density and velocity have been normalized by the plasma density and Bohm velocity found in the reservoir, while the potential has been left dimensional, so as to compare the total potential drop computed by the different models

As can be seen the behaviour of the potential computed by the three models is in very good agreement. The main difference is that for an infinite expansion where the magnetic induction approaches zero the Lafleur model, due to its assumption of electron isothermality, finds an ever-decreasing ambipolar potential, while the other two models, that capture electron cooling, are capable of finding a finite value for this quantity. The effect of this infinite acceleration of the ions considered by the Lafleur model can be seen also in panel (c), where the plasma velocity in the far region of the nozzle continues to increase indefinitely, while the one computed by the other two models finds a maximum finite value. The discrepancy in the velocities computed

Parameter	Value	Units
Plasma density (n)	10^{18}	m^{-3}
Electron temperature (T_e)	4	eV
Ion to electron mass ratio (m_{ratio})	72820	-
Initial ion internal energy (ϵ_i)	0.01	-
Net prescribed current (\tilde{j})	0	-
Throat radius (R_s)	3.25	cm

Table 3.5: Plasma parameters used to run the magnetic nozzle models

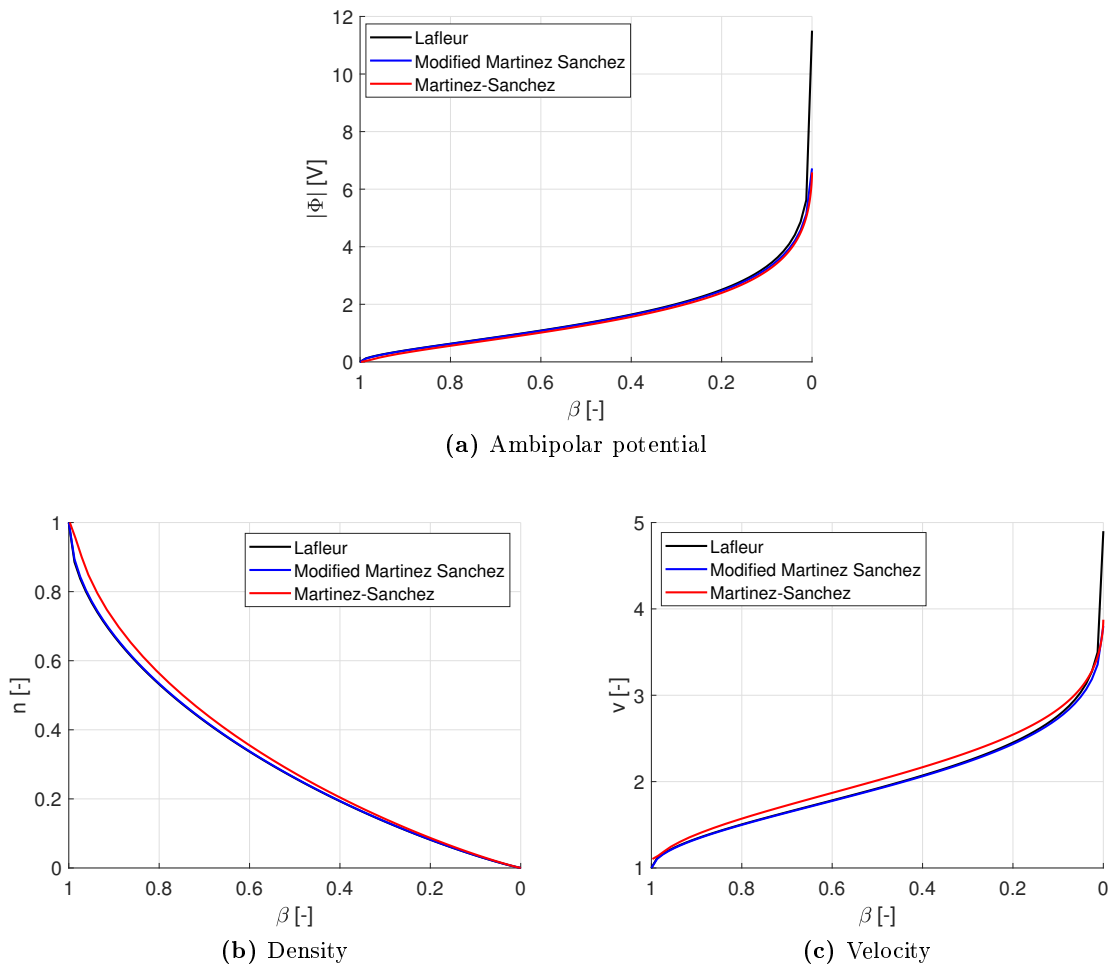


Figure 3.14: Properties of the expanding plasma along the nozzle according to the Laffleur model (black line), the MMS model (blue line) and the MS model (red line). The normalized magnetic induction (β) has been used to identify the position along the diverging nozzle.

by the MS model with respect to the other two algorithms is, instead, due to the throat conditions considered. As shown in Figure 3.3, in fact, the Martinez-Sanchez model finds a slightly supersonic velocity at the magnetic throat, inducing a shift in the velocity values, that remains nearly constant throughout the majority of the expansion. It has been verified, but for brevity the resulting Figure will not be shown here, that by imposing the velocity computed at the magnetic throat by the MS model as the initial condition for the other two models, a very good agreement between the velocity profiles can be reached. Similarly the discrepancies in the density profiles shown in panel (b) may also be explained thanks to the different velocity conditions found at the magnetic throat. To guarantee the flux conservation through the nozzle

in presence of the higher velocities obtained, in fact, the MS model computes a slightly higher density profile throughout the expansion.

The thrust due to the charged particles computed by the three nozzle models may also be compared, in order to shed some light on the effects of a magnetic nozzle and on the results of the implemented algorithms. This thrust may be subdivided in two different ways, as shown in Equations 3.5 and 3.6. In the former case two thrust contributions are highlighted: one deriving from the momentum flux that the plasma particles carry out of the thruster (F_{mom}) and one from the pressure exerted by the plasma's thermal agitation (F_{pres}). In the latter, instead, the thrust is subdivided into the portion of thrust simply obtained by the mechanical forces acting onto the source walls (F_{source}), and the thrust increment due to the presence of the magnetic nozzle (F_{MN}).

$$F_{plasma} = F_{mom} + F_{pres} \quad (3.5)$$

$$F_{plasma} = F_{source} + F_{MN} \quad (3.6)$$

Considering once again a simply diverging nozzle attached to the plasma reservoir described by Table 3.5, the thrust forces shown in Figure 3.15 can be found. Here the thrust values have been linked to a point along the nozzle expansion, identified by the local normalized magnetic induction β , by computing the thrust that would be obtained if the nozzle ended in the considered location and the plasma underwent no further expansion. For each model, the total thrust (F_{plasma}) has been represented with a continuous line, the contribution of the magnetic nozzle effect to the total thrust (F_{MN}) with a dashed line, and the portion of the thrust due to the plasma pressure at the nozzle exhaust (F_{pres}) with a dotted line. This last contribution has not been shown for the Lafleur model, as it is undistinguishable from the portion of thrust due to the particle momentum flux crossing the exhaust section because of the way that the thrust is computed in Equation 2.7.

Once again here the slightly higher total thrust computed by the MS model can be explained through the higher Mach number found at the throat, while the diverging values of total thrust found by the Lafleur model far downstream are a consequence of the isothermal assumption. For this reason the Lafleur model must be linked to a detachment criterion: if the expansion is not truncated somewhere along the nozzle the computed thrust results infinite. This is not a strict necessity for the other two models, that are capable of expanding the plasma to infinity without incurring into unphysical thrust values. It is interesting to note that the magnetic nozzle results responsible for roughly half of the total thrust obtained, and becomes more efficient the further the plasma can be expanded before detachment. A correctly designed magnetic nozzle can therefore be expected to roughly double the propulsive performance of a cathodeless plasma thruster. On the other hand instead the contribution to the total thrust offered by the plasma pressure at the nozzle exhaust decreases, logically, as the expansion proceeds. As can be seen this contribution to the thrust becomes rapidly negligible as one proceeds downstream of the throat and most of the propulsive force is stored into the momentum transported out of the thruster by the plasma particles. This effect can be attributed to the conversion of the internal plasma energy to axial kinetic energy of which the magnetic nozzle is responsible.

Having described the results obtained through the nozzle models some more general considerations on their use and characteristics are mandatory. The most apparent differences between the models are the magnetic geometries that they are capable of modelling and the plasma properties that they can compute. The original Martinez-Sanchez model is in fact the only one capable of handling a convergent-divergent magnetic nozzle, as well as offering

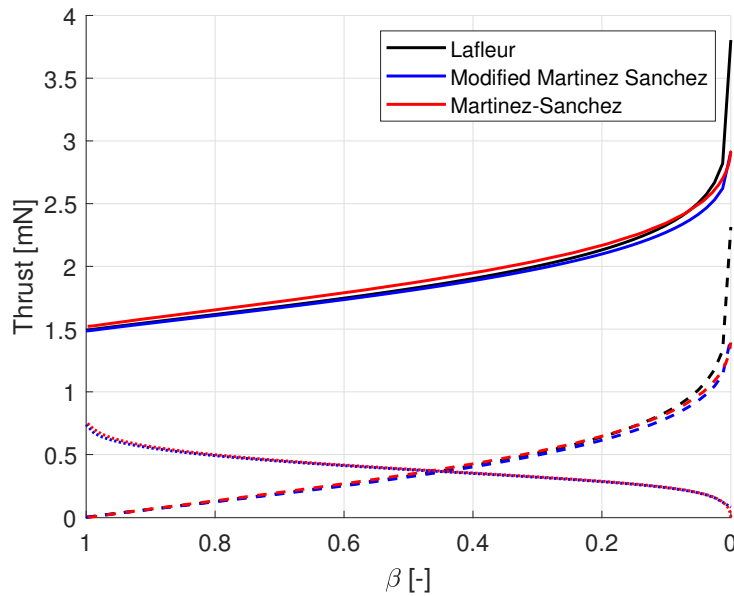


Figure 3.15: Comparison between the plasma thrust forces computed by the Lafleur (black lines), MS (red lines), and MMS (blue lines) models. The the total thrust granted by the plasma (continuous lines), the thrust increment due to the magnetic nozzle (dashed lines), and the contribution to the thrust due to the plasma pressure (dotted lines) are shown in function of the normalized magnetic field (β).

the most detailed description of the plasma characteristics throughout the expansion. It is in fact able to compute both the electron and ion densities, parallel and perpendicular velocities, parallel and perpendicular temperatures, kinetic energies and energy fluxes. The Modified Martinez-Sanchez model and the Lafleur model, instead, are only capable of describing a simply divergent geometry, and while the former is capable of completely characterizing only the electron population the latter only provides the plasma density, velocity and the ambipolar potential, along with the electron temperature, constant by assumption. This lack of information leads to the impossibility of using the Merino and Arefiev detachment criteria with the Lafleur model, and the Merino criterion with the MMS model. On the other hand the Martinez-Sanchez algorithm is computationally quite cumbersome, requiring up to three hours to converge to a self-consistent solution when the nozzle is subdivided into 200 evaluation points. Furthermore it is also numerically unstable, requiring a fine tuning of the weight K , used to compute the error to be minimized, to reach convergence, especially for high values of initial ion energy and mass ratios. These problems are further aggravated if the initial ion energy must be determined through an iterative procedure as described in Section 2.1.2. For the low ion energies typically present in cathodeless plasma thrusters, however, this usually causes negligible variations in the computed results, and can therefore be avoided. The presented drawbacks are strongly mitigated by the normalization carried out on the model outputs, which makes them depend only on the ion to electron mass ratio of the propellant and on the ion energy when its adimensional value is higher than 0.01. Having fixed these values the model outputs may therefore be saved and utilized for any type of plasma conditions upstream of the nozzle, allowing to run the Martinez-Sanchez model only once. The Modified Martinez-Sanchez model also overcomes these drawbacks by slightly simplifying the computations, that allows to reduce the computational cost, and by considering only the divergent part of the nozzle. From the stability point of view, in fact, the most challenging region is the nozzle throat, where the derivative of the magnetic intensity changes sign. By considering only the divergent portion of the nozzle, then, the MMS model greatly improves the stability of the algorithm. In conclusion, considering

the similarity between the obtained solutions, the Laffleur model may be preferred to the other models because of its simplicity and velocity, albeit the mandatory need for a precise detachment criterion. However if more detailed information on the plasma properties are needed, for example for the computation of a detachment criteria, the other two algorithms may result the more adequate alternatives.

The behaviour of the divergence efficiency, computed as explained in Section 2.1.5, should now be considered as it can strongly influence the total thrust offered by the engine. To this end a magnetic nozzle generated by a current ring with a radius three times bigger than the source radius was considered. The divergence efficiency of this nozzle, again computed in function of the normalized magnetic induction β that identifies a precise axial distance from the throat, is reported in panel (a) of Figure 3.16, while its influence on the thrust computed by the three magnetic nozzle models is shown in panel (b).

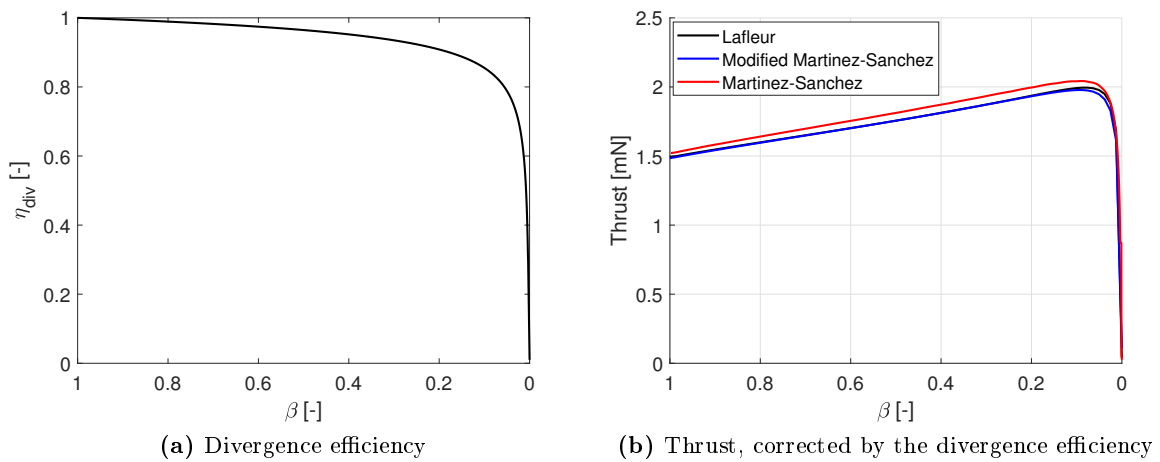


Figure 3.16: The divergence efficiency (η_{div}) and its effect on the thrust. In panel (b) the thrust, corrected with the divergence efficiency, found by the Laffleur, MMS and MS models is represented respectively with the black, blue, and red lines

As can be seen the divergence efficiency decreases as the expansion proceeds downstream and the field lines gradually fan outwards. Indeed, the divergence is unitary at the magnetic throat, where all the field lines are directed axially, and null at infinity, where the field lines have either turned back towards the thruster or are fully directed axially. This efficiency profile implies, as shown by panel (b), that a point along the nozzle exists where the thrust is maximum. Here in fact the plasma has undergone a sufficient expansion, increasing the provided thrust through the magnetic nozzle effect, but is still principally directed axially, granting a good divergence efficiency. By taking this into consideration then the optimal detachment location is not at infinity as would appear from Figure 3.15, but at a precise point along the nozzle that depends on the geometry of the field lines and on the radial density profile found in the plasma.

3.2.3 Detachment Criteria

The effect of the detachment, and of the criteria used to determine its location, becomes therefore of paramount importance. In fact, the detachment location strongly influences the divergence efficiency, especially in the further regions of the nozzle, and in turn the thrust granted by the thruster. Furthermore a precise and effective detachment criteria would allow the use of the simple Laffleur MN model without worrying about the unphysical effects found at infinity, that would be cut out. Indeed, in most cases plasma detachment is likely to occur in a region of the nozzle where the MS, MMS and Laffleur models offer very similar solutions, albeit

with different levels of complexity and computational times. However, as explained in Section 2.1.4, the detachment location is of complex determination, especially when using simple mono-dimensional nozzle models, and is in reality only an idealized concept: the plasma does not detach from the field lines at a given axial coordinate, but over a complex, bidimensional surface. With the intent of further analysing the effects of the detachment location and the differences between the proposed criteria, the simulation of a simply divergent nozzle given by the Martinez-Sanchez model has been truncated using all of the four criteria described. The MS model has been used as it is the only one capable of supporting all of the criteria proposed. The parameters of the Argon plasma reservoir upstream of the nozzle, as well as the properties of the magnetic nozzle considered have been summarised in Table 3.6.

Parameter	Value	Units
Plasma density (n)	10^{18}	m^{-3}
Electron temperature (T_e)	4	eV
Ion to electron mass ratio (m_{ratio})	72820	-
Initial ion internal energy (ϵ_i)	0.01	-
Net prescribed current (\tilde{j})	0	-
Throat radius (R_s)	3.25	cm
Throat magnetic induction (B)	100	G
Current ring radius (R_r)	9.75	cm

Table 3.6: Plasma and magnetic nozzle parameters used to compare the detachment criteria.

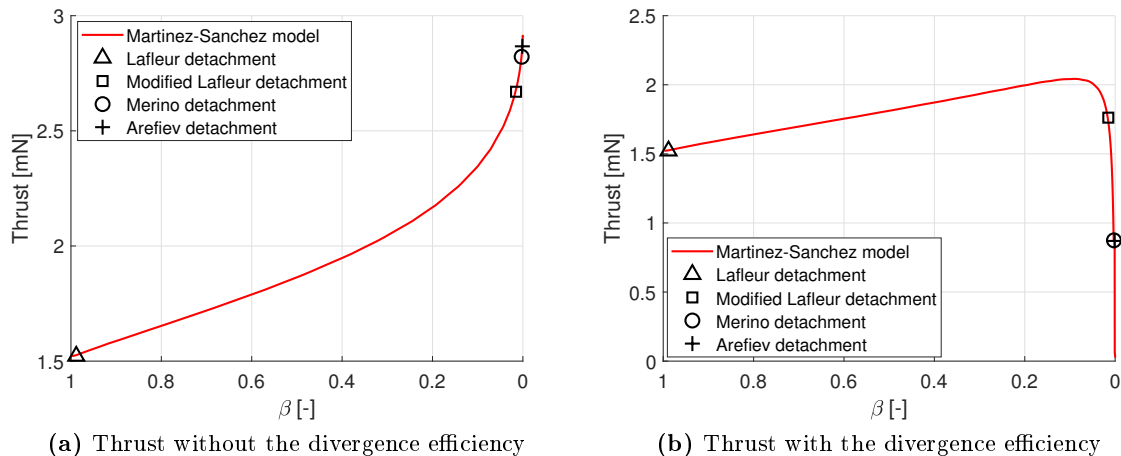


Figure 3.17: Detachment locations found by the four detachment criteria proposed along the magnetic nozzle, and the corresponding thrust. The Lafleur, modified Lafleur, Merino and Arefiev criteria are identified respectively using black open triangles, squares, circles and crosses. The red line represents the total thrust computed by the MS model.

Figure 3.17 presents the results of the simulation, where panel (a) displays the computed thrust corresponding to each detachment criteria without correcting it with the divergence efficiency, while panel (b) also includes the correction for the divergent flow. As can be seen the Lafleur criterion identifies the detachment position at the very start of the expansion. This, as explained in Section 2.1.4, is due to the use of the plasma beam radius as the characteristic length of the magnetic field, and to the relatively low electron temperatures considered, with respect to the ones obtained through the Lafleur source model. Indeed, by changing the definition of the characteristic length in the modified Lafleur criterion the detachment location

moves downstream. On the other hand the Merino and Arefiev criteria identify the detachment location towards the end of the nozzle. This could be expected for the Arefiev criterion as it is not based on the inertial demagnetization of the charged particles, but rather on the stretching of the field lines through the magnetic field induced by their motion. Recent studies, in fact, have shown that this detachment mechanism overestimates the length of the expansion, as it is preceded by the particles' demagnetization [49] [39]. The result given by the Merino detachment instead locates the detachment quite far downstream, but is coherent with the assumptions made: in fact it continues the expansion further than the Lafleur and Modified Lafleur criteria, thanks to the fact that it considers the ambipolar electric field that keeps the ions frozen onto the field lines even beyond their demagnetization. The detachment position found also slightly precedes the one computed through the Arefiev criterion. Finally the influence of the detachment locations found on the divergence efficiency should be analysed. It should be in fact noticed from panel (b) that, as in the case of the Arefiev and Merino criteria, if the detachment is located too far downstream the thrust obtained results inferior to what could be achieved with an earlier detachment. Furthermore, when taking into consideration the divergence efficiency, it becomes apparent that even for the Martinez-Sanchez and MMS nozzle models, where the identification of a detachment location is not strictly necessary to obtain physically meaningful results, the detachment position may strongly influence the computed thrust. The divergence efficiencies corresponding to each detachment criteria have been summarised in Table 3.7. It is interesting to note that only the Modified Lafleur criterion corresponds to a divergence efficiency within the expected range of this parameter for typical cathodeless plasma thrusters: from 60% to 90% [40]. The Lafleur criterion, in fact, considers an excessively premature detachment, while the Merino and Arefiev criteria allow the expansion to proceed too far downstream, where the field lines largely diverge.

Criteria	Divergence efficiency [%]
Lafleur	100%
Modified Lafleur	64.2%
Merino	29.4%
Arefiev	29.3%

Table 3.7: Divergence efficiencies corresponding to each detachment criteria.

Chapter 4

Model Validation against Experiments

In order to understand and demonstrate the accuracy of the implemented models their results have been benchmarked against measurements performed on real cathodeless thrusters. In particular experiments involving (i) a non magnetized thruster (hereafter referred to as Thruster A), (ii) a HPT characterized by a roughly constant magnetic field (Thruster B), and (iii) a HPT whose magnetic geometry is provided of cusps (Thruster C) have been considered, so as to test all of the capabilities of the implemented models. As already mentioned, for the sake of brevity and clarity only the Global source model has been utilised here, as it is preferred to the Lafleur source model because of the higher accuracy with which it captures the physical properties of the generated plasma. On the other hand all of the nozzle models and the Modified Lafleur, Merino and Arefiev detachment criteria have been considered, as well as the total absence of detachment for the MS and MMS models. The Lafleur detachment criterion has not instead been considered, as it identifies detachment at the nozzle throat for both of the thrusters provided of a magnetic nozzle, cutting out the plasma expansion downstream. For each thruster the solutions obtained by considering or not the divergence efficiency have been presented.

4.1 Thruster A

As mentioned the first thruster used to evaluate the accuracy of the models developed consists of a simple plasma source, devoid of a confining magnetic field, developed, tested and described by Takahashi et al. in Reference [55]. While simulating the plasma characteristics and thrust obtained by this thruster may not give any information on the modelling of the magnetic nozzle or on the plasma diffusion in presence of a confining magnetic field, it offers precious information on the description of the plasma reactions inside the source and of the plasma sheath and losses along the source walls. The characteristics of Thruster A are summarized in Table 4.1.

It should here be mentioned that while in the Global source model the plasma diffusion inside the source has been modelled considering the presence of a confining magnetic field, Equation 2.101, used to compute the diffusion coefficient, reverts to the computation of the simple ambipolar coefficient in the case of a null magnetic induction [3] making it capable of also modelling a source with no magnetic fields. This can be appreciated by noticing the good agreement shown between the computed and experimental data in panel (a) of Figure 3.10. However in order to model the considered thruster some changes have been made in the described source model. In particular, in absence of a magnetic nozzle, the plasma exhaust and the computation of the thrust have been slightly reworked. It has in fact been assumed that an ideal stationary plasma sheath is found at the exhaust section of the source, so that the plasma density found there corresponds to the maximum density in the source reduced by a factor h_L ,

Parameter	Value	Unit
Power range (P_T)	100-700	W
Mass flux (\dot{m})	0.9	mg s ⁻¹
Source length (L_s)	17.5	cm
Source radius (R_s)	3.2	cm
Exhaust radius (R_f)	3.2	cm
Magnetic induction (B)	0	G
Wave coupling efficiency (η_{rf})	1	-
Physical expansion ratio (ε_{exp})	1	-

Table 4.1: Characteristics of thruster A

while the Bohm criterion may be imposed on the velocity of the particles exiting the source. The plasma flux and energy losses can therefore be computed exactly in the same way as the losses at the back wall, with the sole difference that the charged particles do not neutralize, but leave the domain. The portion of thrust due to the plasma particles may instead be computed using the classical thrust equation substituting the mass flux, exit velocity and electron pressure with the adequate terms, yielding an expression identical to Eq. 2.43. Obviously, in absence of a magnetic nozzle, no detachment or divergence have been considered.

By using the parameters summarised in Table 4.1 to run the source model for different values of total power provided to the thruster, the electron temperatures and plasma densities presented with a continuous black line in Figure 4.1 have been computed. The predicted values have been compared with the experimental data reported in Figure 2 of Reference [55], expressed by means of full black circles. Unfortunately the uncertainties regarding these measurements have not been found, and they have therefore been assumed as ideal data. As shown by panel (a) the computed electron temperature agrees well with the experimental data, suggesting that the energy losses and the energetic behaviour of the electron population has been accurately modelled. On the other hand, as shown in panel (b), the computed maximum plasma density appears to qualitatively follow the experimentally determined behaviour, but quantitatively underestimates the real density values found in the source, with a maximum relative error of 43%. A possible explanation for this discrepancy lies in the hypotheses made specifically for the case of a null magnetic field. In fact, the assumption of an ideal plasma sheath and of a sonic velocity at the source exhaust may not accurately model the source exhaust conditions. Indeed, in presence of an open boundary, instead of a solid wall, the Bohm criterion and the plasma sheath model do not necessarily apply.

The thrust provided by the charged particles of the plasma thus characterised, however, has been found to be very faithful to the empirical data, as shown in Figure 4.2 by the continuous black line (the computed plasma thrust) and the circular markers and error bars (the empirical data-points and their relative errors). This result is surprising as, given the low plasma density found by the model, an underestimation of the provided total thrust would have been expected. This discrepancy between the expected behaviour of the thrust and the real measured profile may be attributed either to uncertainties in the experimental data-points, or, once again, to the hypotheses made in the description of the source exhaust. It is important to note that in Figure 4.2 the continuous black line represents the thrust only due to the charged particles. The thrust stand used to obtain the experimental data in Reference [55] has in fact been attached only to the source walls of the thruster and not to the neutral propellant inlet, measuring therefore only the portion of thrust due to the charged particles. The dotted line in Fig. 4.2 however represents the thrust provided by the neutral species that compose the plasma. As can be seen at higher powers, even in absence of the accelerating effect of the magnetic nozzle, this contribution to the thrust is small compared to the one due to the charged particles because

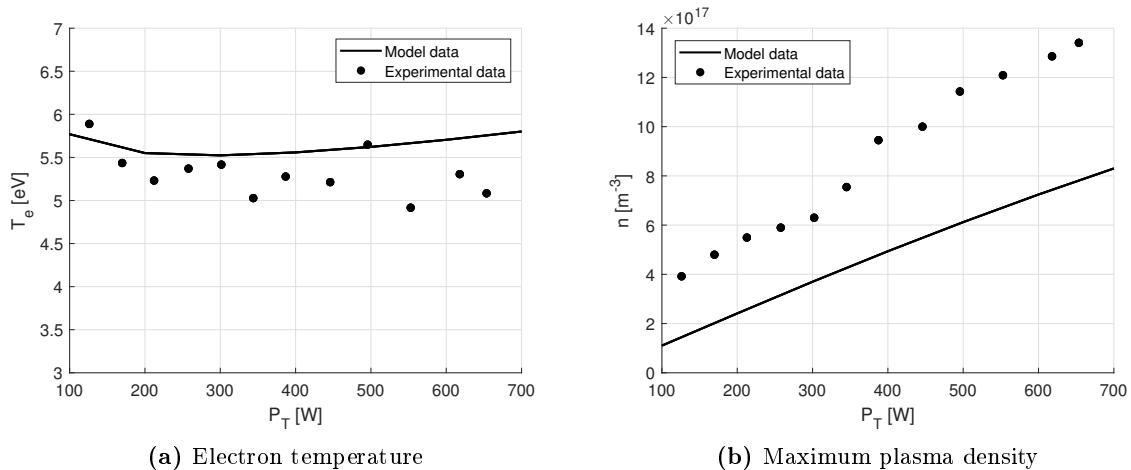


Figure 4.1: Comparison between the computed (continuous line) and measured (closed circles) plasma properties inside the plasma source of Thruster A.

of the much inferior temperature of the neutrals with respect to the electrons. The decrease of this thrust component with higher input powers can be attributed to the rising of the ionization coefficient and the consequently lower neutral density found in the source.

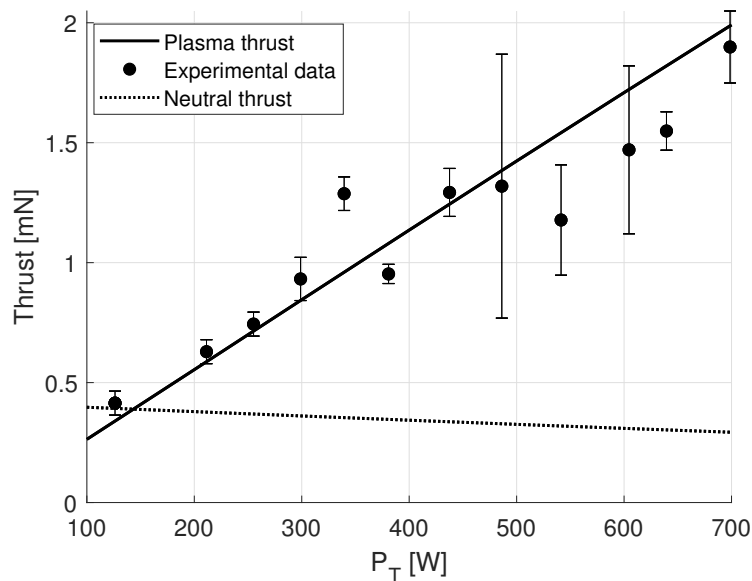


Figure 4.2: Comparison between the computed (continuous line) and measured (closed circles and error bands) total thrust provided by Thruster A.

Finally, for completeness, the specific impulse (I_{sp}) and the thrust efficiency (η_{th}) of the considered thruster have been computed and are reported in Figure 4.3. Both of these values result very low because of the absence of a magnetic field. While the diverging field lines that form the magnetic nozzle, in fact, would accelerate the particles axially, increasing the specific impulse, a confining magnetic field in the source would prevent high energy losses at the source walls, allowing for a larger thrust efficiency. Furthermore, the initial drop in the thrust efficiency can be explained by considering the corresponding decrease in electron temperature shown in panel (a) of Fig. 4.1.

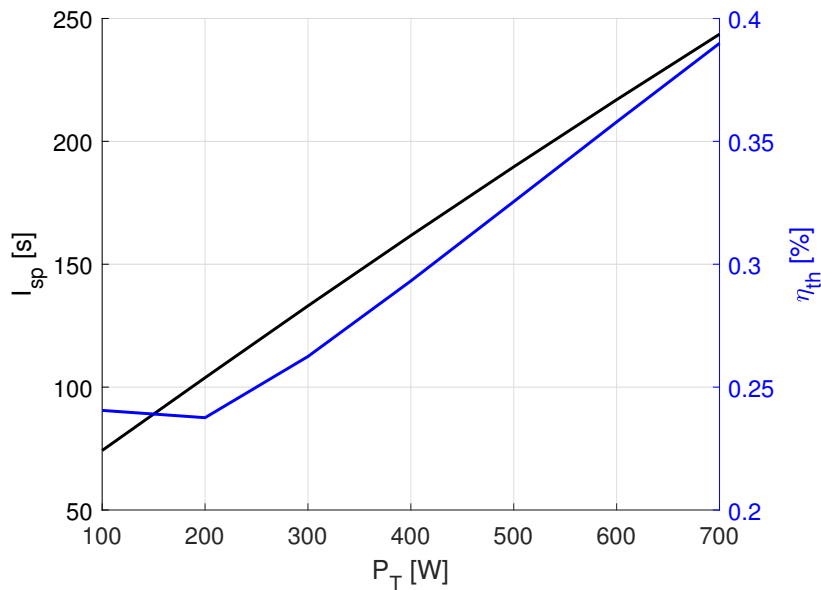


Figure 4.3: Specific impulse (I_{sp}), in black, and thrust efficiency (η_{th}), in blue, of Thruster A.

4.2 Thruster B

The second thruster considered has been chosen because of the uniform and roughly axial magnetic topology that characterises it, which is well suited to the Global source model’s capabilities and assumptions. The thruster has been developed and tested by Takahashi et al. in Reference [53], and is fully characterised by the properties summarised in Table 4.2.

Parameter	Value	Unit
Power range (P_T)	100-700	W
Mass flux (\dot{m})	0.745	mg s^{-1}
Source length (L_s)	8	cm
Source radius (R_s)	3.25	cm
Exhaust radius (R_f)	3.25	cm
Magnetic field in source (B_s)	196.6	G
Magnetic field in throat (B_{th})	204	G
Wave coupling efficiency (η_{rf})	1	-
Radius of current ring (R_r)	9.7	cm
Physical expansion ratio (ε_{exp})	1	-

Table 4.2: Characteristics of Thruster B

Where the magnetic field inside the source has been computed by averaging out the more complex profile described in Reference [53], while the radius of the ring current (R_r) used to produce the magnetic nozzle has been found so as to match the real magnetic geometry of the nozzle, as shown in Figure 4.4.

By running the Global source model, paired with the different magnetic nozzle models to determine the exhaust conditions, the plasma densities and electron temperatures presented by the continuous lines in Figure 4.5 have been obtained for Thruster B. Here the continuous red line shows the results obtained by considering a full expansion through the convergent-divergent nozzle modelled by the MS algorithm (hereafter denoted as the full MS model),

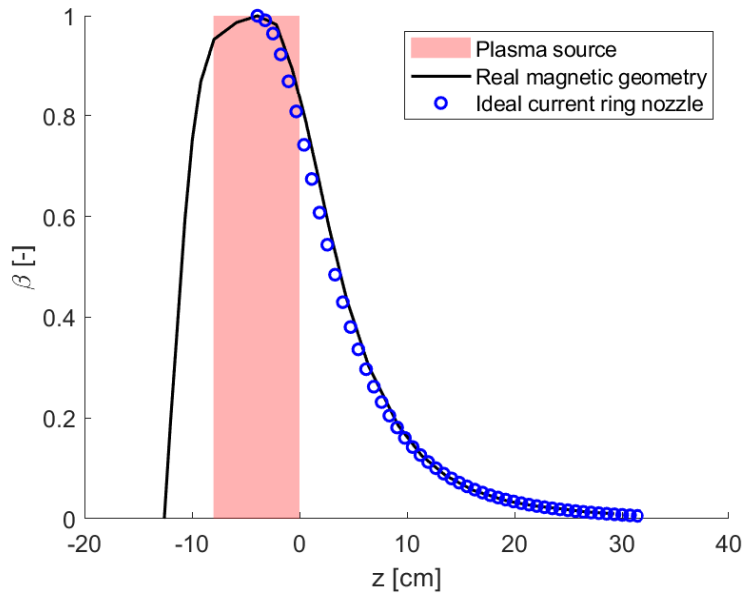


Figure 4.4: Normalized magnetic induction (β) along the axis of Thruster B (black line) compared with the ideal magnetic nozzle obtained from a single current ring of radius R_r (blue open circles). The axial coordinates corresponding to the plasma source have been highlighted in red.

while for the orange line stagnation temperatures and densities have been used to start the expansion in the point of the convergent where the magnetic field matches the one found in the source (partial MS model). The blue and black lines represent respectively the results obtained by adopting the MMS and Lafleur models. Unfortunately the only empirical data available on the plasma source are the electron temperature and plasma density relative to an input power of 600 W, which have been represented with a black circle in both panels. The results show a good quantitative agreement with the experimental data available when considering the simplicity of the model adopted. It should be noted that the lower densities obtained by the two Martinez-Sanchez models with respect to the others may be explained by considering the higher throat velocity imposed by this algorithm. In turn this causes a slightly higher electron temperature, as the provided power is distributed over a smaller electron population.

Once again the available empirical thrust data for Thruster B regards only the force due to the charged plasma particles. The comparison between the results obtained through the presented magnetic nozzle models and detachment criteria, and the data-points taken from Figure 3 of Ref. [53] are shown in Figure 4.6, where no divergence efficiency has been considered, and 4.7, where instead the divergence efficiency has been taken into account. The detachment criteria have been utilized in unison with the nozzle models capable of supporting them: the modified Lafleur criterion has been implemented for all of the MN models, the Merino criterion only for the full and partial MS models, and the Arefiev criterion for the two MS models and the MMS algorithm. The Lafleur criterion has been implemented in its modified version otherwise detachment would occur immediately at the thruster outlet. Of course the Lafleur nozzle model has not been considered for the case of no detachment, as it would compute an infinite thrust, and the divergence efficiency has not been applied to this case, as at infinity a null efficiency and zero thrust would have been found. Finally, for completeness, the portion of thrust obtained from the neutral particles has been plotted as a dotted black line. As can be appreciated by Figures 4.6 and 4.7 in presence of a magnetic nozzle the neutral forces are a small portion of the total thrust provided by the engine.

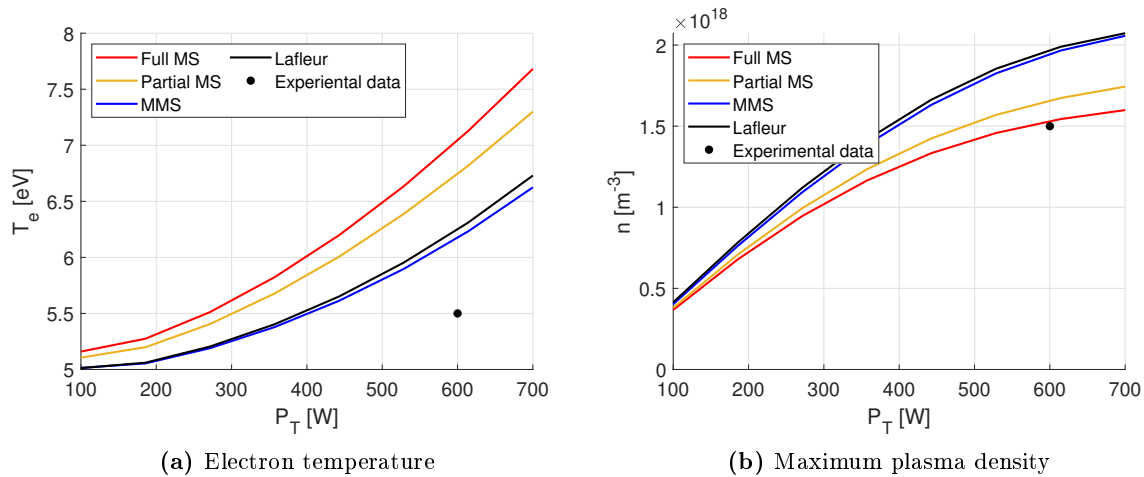


Figure 4.5: Comparison between the computed and measured plasma properties inside the plasma source of Thruster B. The plasma density (n) and electron temperature (T_e) found by using the full expansion in the MS model (red line), the partial expansion in the MS model (orange line), the MMS model (blue line), and the Lafleur model (black line) are plotted in function of the input power (P_T). The black full circles represent the available empirical data.

As can be seen all of the results obtained qualitatively follow the experimental data. From a quantitative viewpoint, instead, the most accurate results have been found by considering the Merino detachment criterion coupled with the divergence efficiency. This solution, however, is characterised by a divergence efficiency largely outside the expected values of 60% to 90% as can be noticed by comparing panel (c) of Fig. 4.6 and panel (b) of Fig. 4.7. A similar issue characterises the solution obtained by the Arefev criterion coupled with the divergence efficiency. The modified Lafleur detachment criterion, coupled with the detachment efficiency, may therefore be considered the solution that best describes the physical behaviour of the thruster, especially when considering the overestimation of the electron temperature shown in Figure 4.5 which means that a slight enlargement of the predicted thrust is to be expected. Regarding the different nozzle models, as expected from their comparison in Section 3.2, the results obtained are quite similar and show a stronger dependence on the detachment and divergence rather than on the choice of the model. Moreover the main differences may be attributed more to the plasma conditions found in the source by each model rather than to the differences in the thrust computation. A few considerations may however be made. The lower values of thrust computed by the MMS model can be associated to the unitary Mach number that it imposes in the nozzle throat, rather than the supersonic velocity considered by the two MS models. Moreover the lower propulsive properties computed by the partial Martinez-Sanchez expansion with respect to the full one can be attributed to the way in which the density at the start of the expansion is calculated, which yields slightly lower values. This difference between the models is also responsible for the higher density found inside the source through a partial expansion.

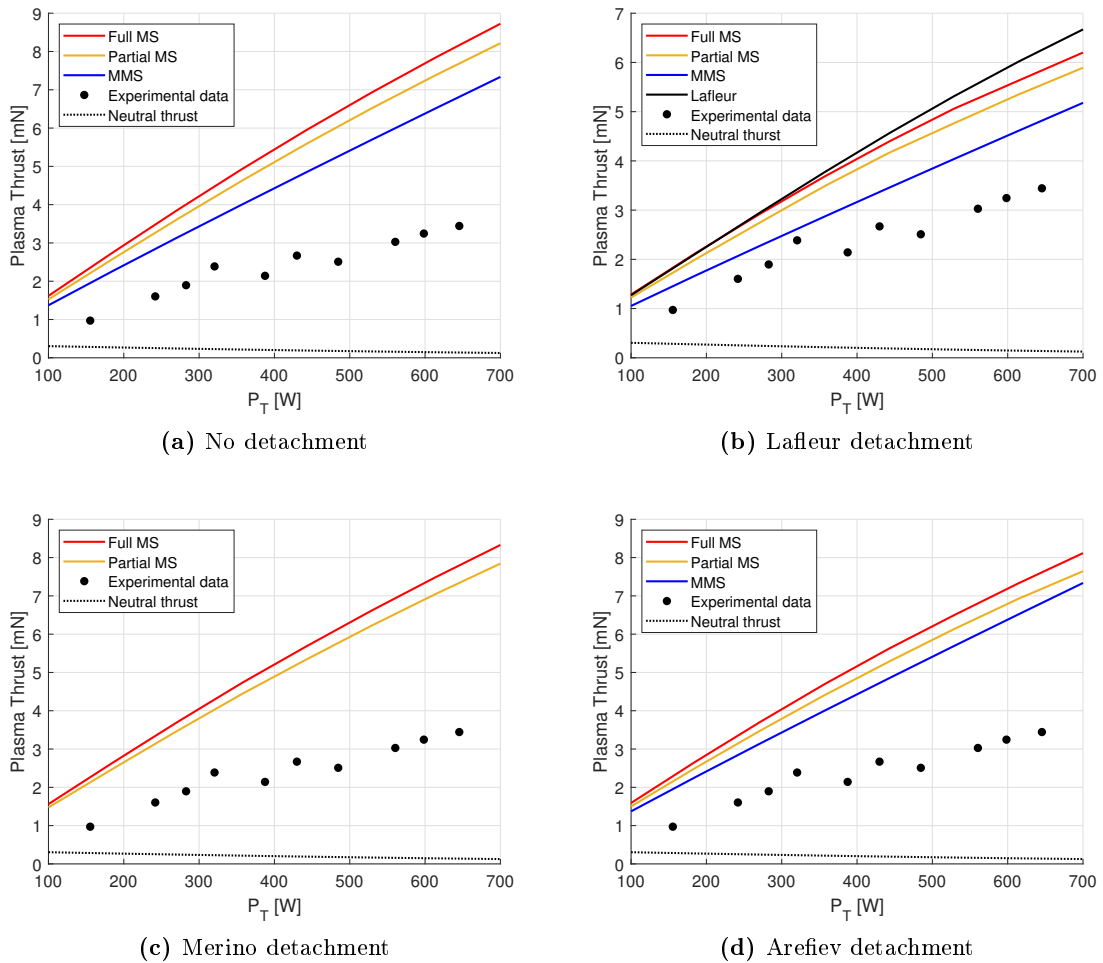


Figure 4.6: The plasma thrust computed with the full MS (red line), partial MS (orange line), MMS (blue line) and Lafleur (continuous black line) models, without divergence efficiency, compared to the experimental data (closed black circles) for thruster B. The black dotted line shows the portion of thrust due to neutral particles.

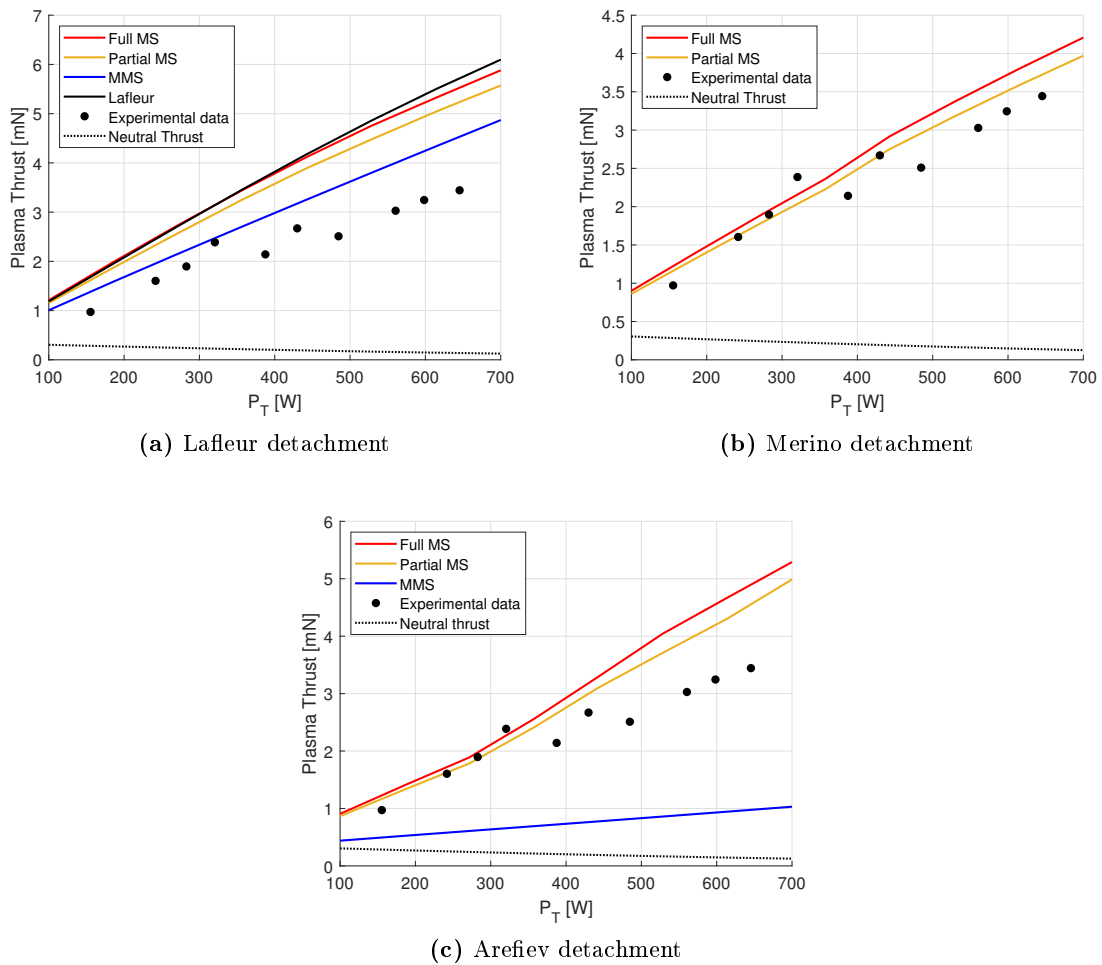


Figure 4.7: The plasma thrust computed with the full MS (red line), partial MS (orange line), MMS (blue line) and Laffleur (continuous black line) models and corrected with the divergence efficiency compared to the experimental data (closed black circles) for thruster B. The black dotted line shows the portion of thrust due to neutral particles.

Finally, as for Thruster A, the specific impulse and thrust efficiency of Thruster B have been computed, and are shown in Figure 4.8. For this computation the partial MS nozzle model, along with the Merino detachment and divergence efficiency have been used, as they guarantee the most accurate numerical prediction of the propulsive force. As can be seen by comparing Figure 4.8 and 4.3 both the specific impulse and the thrust efficiency greatly benefit from the presence of a confining magnetic field and magnetic nozzle. The specific impulse obtained for Thruster Bis in line with the expected values for a Helicon Plasma Thruster, while the low thrust efficiency found is a typical challenge for this technology, and can be expected especially in unoptimized thrusters that make use of argon as the propellant.

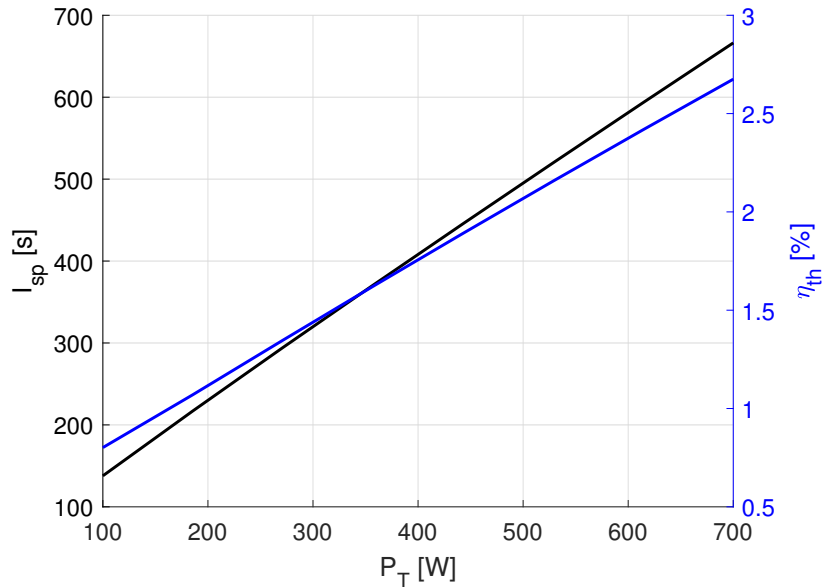


Figure 4.8: Specific impulse (I_{sp}), in black, and thrust efficiency (η_{th}), in blue, of Thruster B

4.3 Thruster C

The last thruster used to compare the the results obtained from the presented models is the one described and tested in Reference [66] by Magarotto et al. The data on this thruster is both empirical, in the case of the propulsive properties, and taken from a higher fidelity numerical model in the case of the plasma properties in the source. This particular thruster has been chosen because of its magnetic geometry, formed by two magnet rings that form cusps in the axially directed field lines. It is therefore a perfect benchmark for the Global source model's description of similar magnetic geometries. The characteristics of Thruster C have been summarised in Table 4.3. It should be mentioned that in Reference [66] the performance of the considered thruster has been determined for four different mass fluxes. These different conditions have all been compared to the solutions obtained from the developed models but, because of the likelihood of the results found, only the case characterised by a mass flux of 0.10 mg s^{-1} has been presented. Finally it is important to note that, in accordance with the model implemented in the Reference, the temperatures assumed for the ion and neutral species have been both changed to 600 K.

In order to model Thruster C a slight change in the Global source model has been made. Indeed, as shown by Figure 8 of Ref. [66], it was found that in this case the maximum plasma density developed in the source is not located at the source's centre, but at the exhaust. Unsurprisingly then, when modelled with the unchanged Global source model, the computed thrust resulted roughly half of the one determined experimentally. The particle and energy

Parameter	Value	Unit
Power range (P_T)	10-70	W
Mass flux (\dot{m})	0.10	mg s^{-1}
Source length (L_s)	8	cm
Source radius (R_s)	0.75	cm
Exhaust radius (R_f)	0.75	cm
Magnetic field in source (B_s)	600	G
Magnetic field in throat (B_{th})	600	G
Number of cusps (n_{cusps})	2	-
Wave coupling efficiency (η_{rf})	1	-
Radius of current ring (R_r)	4.05	cm
Physical expansion ratio (ε_{exp})	30	-

Table 4.3: Characteristics of Thruster C.

transport out of the exhaust have therefore been corrected so as to consider the maximum plasma density at the source's exhaust, neglecting the process of axial diffusion from the centre to the edge of the source. In other words the coefficient h_L used to compute the plasma density at the exhaust has been imposed equal to 1 in Equation 2.113, 2.116 and 2.117, and the stagnation densities used for the Martinez-Sanchez model have been computed starting from the maximum plasma density and not from the reduced value expected at the source exhaust. Likewise the computation of the thrust imparted by the engine has been modified so as to consider the higher density found at the nozzle entrance. The plasma properties computed by the modified Global source model, completed with the different nozzle models considered, are shown in Figure 4.9, along with the results of the higher fidelity fluid model used to characterise Thruster C and equipped of the corresponding error bands. Here the colour coding for the four nozzle models has been kept unvaried, but the line style of the partial Martinez-Sanchez expansion has been changed to dashed, in order to better distinguish the overlapping lines corresponding to the Lafleur, MMS and partial MS models.

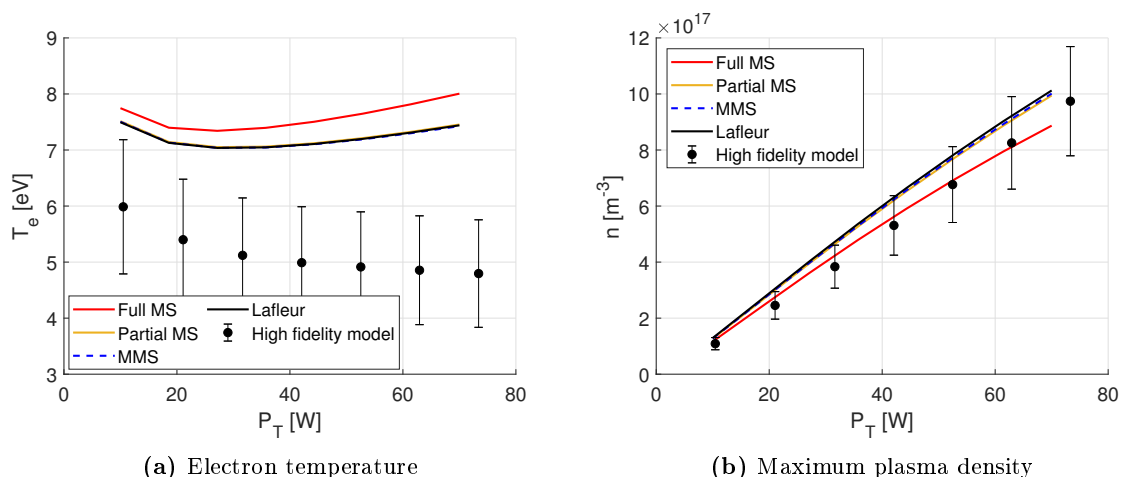


Figure 4.9: The plasma density (n) and electron temperature (T_e) found by using the full expansion in the MS model (red line), the partial expansion in the MS model (orange line), the MMS model (dashed blue line), and the Lafleur model (black line) compared to the results of the higher fidelity fluid model used in Reference [66] (closed black circles and error bands).

As can be seen in panel (b) of Fig. 4.9 an excellent agreement, both qualitative and

quantitative, between the computed density and the reference data has been found for all of the adopted models. It should be noticed that, by imposing the density at the source exhaust, the outputs of all of the models except for the complete Martinez-Sanchez expansion result nearly identical. This is due to the fact that previously the biggest difference between the models corresponded to the way in which the exhaust conditions were computed, which has now been uniformed. Only the full MS expansion differs from the other models because, by determining fictitious stagnation quantities upstream of the convergent, it finds different energy and particle fluxes at the nozzle throat. On the other hand, as already seen in Figures 4.1 and 4.5, the model has the tendency to overestimate the electron temperature. This could be due to many factors, first amongst which the fact that, as shown in Figure 8 of Reference [66], the electron temperature inside the source of Thruster C is far from uniform, while the Global source model adopts this assumption. Other factors that may cause errors in the temperature determination are the complicated coupling between the electromagnetic power and the electron population, the modelling of the plasma collisions and reactions, with particular emphasis on the missing irradiative de-excitation which could constitute an energy sink, and the neutralization at the source walls. In any case the qualitative behaviour of the temperature is closely respected, and considering the simplicity of the model and the error bands of the benchmark data the quantitative predictions obtained may also be considered relatively accurate. It should here be noted that the temperatures that have been obtained are, strictly speaking, outside of the model's working range as they exceed the limit of 7 eV for which the expressions of the reaction rates are valid. Nevertheless, given the good correspondence between the adopted analytical expressions for the reaction rates and other experimental data even over this temperature limit (see Figure 3.12) and the excellent agreement between the model results and the empirical data, the model outputs associated with these high temperature have been considered acceptable, and are here presented.

The thrust derived from the plasma conditions found in Figure 4.9 has been computed and compared with the experimental data of Reference [66]. In this case the total thrust provided by the thruster, including the force due to the neutral particles, has been considered, as the experimental data-points used derive from attaching the full propulsive system to the thrust stand. Once again all of the available combinations of MN models and detachment criteria have been employed, including the absence of detachment, and both the thrust with no divergence correction and the thrust corrected with the divergence efficiency have been presented respectively in Figures 4.10 and 4.11. The same colour scheme identifying the different models has been kept, and as before the portion of thrust due to the neutral particles has been added using a dotted black line. It should be noted that, given the lower powers considered and the consequently lower ionization ratio, the contribution of the neutrals results relevant. Indeed, at an input power of 10 W, it has been found responsible for more than half of the total computed thrust. The higher neutral thrust may also be attributed to the presence of a physical nozzle in Thruster C, which of course exalts the contribution of the unionised gas to the total propulsive performance.

Again from Figures 4.10 and 4.11 it is easy to notice that the results of the Lafleur, Modified Martinez-Sanchez and partial Martinez-Sanchez models result nearly identical. As for the plasma properties of Figure 4.9 this is a consequence of the imposition of the maximum plasma density at the source exhaust, and of the low normalized initial ion energy found for this thruster: $\epsilon_i \approx 0.001$. This low normalized ion energy is due to the high electron temperatures computed (by which the energy has been normalized) and to the relatively low ion temperature assumed in Reference [66]. The main difference between the models has therefore been found in the full Martinez-Sanchez expansion, whose higher computed thrust may be explained by considering the higher throat velocities that this model entails. In any case all of the considered models agree well with the experimental data, especially when considering the 20% relative error that characterises it. As shown in panel (c) of Figure 4.11, the only condition that strongly

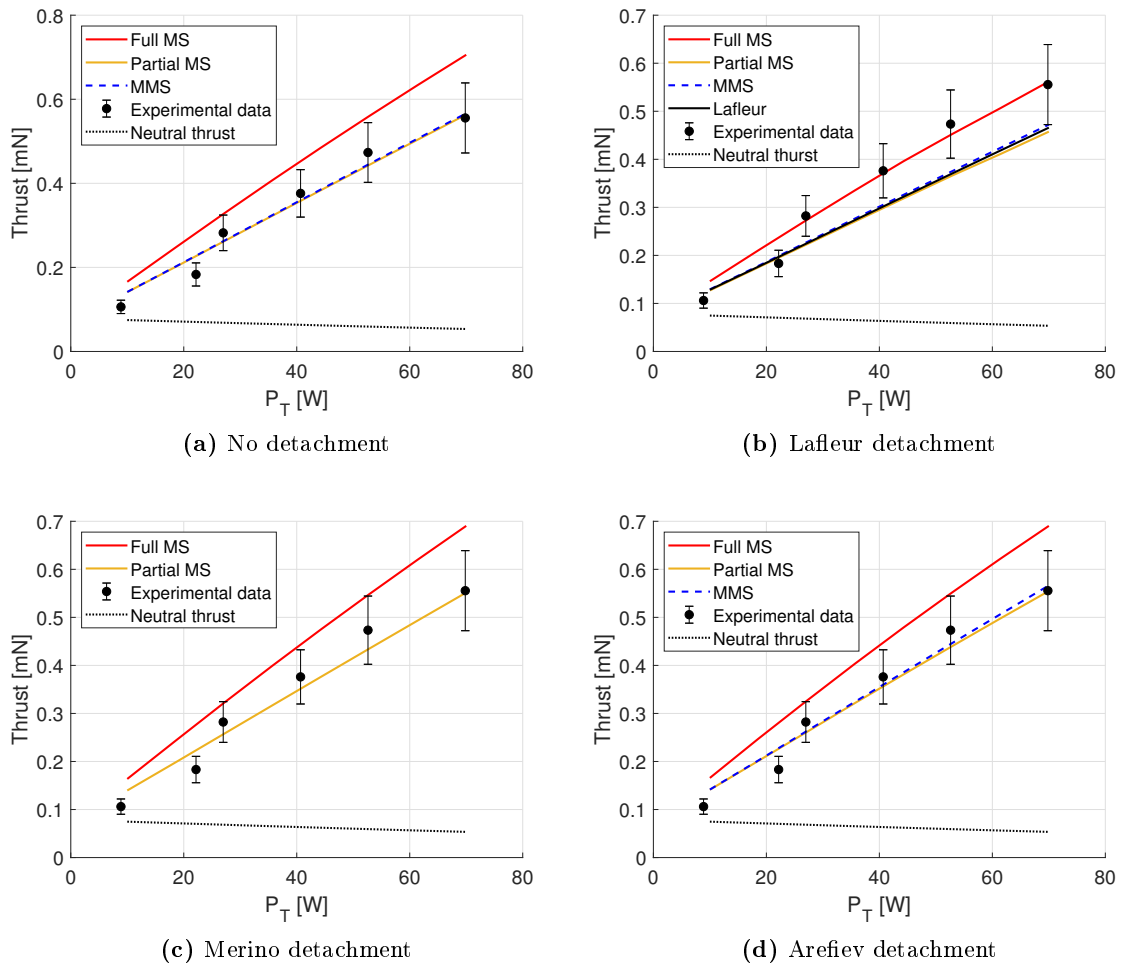


Figure 4.10: The plasma thrust computed with the full MS (red line), partial MS (orange line), MMS (dashed blue line) and Laffleur (continuous black line) models, without divergence efficiency, compared to the experimental data (closed black circles and error bands) for thruster C. The black dotted line shows the portion of thrust due to neutral particles.

underestimates the imparted thrust is the MMS model joined with the Arefiev detachment criterion and the divergence efficiency. Indeed, as for thruster B, this combination identifies the detachment location very far downstream of the nozzle throat, resulting in a divergence efficiency below 10%. Finally, as for thruster B, the most accurate prediction of the thruster’s performance has been obtained by means of the full Martinez-Sanchez nozzle model, coupled with the Merino detachment criterion and the use of the divergence efficiency.

Once again the remaining propulsive properties of Thruster C, for the considered mass flux, have been computed using the MS model, along with the Merino detachment criterion and the divergence efficiency, and are represented in Figure 4.12. As can be seen, especially for the low powers considered, the specific impulse results in line with the expected values for Helicon Plasma Thrusters. On the other hand the thrust efficiency has been found to assume quite low values. However these low thrust efficiencies are a common problem of Helicon Plasma Thrusters, and can be expected especially for unoptimised cases and for thrusters that make us of Argon as a propellant, such as the one considered.

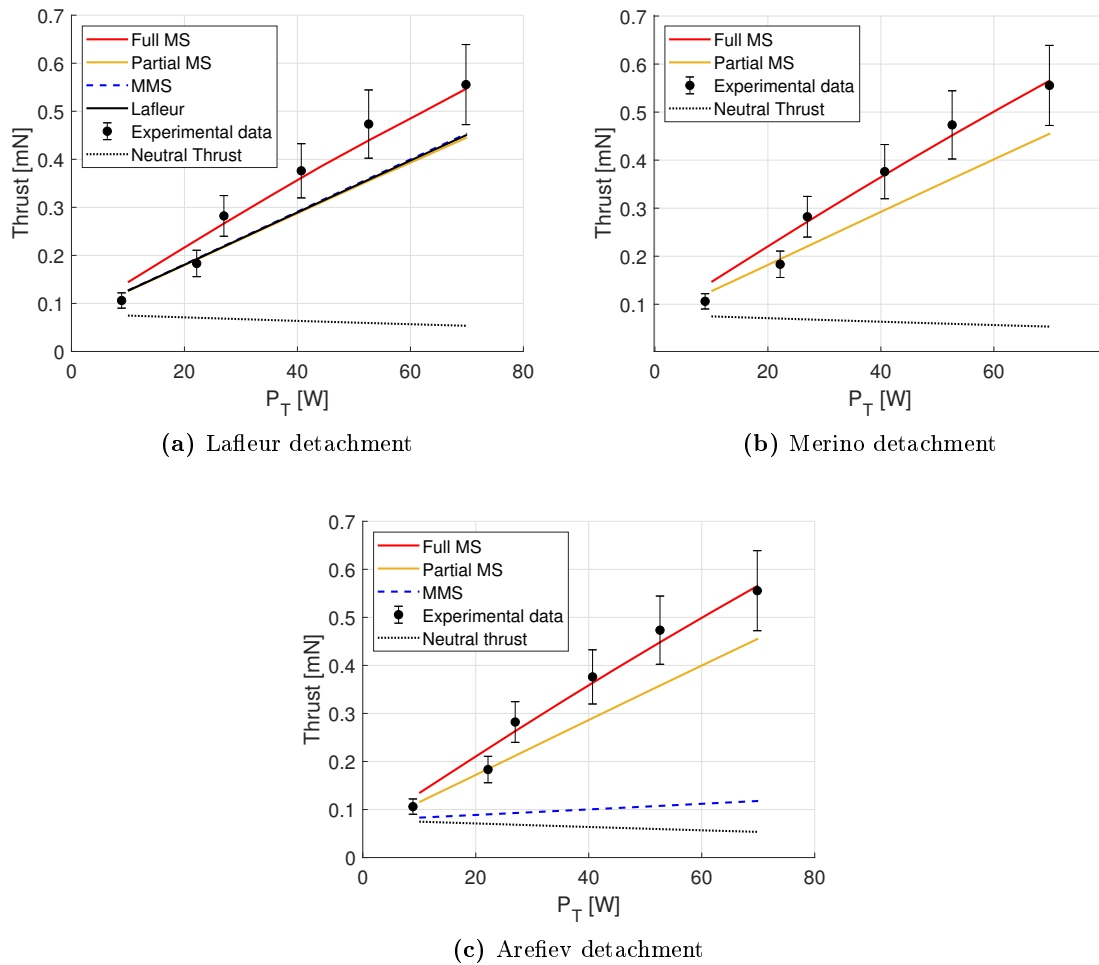


Figure 4.11: The plasma thrust computed with the full MS (red line), partial MS (orange line), MMS (dashed blue line) and Lafleur (continuous black line) models, corrected by the divergence efficiency, compared to the experimental data (closed black circles and error bands) for thruster C. The black dotted line shows the portion of thrust due to neutral particles.

4.4 Validation Results

As shown in the previous Sections the agreement between the numerical models implemented and the experimental data has been found, in general, to be very good, especially considering the simplicity and rapidity of the algorithms adopted. In particular the magnetic nozzle models offer very similar results and the main modelling choice that influences the computed propulsive performances is the selection of the detachment criterion, even more so when the detachment location is used to compute the divergence efficiency. Out of the four detachment criteria presented, however, none have demonstrated a consistent capability of accurately determining the correct detachment location. Indeed, for each thruster considered a different detachment criterion offers the most precise solutions. However, by considering Figure 3.17 and the detachment locations identified by the four criteria, the modified Lafleur criterion may be preferred to the others, as it determines a detachment point more compatible with the expected positions for typical magnetic nozzles. Indeed detachment may be expected at the beginning of the far field of the magnetic nozzle, where the divergence efficiency values are still above 60%.

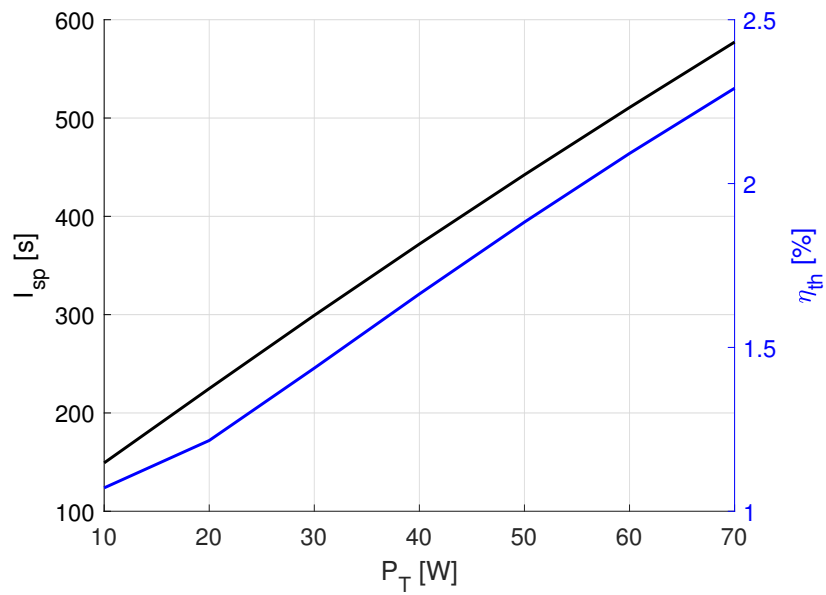


Figure 4.12: Specific impulse (I_{sp}), in black, and thrust efficiency (η_{th}), in blue, of Thruster C.

Chapter 5

Sensitivity to Design Parameters

Having verified the models and ascertained that they accurately describe, at least qualitatively, the behaviour of real cathodeless plasma thrusters, they have been used to determine the sensitivity of the propulsive properties to their main design parameters. The design parameters identified are the source radius (R_s) and length (L_s), the exhaust radius (R_f), the mass flux (\dot{m}), the magnetic induction (B), the number of cusps (n_{cusps}), the total input power (P_T) and the ion and neutral gas temperatures (T_i and T_n). These last two parameters are not actually design parameters, as they are not externally imposed but depend on the characteristics of the thruster. However, since the source model assumes a fixed value for these parameters, the dependence of the results on their values is of interest both in the definition of the model's limits and in the determination of future developments of the codes. In order to characterise the behaviour of the computed electron temperature (T_e), plasma density (n), total thrust (F), specific impulse (I_{sp}) and thrust efficiency (η_{th}) in function of the design parameters a nominal value and an evaluation range has been determined for each of these variables, based on the typical values found in small cathodeless plasma thrusters. Each design parameter has then been varied through its evaluation range while keeping the other parameters at their nominal value, and the behaviour of the mentioned outputs has been computed. The values and ranges associated to each parameter have been summarised in Table 5.1, while the effects of each design variable has been described in the following paragraphs. This sensitivity analysis has been carried out using the Global source model coupled with the partial MS nozzle expansion in a simply divergent nozzle. Following the considerations made in Section 4.4 the modified Lafleur detachment criterion and the divergence efficiency correction have also been employed, as this has been considered the most accurate description available of the detachment. For reference, the plasma properties and propulsive characteristics obtained in nominal conditions have been reported in Table 5.2.

Parameter	Nominal value	Evaluation range	Units
Source radius (R_s)	3	2 - 4	cm
Source length (L_s)	12	5 - 20	cm
Exhaust radius (R_f)	2	2 - 3	cm
Mass flux (\dot{m})	0.3	0.15 - 0.7	mg s ⁻¹
Magnetic induction (B)	300	100 - 600	G
Number of cusps (n_{cusps})	0	0 - 4	-
Input power (P_T)	300	10 - 600	W
Ion temperature (T_i)	0.15	0.1 - 0.2	eV
Neutral temperature (T_n)	300	300 - 600	K

Table 5.1: Nominal value and evaluation range of the design parameters.

Parameter	Value	Units
Plasma density (n)	$1.37 \cdot 10^{18}$	m^{-3}
Electron temperature (T_e)	5.03	eV
Thrust (F)	1.19	mN
Specific impulse (I_{sp})	406	s
Propulsive efficiency (η_{th})	0.79	%

Table 5.2: Plasma characteristics and propulsive properties of the modelled thruster in nominal conditions.

Source Radius

The source radius' nominal value has been fixed at $R_s = 3 \text{ cm}$, while its effects have been evaluated over a range of values going from 2 cm to 4 cm. To guarantee independence between the effects of the design parameters during the variation of the source radius the exhaust radius has been kept constant. Of course this acts as a lower bound to the value of the source radius, which cannot be smaller than that of the exhaust. The effects of the variation of R_s on the plasma properties inside the source and on the propulsive characteristics of the thruster are shown in Figure 5.1.

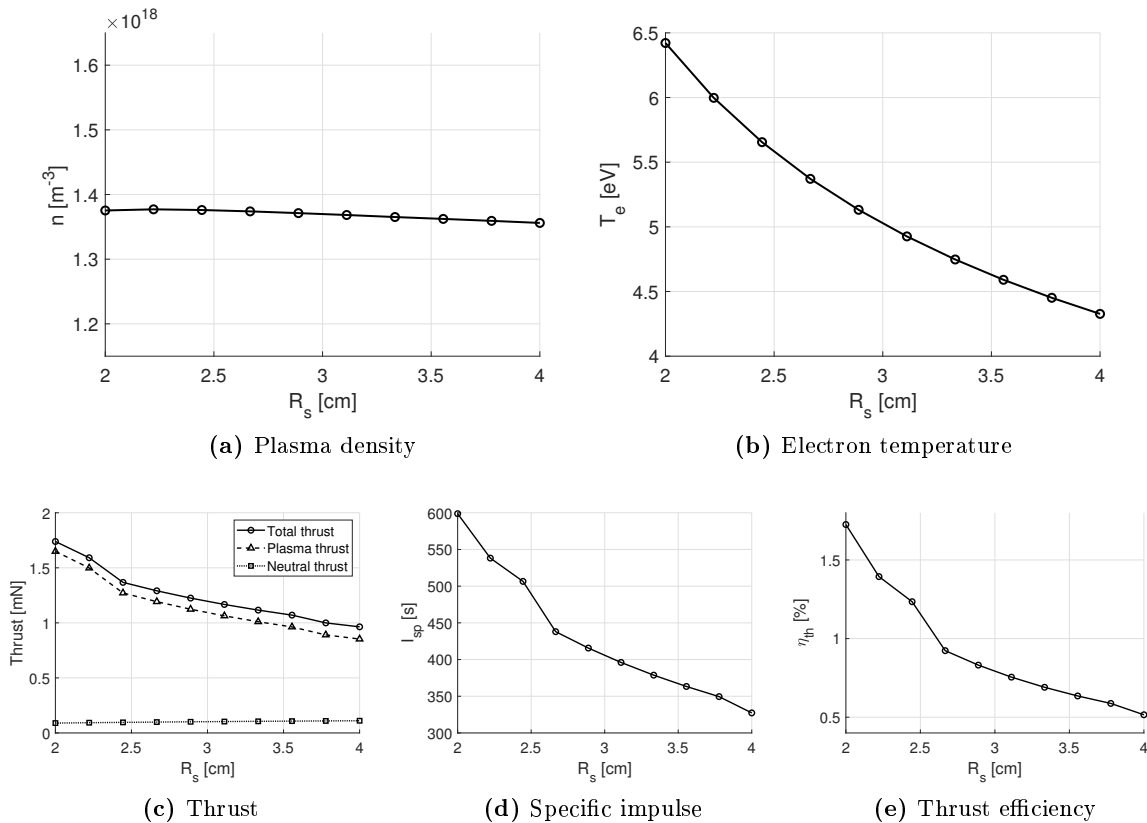


Figure 5.1: Behaviour of the plasma properties and propulsive characteristics as a function of the source radius (R_s).

As can be seen the plasma density remains roughly constant in the range of values employed. This can be justified by considering that two counteracting effects take place as the source radius increases. Indeed, the consequent enlarging of the source volume implies a lower power density that in turn should lead to a lower number of ionizations and a smaller plasma density. On the

other hand, as the source radius increases, h_R decreases as can be noticed by Eq. 2.102, leading to lower plasma losses at the radial walls and an increase in the plasma density. These two effects balance out, leaving the plasma density largely unvaried. The density of the neutrals is also fundamentally unaffected by a change in the source volume, since the equilibrium of this species depends mainly on the exhaust conditions. The decreasing behaviour of the electron temperature is also to be expected, as, albeit the slight decrease of the plasma density, the increase in volume linked to a bigger source radius implies a smaller power density. Finally the large decrease of the electron temperature has a stronger effect on the thrust than the mild variation of the plasma density, implying that, as the source radius increases the total thrust provided by the thruster decreases. The neutral thrust can instead be considered nearly constant, and over this range of values never constitutes more than 10% of the total thrust. Finally since both the mass flux passing through the thruster and the input total power are imposed constant the specific impulse and thrust efficiency are simply proportional to the total thrust.

Source Length

Nominally the source length has been fixed at 12 cm, while its effects have been evaluated over a range of values going from 5 cm to 20 cm. The effects of the variation of L_s on the plasma properties inside the source and on the propulsive characteristics of the thruster have been represented in Figure 5.2.

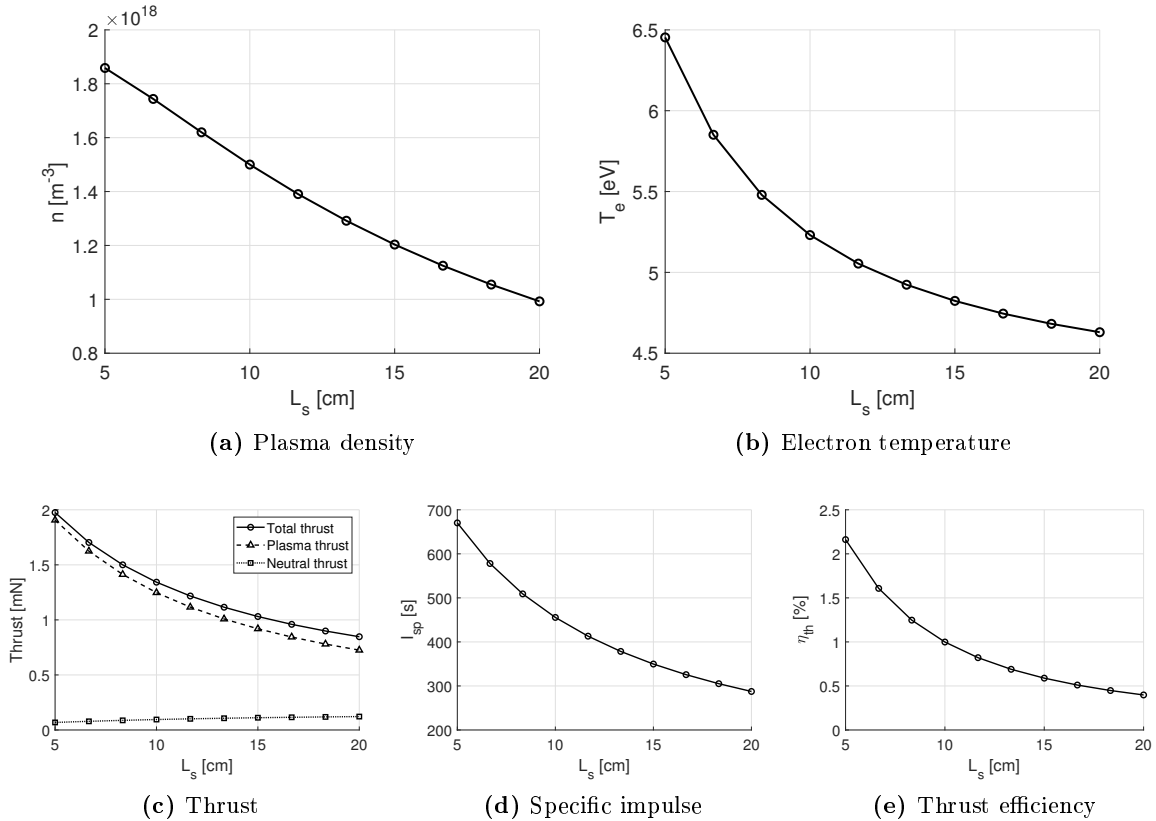


Figure 5.2: Behaviour of the plasma properties and propulsive characteristics as a function of the source length (L_s).

Again the behaviour of the plasma properties can be explained considering the increase in the lateral surface and volume of the source. Indeed the decrease in plasma density as the source length increases is due to the larger losses at the radial wall caused by the bigger loss

area. However as the source length decreases, instead, the coefficient h_L , computed through Eq. 2.103, that determines the density at the axial source boundaries becomes larger, causing bigger particle and energy losses. An optimal value of the source length is therefore expected to exist, even if outside of the considered range. On the other hand the decrease in temperature can be explained by considering that, even as the plasma density decreases the total volume increases by a larger factor, meaning that the total electron population to be heated by the electromagnetic energy enlarges. The power density therefore decreases and the electron temperature becomes smaller as the source becomes longer. Finally, since both the density and electron temperature decrease with the source length, the total thrust, which results proportional to the product of the two, behaves analogously. Again the propulsive characteristics of the thruster result directly proportional to the thrust itself, as both the input power and the mass flux have been kept constant. As for the source radius the effects of a variation in the source length depend on the values of the magnetic field and source radius itself. In case of strong magnetic confinement, for example, the losses to the radial walls are reduced, so that the increase in the area of the radial wall linked to a longer source has a smaller influence on the plasma density. On the other hand an increase in L_s generates a smaller h_L coefficient, reducing the axial losses and increasing the plasma density. These two counteracting effects therefore become comparable and an optimal value of the source length that optimises the plasma density is expected, as shown by Figure 5.3, obtained for a magnetic field of 1500 G. In any case, even for high magnetic fields, the other outputs follow behaviours similar to the one depicted in Figure 5.2, because of the only mild variation in the density shown in Figure 5.3.

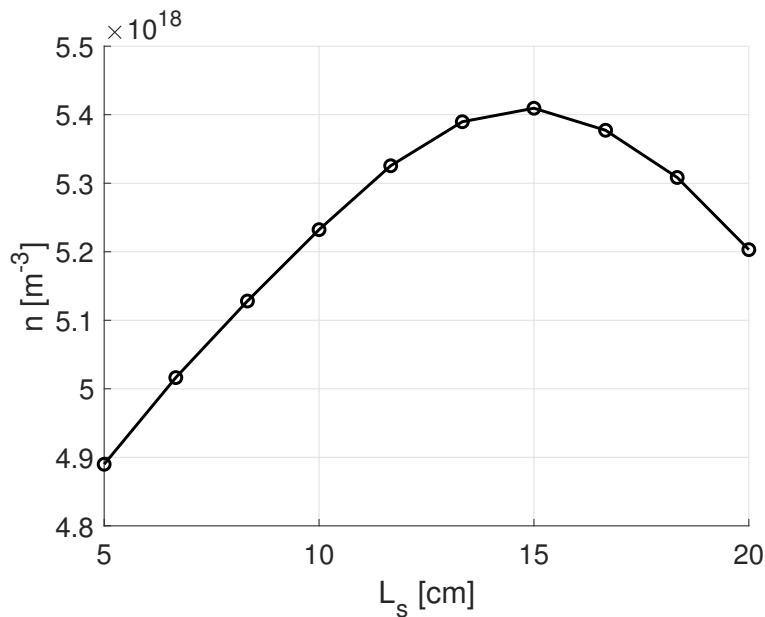


Figure 5.3: Behaviour of the plasma density (n) in function of the source length (L_s) in the case of a strong confining magnetic field $B = 1500$ G.

Exhaust Radius

The exhaust radius has been nominally fixed at a value of 2 cm and its effects have been analysed over a range going from 2 cm to 3 cm. As previously mentioned, of course, the exhaust radius cannot become bigger than R_s , meaning that its upper value is limited by the nominal source radius. The behaviour of the outputs in function of the exhaust radius can be found in Figure 5.4.

As could be expected the plasma density has been found to decrease as the exhaust section

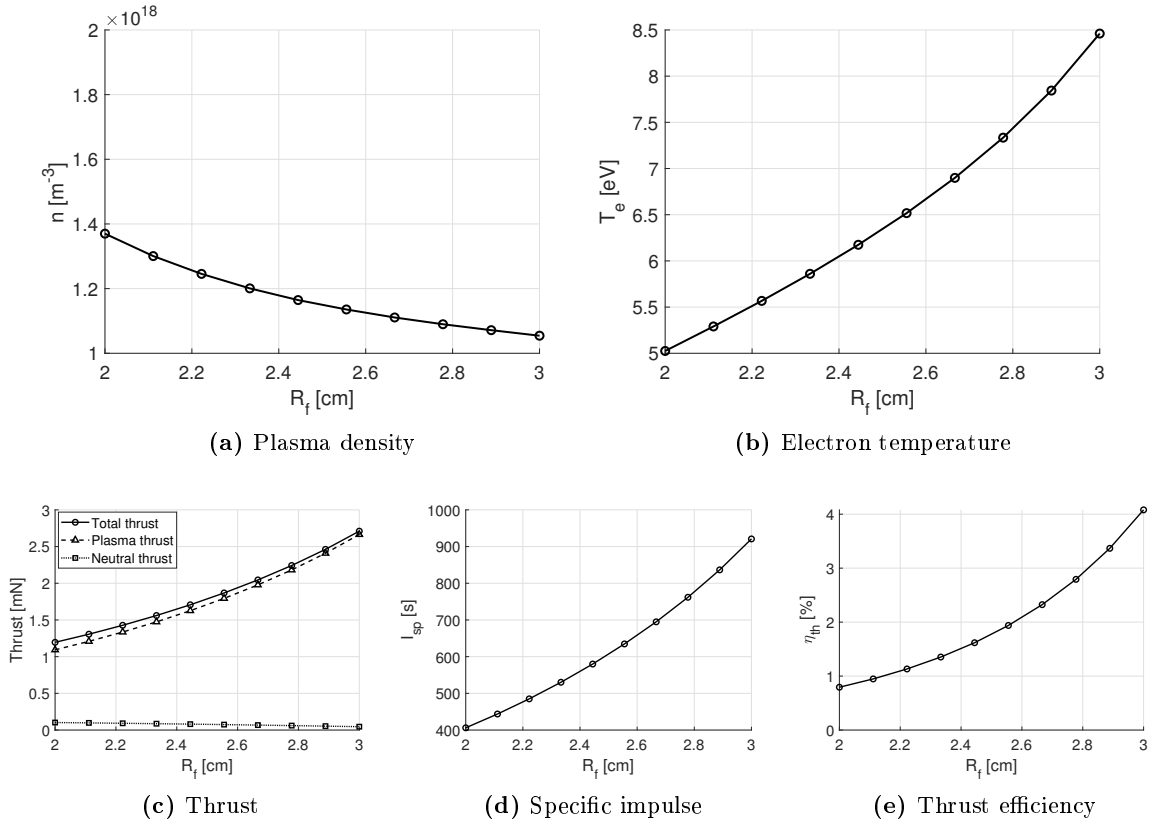


Figure 5.4: Behaviour of the plasma properties and propulsive characteristics as a function of the exhaust radius (R_f).

becomes larger, because of the greater flux of particles flowing out of the source. Similarly it has been observed that the density of the neutral particles decreases with the increase of the exhaust radius, because of the smaller neutral pressure necessary to maintain the mass flux constant in presence of a larger exhaust. This in turn contributes to the decrease of the plasma density, as it cuts down the probability of ionizing collisions. Because of this fall in the plasma density the electron temperature has instead been found to increase, due to the smaller number of electrons to be energized. It should here be noted that, as shown in panel (b) of Figure 5.4, the last three evaluation points are outside of the model limits, as the electron temperature has been found to exceed the 7 eV mark. Nevertheless, taking into account the good agreement of the reaction rate expressions with other empirical data even beyond this limit and the good continuity demonstrated with respect to the previous behaviour, the results beyond this temperature threshold have been kept in the Figure. Finally, as can be seen, the increase of the electron temperature has a bigger effect than the plasma density decrease and the propulsive properties have been found to rise as the exhaust opening becomes larger. Indeed while the decrease in the plasma density tends to cause a lower plasma mass flux the larger exhaust tends to rise this value, countering the effect of a smaller plasma density.

Mass Flux

Nominally the mass flux has been fixed at $\dot{m} = 0.3 \text{ mg s}^{-1}$, and its effects have been computed over a range of values varying from 0.15 mg s^{-1} to 0.7 mg s^{-1} . The results are shown in Figure 5.5.

As the mass flux increases the plasma density has been found to rise, as reported in panel (a). This can be explained by considering that an increase in the mass flux necessarily implies a

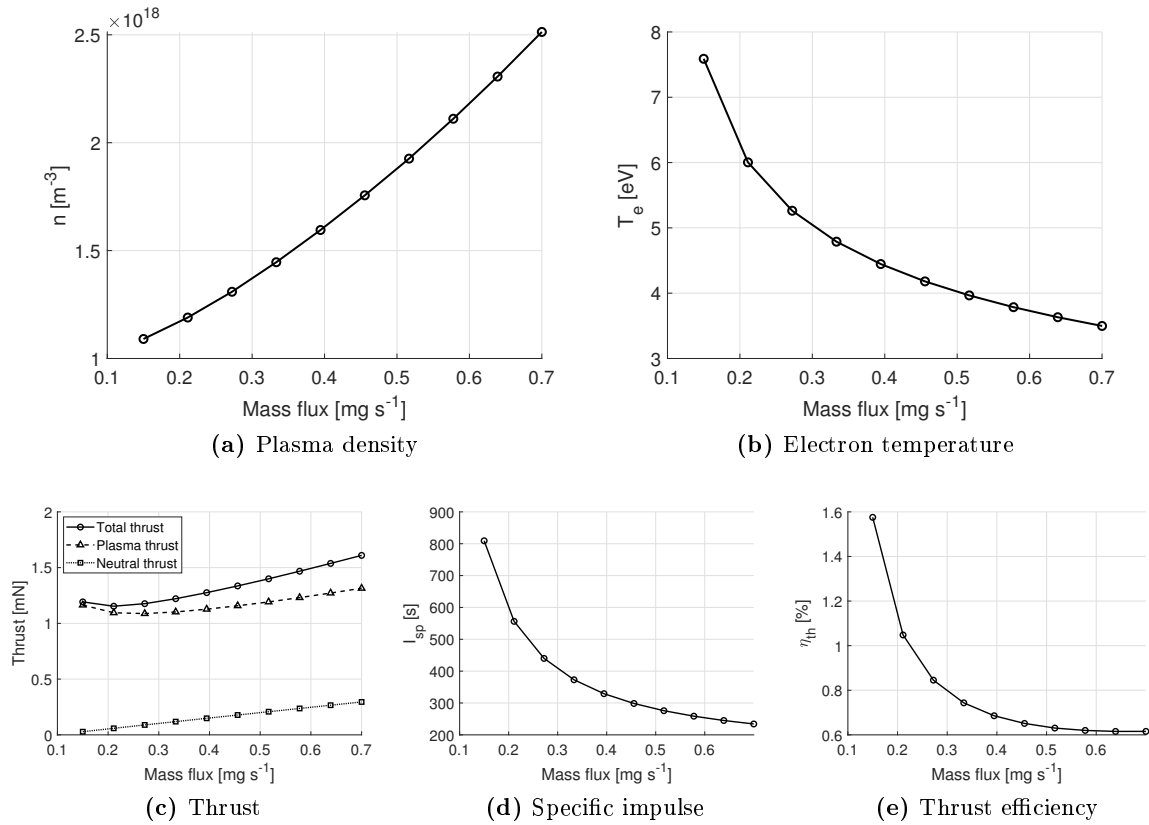


Figure 5.5: Behaviour of the plasma properties and propulsive characteristics as a function of the mass flux.

higher density of neutral atoms and therefore a larger number of ionizing collisions. The result is a bigger electron population and, consequently, a lowering of the electron temperature as \dot{m} increases, as can be observed in panel (b). The behaviour of the plasma thrust observed in panel (c) depends directly on the plasma properties found in the source, while the contribution of the neutral atoms has been found to rise due to the increase in their density. The result is a mild increase in the total thrust. On the other hand the specific impulse has been observed to decrease, due to the small variation in the thrust, its numerator, while the mass flux, proportional to the denominator, increases. The increase of the mass flux, therefore, can only be reasonably used to increase the thrust provided by the thruster in a small range of values, as a large increase \dot{m} would cause an important loss of specific impulse.

Magnetic Induction and Cusp Number

Given the strict relationship between the magnetic field inside the source and the number of cusps present in the magnetic geometry their influence on the plasma properties and propulsive characteristics of the thruster have been analysed together. The magnetic induction has been varied over a range of values going from 100 G to 700 G, and for each of these magnetic fields the model has been run considering a variable number of cusps: from 0 to 4. It should be here mentioned that a simply divergent magnetic nozzle, with magnetic induction at the throat identical to the one found in the source, has been considered for all the simulations. The results obtained are presented in Figure 5.6, where, for clarity, only the total thrust has been plotted in panel (c) taking advantage of the fact that the thrust of the neutral particles is only slightly influenced by the magnetic field and the number of cusps, with a maximum relative variation, over the full range of values considered, of only 4%.

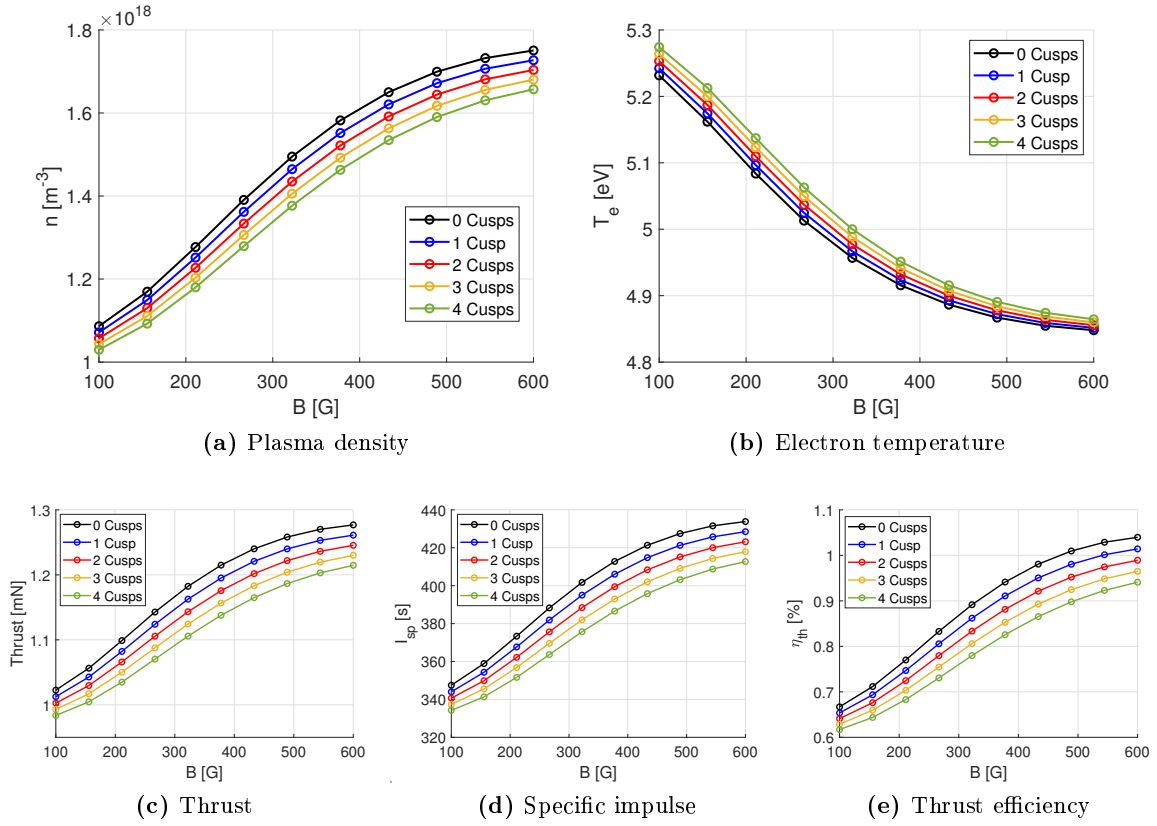


Figure 5.6: Behaviour of the plasma properties and propulsive characteristics as a function of the magnetic induction in the source (B), and parametrised by the number of cusps. In all panels the black, blue, red, orange and green lines represent the results obtained by considering respectively a magnetic geometry formed by 0, 1, 2, 3, or 4 cusps.

As can be observed in panel (a) the plasma density increases as the confining effect of the magnetic field strengthens. This result is expected, as a higher magnetic induction causes a lower radial diffusion and therefore reduced losses to the outer source walls. Likewise it can be observed that using fewer cusps increases the plasma density. The cusp regions are in fact points of higher radial diffusion in the source, since in their proximity the charged plasma particles do not have to cross the field lines to reach the walls but can move along them. If the cusps are more numerous, therefore, the total number of particles that reach the outer walls increases. As already mentioned the behaviour of the electron temperature is often found to be inverse to the one of the plasma density, as an increase in the electron population implies that the electromagnetic energy has to be subdivided over a higher number of particles, allowing a lower average temperature. Indeed, as can be seen in panel (b) the electron temperature has been observed to decrease as the magnetic induction increases and as the number of cusps decrease. It can be also noted that both at high and low magnetic fields the variation in density and temperature due to a different number of cusps starts to decrease. Indeed for a magnetic intensity of $B = 100$ G the difference between the densities computed with 0 and 4 cusps is of approximately 0.085 m^{-3} , and at $B = 600$ G the difference result roughly equal to 0.095 m^{-3} . For magnetic inductions of $B = 380$ G, where it is maximum, instead, this difference rises to 0.11 m^{-3} . This can be explained by considering that in the presence of a low magnetic induction the diffusion towards the radial walls is already quite high, meaning that the difference in radial diffusion between the points in the wall where a cusp is present and the ones where it is not becomes negligible and therefore so does the number of cusps. At high magnetic intensities, instead, the dimensions of the cusps decrease as it is proportional to the

Larmor radius of ions and electrons, leading to a smaller influence of their number. Finally it can be observed in panels (c), (d), and (e) that a higher magnetic field and a lower number of cusps lead to a better propulsive performance, because of the reduced losses at the radial walls.

Input Power

Once again to study its influence on the thruster's performance the input power has been varied over a range of values going from 10 W to 600 W. It should here be noted that, for these computations, the electromagnetic power given to the thruster has been considered perfectly coupled with the plasma, and the antenna circuit has been idealized, so that a unitary transfer efficiency from the electric power to the power absorbed by the plasma could be assumed ($\eta_{rf} = 1$). While a unitary transfer efficiency is not a physically accurate condition, as some power is always lost in the antenna circuit and in the coupling with the plasma, its influence in this analysis is negligible, as only the qualitative behaviour of the plasma and propulsive properties has been evaluated. The influence of the input power (P_T) is shown in Figure 5.7.

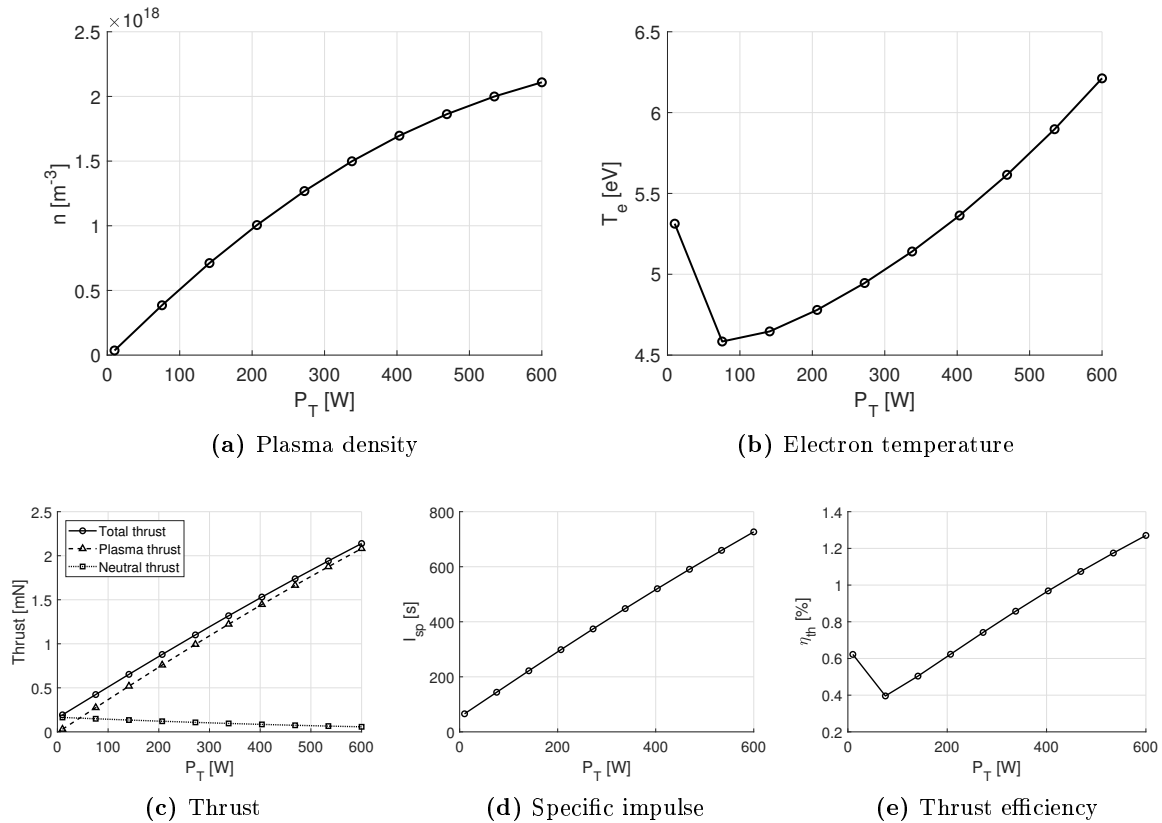


Figure 5.7: Behaviour of the plasma properties and propulsive characteristics as a function of the total power (P_T) provided to the thruster.

Once again the behaviour of the plasma properties may be explained through simple physical considerations. Indeed, in panel (a), the plasma density can be observed to increase as more power is provided, due to the larger energy available to ionize the neutral atoms. Likewise the electron temperature increases as the energy transferred into the plasma rises. The increase in electron temperature found when lowering the input power from 70 W to 10 W can be attributed to the extremely low plasma density found at these low power values (0.05 m^{-3}). This implies that most of the energy given to the plasma is stored under the form of thermal energy, but does not contribute to the ionization of the neutral atoms. As expected panel (c)

demonstrates that the total thrust increases as a higher power is offered to the thruster. It is interesting to note that at very low input powers the majority of the thrust can be attributed to the neutral particles, because, as before, of the very low plasma densities produced at these powers. As shown in panel (d) the specific impulse follows faithfully the behaviour of the total thrust as, having imposed a fixed mass flux, it results directly proportional to it. Finally the behaviour of the thrust efficiency is of particular interest in this case. Indeed, since the total input power features at the numerator of the thrust efficiency, the increasing behaviour presented in panel (e) was not guaranteed. This rise of η_{th} with the provided power implies that the energy losses in the source increase at a slower rate than the input power itself. Such a result is an encouraging sign for the attempts to produce high power cathodeless plasma thruster. The increase of the thrust efficiency found at very low powers can be attributed both to the analogous profile of the electron temperature and to the fact that, as shown in panel (c), the thrust in this region is mainly due to internal energy of the neutral particles, which has not been included in the power used to compute η_{th} .

Ion Temperature

As previously explained the ion temperature cannot be considered a design parameter. Indeed, its value cannot be externally imposed but depends on the physical processes that characterise the plasma source. However, because it is assumed in all the considered models and not derived through a physical analysis of the ion population, its influence on the model outputs has been studied, in order to better understand the consequences of this assumption. The effects of the ion temperature have therefore been analysed over a range of values spanning from 0.05 eV to 0.2 eV and the results are depicted in Figure 5.9.

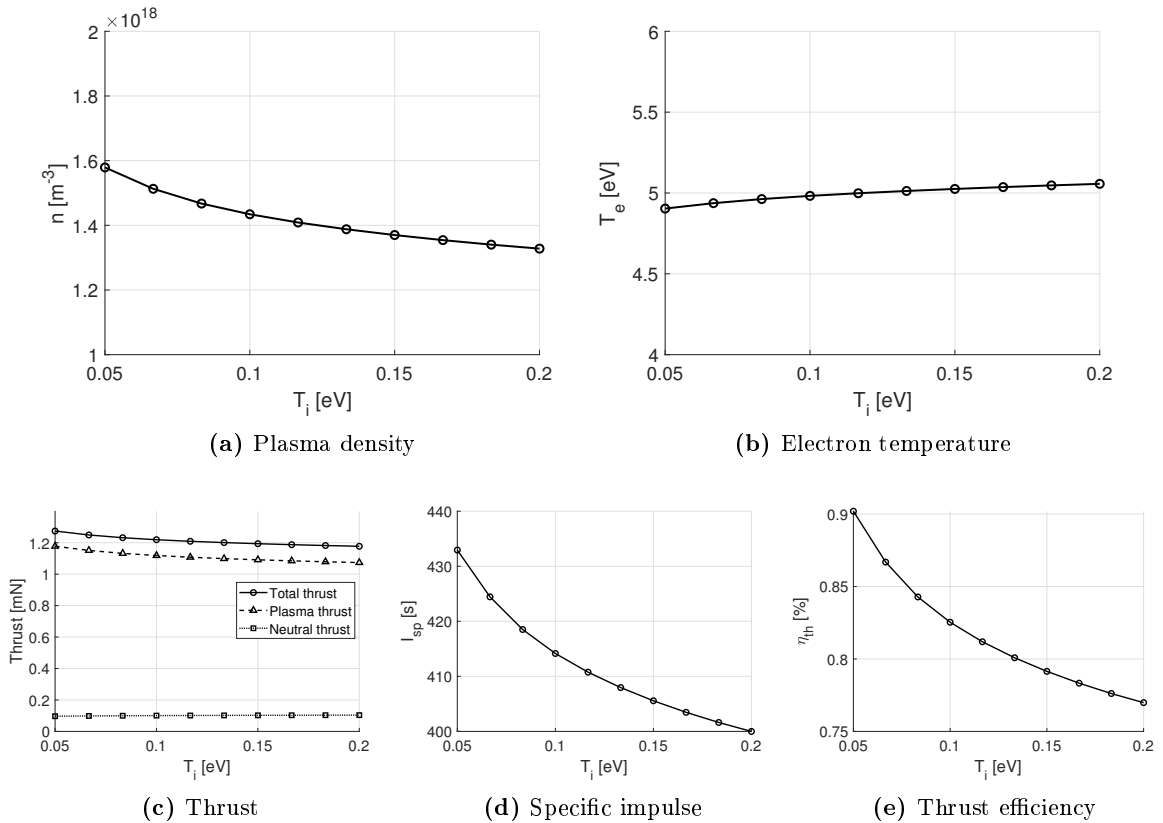


Figure 5.8: Behaviour of the plasma properties and propulsive characteristics as a function of the ion temperature (T_i) in the plasma source.

As can be seen the effect of the ion temperature on the propulsive properties of the thruster is quite mild, with a maximum thrust variation over the considered range of temperatures of 7%. Its influence on the plasma density is, instead, more relevant as it induces a maximum variation of its value of 23% over the considered range. This decrease in the plasma density as the ions heat up can be attributed to the larger diffusive capabilities that can be attributed to hotter particles. The electron temperature has instead been found to be largely independent of the ion temperature, and only slightly rises as the ion temperature increases, possibly because of the lower plasma density. Errors linked to the assumption of the ion temperature, therefore, result acceptable for the simple semi-analytical models considered, especially for the determination of the propulsive properties of the modelled thruster. If an accurate determination of the plasma density is required, instead, a deeper description of the ion population that allows a calculation of their temperature could noticeably increase the precision of the algorithms.

Neutral Temperature

Analogously to the ion temperature the temperature of the neutral particles (T_n) cannot be considered a design variable. Indeed, while a larger control on its value is possible by modifying the temperature at which the neutral gas is injected into the plasma source, the temperature of the neutrals in steady state conditions depends on their interaction with the plasma in the source. However since the models presented assume this value constant its effects have been analysed over a range of values from 300 K to 600 K, in order to shed light on its influence on the model outputs. The results have been presented in Figure 5.9

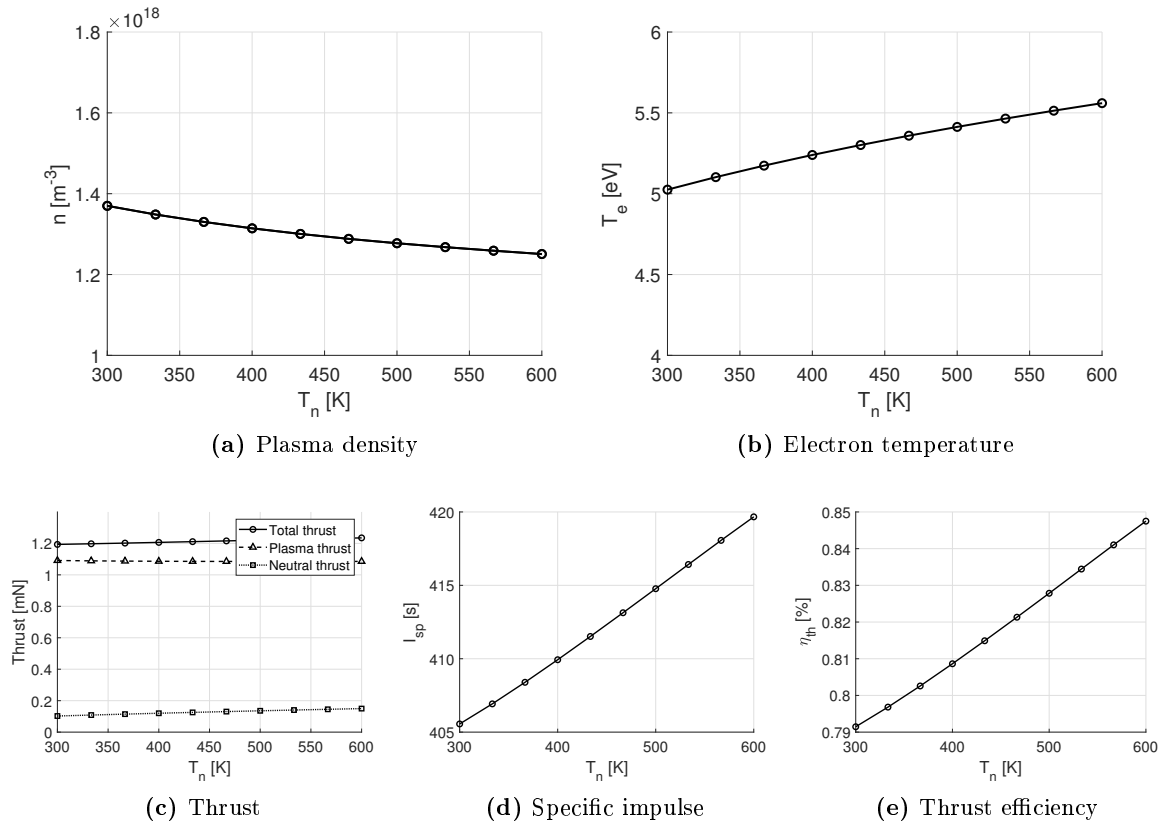


Figure 5.9: Behaviour of the plasma properties and propulsive characteristics as a function of the temperature of the neutral particles (T_n) in the plasma source.

Also in this case the effects of the neutral temperature on the propulsive properties of the thruster have been found to be negligible, with a maximum variation of the total thrust over

the full range analysed of 3.5%. The influence on the plasma properties is also quite mild, with a total variation of the plasma density of 9% and of the electron temperature of 10%. The decrease of the plasma density and the increase in electron temperature as the neutral temperature rises may be attributed to the decrease in the density of the neutral particles that this implies. In fact higher temperatures result in a higher flux of neutral particles leaving the source and reduces the density reached at equilibrium. The consequence is a lower number of ionization reactions and a lower plasma density, which in turn causes the rise of the electron temperature.

Local Sensitivity to All Design Parameters

Finally, to give a global view of the effects of the design parameters and to highlight the importance of each one with respect to the others the local sensitivity of each parameter has been computed. This quantity may be calculated for each variable by deriving a chosen output by the the parameter considered, and normalizing the result by the ratio between the output and the parameter themselves at the nominal point as shown in Equation 5.1. Here x and p are respectively the considered output and design parameter, while $S_{x/p}$ is the sensitivity of the output x on the parameter p . The subscript 0 indicates values computed at the nominal condition.

$$S_{x/p} = \frac{\left. \frac{dx}{dp} \right|_0}{\frac{x_0}{p_0}} \quad (5.1)$$

The local sensitivity may be used to understand the direct dependence of the considered outputs on the design parameters only near the nominal conditions. Indeed, due to the strongly non linear behaviour of a plasma source and nozzle and because of the cross-dependencies that link the design variables, the results of such an analysis may strongly vary according to the nominal values considered. Nevertheless using finite central differences the local sensitivity of the plasma density, electron temperature and thrust have been computed for all of the design variables. The results have been presented in Figure 5.10, normalized by the total variation computed so that the sum of the modulus of all the sensitivities is equal to one for each output.

The behaviour of each output in function of the variation of the design parameters has already been detailed in the previous paragraphs and will not be repeated. The relative dimensions of the obtained sensitivities are, instead, of higher interest. Indeed, as can be seen in Figure 5.10, for the nominal conditions considered the total thrust has been found to be mainly dependent on the radius of the exhaust (R_f), on the input power (P_T) and on the length and radius of the source (L_s and R_s). Invoking the Pareto principle [67] it can then be stated that these are the four variables to be optimized to obtain the maximum propulsive performance. In particular the input power is of easy optimization as it should be maximised, and is only limited by its upper constraints. On the other hand the source and exhaust radii and length are of more delicate determination as their optimal value depends, as shown, both on their respective dimensions and on the magnetic induction in the source. Furthermore it should be noted that an increase in the source radius loosens the upper constraints on the exhaust radius (which logically can at most be as big as the source radius), allowing bigger values and potentially inverting the relationship between R_s and the thrust. The interdependence between these two design parameters has in fact been neglected by varying them independently, in order to offer a clearer physical picture of their influence on the outputs. However R_s and R_r result strictly intertwined and their mutual dependence should be carefully considered during an optimization process. In the case of a small source radius an accurate simplifying hypothesis may consist in assuming the optimal value of the exhaust radius equal to the source radius,

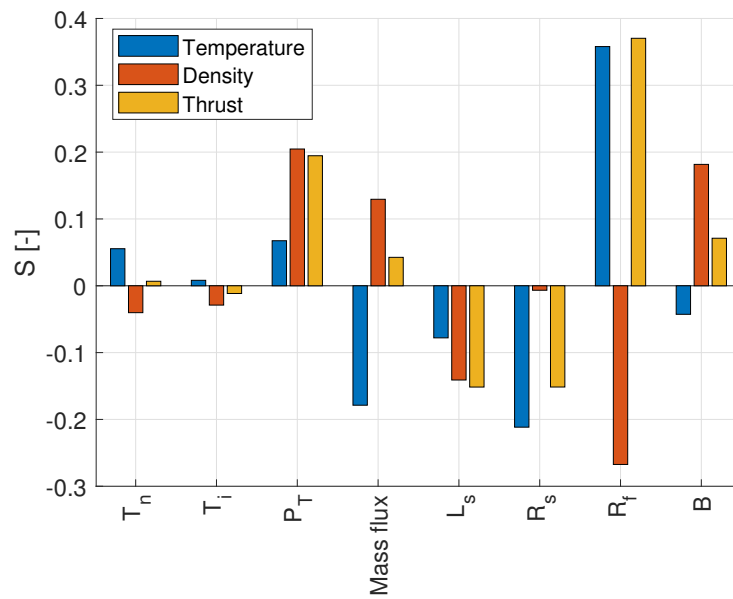


Figure 5.10: Local sensitivity (S) of the electron temperature (in blue), plasma density (in red) and total thrust (in green) on the design parameters.

decreasing the degrees of freedom of the optimization. In fact, as shown by Figure 5.4 for small source radii the propulsive performance of a thruster is found to increase with bigger exhaust sections. Finally, Figure 5.10 also shows how the temperature is mainly dependent on the mass flux, source radius (R_s) and exhaust radius (R_f), while the plasma density is predominantly influenced by the input power (P_T), exhaust radius (R_f), and magnetic field (B).

Chapter 6

Conclusions and Future Developments

6.1 Conclusions

The Global source model developed, along with the Laffleur source model, and the magnetic nozzle models considered have been found to accurately describe the physics of a cathodeless plasma thruster, in the limits of the possibilities of semi-analytical, mono-dimensional models. In particular all of the magnetic nozzle models have been observed to provide very similar results, and the choice between the alternative models has been found to depend mainly on the detachment criterion adopted. A detachment criterion capable of providing results in good agreement with the experimental data, however, has not been identified, but the most interesting alternatives found in the literature have been proposed and analysed. An algorithm that allows to determine the divergence efficiency of the thruster plume has also been developed, and its results have been shown to be in line with the expected divergence efficiency values. Finally the effects of the main design parameters of a cathodeless plasma thruster on its propulsive performance have been discussed through the use of the implemented models.

While the Laffleur source model was found to only accurately describe the force provided by the modelled thruster, the developed Global source model also resulted capable of determining the plasma properties inside the thruster, while further extending the model's capacities to magnetic topologies including cusps. When compared to higher fidelity models or experimental data this algorithm proved quantitatively accurate for a zero-dimensional, semi-analytical model with maximum relative errors of 20%. Similarly the magnetic nozzle models implemented have resulted in excellent agreement amongst themselves, especially for low ion energies, and with the experimental data, that qualitatively matches very well with the computed results. From the quantitative point of view, instead, the determination of the thrust suffers, in the worst cases, of a 40% uncertainty. This can be mainly attributed to the difficulty in the determination of the the detachment location. The detachment criteria discussed, in fact, yield very different solutions, that only occasionally correspond to the experimental data and that, however, strongly influence the computed total thrust. A more accurate study of the detachment and of the corresponding criteria results therefore fundamental in the accurate description of the thrust provided by cathodeless plasma thrusters. Finally the algorithm proposed to compute the divergence efficiency of the thrusters was found to offer acceptable solutions, albeit the difficulty found in its validation due to the lack of experimental data.

All of the models developed, and the main assumptions that they involve have been benchmarked against experimental data when possible. These however are quite scarce and of difficult retrieval, and a deeper validation campaign would greatly increase the understanding of the capabilities of the models. Likewise a more in-depth sensitivity analysis of the developed models, also including uncertainties and disturbances, would greatly help in the identification of their limits and accuracy. Finally the sensitivity analysis carried out may result useful in

the understanding of the influence of each design parameter on the propulsive properties and characteristics of a cathodeless plasma thruster. However it should be taken into account that this analysis does not consider the cross-dependencies between the design variables, that may strongly influence the model outputs. The results obtained, therefore, have a validity limited to the close surroundings of the nominal evaluation point.

6.2 Future Developments

The work presented in this thesis offers many opportunities for further study, improvement and development. A first interesting development possibility regards the proposed Global source model. Indeed the algorithm could benefit from the inclusion of the energy balance on all of the considered particle species, that would allow the computation of their respective temperatures and a more accurate determination of the plasma properties at equilibrium, as discussed in Chapter 5. Moreover the inclusion of other particle reactions, and the extension of the validity of the expressions for the reaction rates beyond 7eV would greatly benefit the model. In particular taking into account the process of radiative de-excitation for the excited atoms could noticeably influence the model results. Finally widening the spectrum of propellants that can be considered with the Global source model could greatly increase its efficacy, especially considering that one of the assets of cathodeless plasma thrusters is the ample range of propellants that can be adopted.

Another point of development that has been highlighted by the results obtained in this thesis is the study of the detachment phenomenon, and the determination of an effective detachment criteria. Indeed none of the criteria proposed and analysed in this work have been found to consistently offer a good agreement with the experimental data. On the other hand it has been shown that the detachment position greatly influences the propulsive properties of the thruster and the results offered by the adopted models. Even though this development direction is of paramount importance for the accurate modelling of the thrust obtained through a magnetic nozzle it is also extremely challenging. The detachment phenomenon has not yet, in fact, been fully understood by the scientific community, and little experimental data detailing it is available in the literature. Furthermore describing the complex nature of plasma detachment through mono-dimensional and quasi-analytical models results remarkably difficult. The use of higher fidelity bi-dimensional models to shed light onto the physics of the phenomenon and as a benchmark for simple, mono-dimensional, detachment criteria could however result highly beneficial.

A further topic of improvement can be found in the sensitivity analysis. Indeed, only the direct influence of the design parameters on the model outputs have been considered, by employing a simple One At a Time design of experiments algorithm. However the problem considered is characterized by strong interactions and cross-dependencies between the input variables, which have only lightly been touched upon. A more complete analysis of the input domain would therefore be very useful in the definition of the sensitivity of the model outputs, providing a more complete and accurate analysis to be employed for a first design of a cathodeless thruster. Variance based methods and Monte Carlo simulations could in fact take excellent advantage of the small computational times linked to the developed models and offer very interesting results in this regard.

Finally, the modelling of the antenna circuit and of the coupling of the electromagnetic waves into the plasma should also be considered to further develop and improve the models presented. In fact, while these processes have been taken into account through a simple, constant coefficient they are characterized by complex physical phenomena. Their description and modelling would therefore increase the precision and the number of information that could be derived from the source models implemented.

Bibliography

- [1] Trevor Lafleur. Helicon plasma thruster discharge model. *Physics of Plasmas*, 21(4):043507, 2014.
- [2] Manuel Martinez-Sanchez, Jaume Navarro-Cavalle, and Eduardo Ahedo. Electron cooling and finite potential drop in a magnetized plasma expansion. *Physics of Plasmas*, 22(5):053501, 2015.
- [3] Michael A Lieberman and Alan J Lichtenberg. *Principles of plasma discharges and materials processing*. John Wiley & Sons, 2005.
- [4] Christine Charles. Plasmas for spacecraft propulsion. *Journal of Physics D: Applied Physics*, 42(16):163001, 2009.
- [5] Ane Aanesland, Stéphane Mazouffre, and Pascal Chabert. Space exploration technologies pegases-a new promising electric propulsion concept. *Europhysics News*, 42(6):28–31, 2011.
- [6] Dmytro Rafalskyi and Ane Aanesland. Coincident ion acceleration and electron extraction for space propulsion using the self-bias formed on a set of rf biased grids bounding a plasma source. *Journal of Physics D: Applied Physics*, 47(49):495203, 2014.
- [7] A Fruchtman, K Takahashi, C Charles, and RW Boswell. A magnetic nozzle calculation of the force on a plasma. *Physics of Plasmas*, 19(3):033507, 2012.
- [8] Dan M Goebel and Ira Katz. *Fundamentals of electric propulsion: ion and Hall thrusters*, volume 1. John Wiley & Sons, 2008.
- [9] M Manente, F Trezzolani, M Magarotto, E Fantino, A Selmo, N Bellomo, E Toson, and D Pavarin. Regulus: A propulsion platform to boost small satellite missions. *Acta Astronautica*, 157:241–249, 2019.
- [10] Anna-Maria Theodora Andreescu, Maximilian-Vlad Teodorescu, Jeni Alina Popescu, Valeriu-Alexandru Vilag, and Adrian Stoicescu. Concept study of radio frequency (rf) plasma thruster for space propulsion. *INCAS Bulletin*, 8(4):15, 2016.
- [11] F Cannat, T Lafleur, J Jarrige, P Chabert, P-Q Elias, and D Packan. Optimization of a coaxial electron cyclotron resonance plasma thruster with an analytical model. *Physics of Plasmas*, 22(5):053503, 2015.
- [12] A Girard, D Hitz, G Melin, and K Serebrennikov. Electron cyclotron resonance plasmas and electron cyclotron resonance ion sources: Physics and technology. *Review of scientific instruments*, 75(5):1381–1388, 2004.
- [13] Alexey V Arefiev and Boris N Breizman. Theoretical components of the vasimr plasma propulsion concept. *Physics of Plasmas*, 11(5):2942–2949, 2004.
- [14] F Trezzolani, M Manente, E Toson, A Selmo, M Magarotto, D Moretto, F Bos, P De Carlo, D Melazzi, and D Pavarin. Development and testing of a miniature helicon plasma thruster. In *Proc. 35th Int. Electr. Propuls. Conf.*, pages 1–9, 2017.
- [15] Adam Shabshelowitz, Alec D Gallimore, and Peter Y Peterson. Performance of a helicon hall thruster operating with xenon, argon, and nitrogen. *Journal of Propulsion and Power*,

- 30(3):664–671, 2014.
- [16] RW Boswell and Christine Charles. The helicon double layer thruster. In *28th International Electric Propulsion Conference, IEPC*, 2003.
- [17] F Trezzolani, A Lucca Fabris, D Pavarin, A Selmo, AI Tzaglov, AV Loyan, OP Rubalov, and M Manente. Low power radio-frequency plasma thruster development and testing. In *Proceedings of 33rd International Electric Propulsion Conference, Washington, DC USA*, 2013.
- [18] F Trezzolani, M Manente, A Selmo, D Melazzi, M Magarotto, D Moretto, P De Carlo, M Pessana, and D Pavarin. Development and test of an high power rf plasma thruster in project sapere-strong. In *Proc. 35th Int. Electr. Propuls. Conf.*, pages 1–9, 2017.
- [19] Mercedes Ruiz, V Gómez, P Fajardo, J Navarro, R Albertoni, G Dickeli, A Vinci, Stéphane Mazouffre, and N Hildebrand. Hipatia: A project for the development of the helicon plasma thruster and its associated technologies to intermediate-high trls. In *71st International Astronautical Congress (IAC)–The CyberSpace Edition*, 2020.
- [20] Francesco Romano, Georg Herdrich, Peter CE Roberts, Daniel García-Almiñana, Silvia Rodríguez Donaire, and Miquel Sureda Anfres. Inductive plasma thruster (ipt) for an atmosphere-breathing electric propulsion system: design and set in operation. In *Proceedings of the 36th International Electric Propulsion Conference*, pages 1–9, 2019.
- [21] Shunjiro Shinohara, Hiroyuki Nishida, Takao Tanikawa, Tohru Hada, Ikkoh Funaki, and Konstantin P Shamrai. Development of electrodeless plasma thrusters with high-density helicon plasma sources. *IEEE Transactions on Plasma Science*, 42(5):1245–1254, 2014.
- [22] Oleg V Batishchev. Minihelicon plasma thruster. *IEEE Transactions on plasma science*, 37(8):1563–1571, 2009.
- [23] JP Sheehan, Timothy A Collard, Frans H Ebersohn, and Benjamin W Longmier. Initial operation of the cubesat ambipolar thruster. 2015.
- [24] Mirko Magarotto, Davide Melazzi, and Daniele Pavarin. 3d-virtus: Equilibrium condition solver of radio-frequency magnetized plasma discharges for space applications. *Computer Physics Communications*, 247:106953, 2020.
- [25] David B Miller and EDWARD F GIBBON. Experiments with an electron cyclotron resonance plasma accelerator. *AIAA Journal*, 2(1):35–41, 1964.
- [26] Ricky Tang. *Study of the Gasdynamic Mirror (GDM) Propulsion System*. PhD thesis, 2011.
- [27] Denis Packan, Paul-Quentin Elias, Julien Jarrige, Mario Merino Martínez, Álvaro Sánchez Villar, Eduardo Antonio Ahedo Galilea, G Peyresoubes, K Holste, P Klar, M Bekemans, et al. The "minotor" h2020 project for ecr thruster development. 2017.
- [28] Hitoshi Kuninaka, Kazutaka Nishiyama, Ikko Funaki, Tetsuya Yamada, Yukio Shimizu, and Jun'ichiro Kawaguchi. Powered flight of electron cyclotron resonance ion engines on hayabusa explorer. *Journal of Propulsion and Power*, 23(3):544–551, 2007.
- [29] Joel Christopher Sercel. *An experimental and theoretical study of the ECR plasma engine*. PhD thesis, California Institute of Technology, 1993.
- [30] Charles K Birdsall and A Bruce Langdon. *Plasma physics via computer simulation*. CRC press, 2004.
- [31] GJM Hagelaar and LC Pitchford. Solving the boltzmann equation to obtain electron transport coefficients and rate coefficients for fluid models. *Plasma Sources Science and Technology*, 14(4):722, 2005.
- [32] Frans H Ebersohn, JP Sheehan, Benjamin W Longmier, and John Shebalin. Quasi-one-dimensional code for particle-in-cell simulation of magnetic nozzle expansion. In *50th*

- AIAA/ASME/SAE/ASEE Joint Propulsion Conference*, page 4027, 2014.
- [33] Filippo Cichocki, Adrián Domínguez-Vázquez, Mario Merino, and Eduardo Ahedo. Hybrid 3d model for the interaction of plasma thruster plumes with nearby objects. *Plasma Sources Science and Technology*, 26(12):125008, 2017.
- [34] Eduardo Ahedo and Mario Merino. Two-dimensional supersonic plasma acceleration in a magnetic nozzle. *Physics of Plasmas*, 17(7):073501, 2010.
- [35] AD Cheetham and JP Rayner. Characterization and modeling of a helicon plasma source. *Journal of Vacuum Science & Technology A: Vacuum, Surfaces, and Films*, 16(5):2777–2784, 1998.
- [36] Franco Javier Bosi. Development of global models of plasma systems for space propulsion. 2016.
- [37] Pascal Chabert, J Arancibia Monreal, Jérôme Bredin, Lara Popelier, and Ane Aanesland. Global model of a gridded-ion thruster powered by a radiofrequency inductive coil. *Physics of Plasmas*, 19(7):073512, 2012.
- [38] Alexey V Arefiev and Boris N Breizman. Ambipolar acceleration of ions in a magnetic nozzle. *Physics of Plasmas*, 15(4):042109, 2008.
- [39] Christopher S Olsen, Maxwell G Ballenger, Mark D Carter, Franklin R Chang Diaz, Matthew Giambusso, Timothy W Glover, Andrew V Ilin, Jared P Squire, Benjamin W Longmier, Edgar A Bering, et al. Investigation of plasma detachment from a magnetic nozzle in the plume of the vx-200 magnetoplasma thruster. *IEEE Transactions on Plasma Science*, 43(1):252–268, 2014.
- [40] T Lafleur, F Cannat, J Jarrige, PQ Elias, and D Packan. Electron dynamics and ion acceleration in expanding-plasma thrusters. *Plasma Sources Science and Technology*, 24(6):065013, 2015.
- [41] SA Andersen, Vagn Orla Jensen, P Nielsen, and N D’Angelo. Continuous supersonic plasma wind tunnel. *The Physics of Fluids*, 12(3):557–560, 1969.
- [42] TA Collard and BA Jorns. Magnetic nozzle efficiency in a low power inductive plasma source. *Plasma Sources Science and Technology*, 28(10):105019, 2019.
- [43] Daniele Pavarin, Fernando Ferri, M Manente, D Curreli, Y Guclu, D Melazzi, D Rondini, S Suman, J Carlsson, Cristina Bramanti, et al. Design of 50 w helicon plasma thruster. In *31st International Electric Propulsion Conference*, volume 20. Ann Arbor Michigan, USA, 2009.
- [44] S Correyero Plaza, Julien Jarrige, Denis Packan, and Eduardo Ahedo. Ion acceleration in the magnetic nozzle of an ecr thruster: Comparison of experimental measurements with a quasi 1d kinetic model. In *Space Propulsion 2018*, 2018.
- [45] Ronald W Moses Jr, Richard A Gerwin, and Kurt F Schoenberg. Resistive plasma detachment in nozzle based coaxial thrusters. In *AIP Conference Proceedings*, volume 246, pages 1293–1303. American Institute of Physics, 1992.
- [46] EB Hooper. Plasma detachment from a magnetic nozzle. *Journal of Propulsion and Power*, 9(5):757–763, 1993.
- [47] Alexey V Arefiev and Boris N Breizman. Magnetohydrodynamic scenario of plasma detachment in a magnetic nozzle. *Physics of Plasmas*, 12(4):043504, 2005.
- [48] W Cox, C Charles, RW Boswell, and R Hawkins. Spatial retarding field energy analyzer measurements downstream of a helicon double layer plasma. *Applied Physics Letters*, 93(7):071505, 2008.
- [49] Mario Merino and Eduardo Ahedo. Plasma detachment in a propulsive magnetic nozzle via ion demagnetization. *Plasma Sources Science and Technology*, 23(3):032001, 2014.

- [50] Justin M Little and Edgar Y Choueiri. Thrust and efficiency model for electron-driven magnetic nozzles. *Physics of Plasmas*, 20(10):103501, 2013.
- [51] Are Mjaavatten. Curvature of a 1d curve in a 2d or 3d space. MATLAB Central File Exchange. URL:<https://www.mathworks.com/matlabcentral/fileexchange/69452-curvature-of-a-1d-curve-in-a-2d-or-3d-space>.
- [52] Alexey Vladimirovich Arefiev. *Theoretical studies of the VASIMR plasma propulsion concept*. PhD thesis, 2002.
- [53] Kazunori Takahashi, Trevor Lafleur, Christine Charles, Peter Alexander, and Rod W Boswell. Electron diamagnetic effect on axial force in an expanding plasma: experiments and theory. *Physical review letters*, 107(23):235001, 2011.
- [54] N Sharma, M Chakraborty, NK Neog, and M Bandyopadhyay. Development and characterization of a helicon plasma source. *Review of Scientific Instruments*, 89(8):083508, 2018.
- [55] T Lafleur, K Takahashi, C Charles, and RW Boswell. Direct thrust measurements and modelling of a radio-frequency expanding plasma thruster. *Physics of Plasmas*, 18(8):080701, 2011.
- [56] Eduardo Ahedo and Manuel Martínez Sánchez. The role of current-free double-layers in plasma propulsion. In *44th AIAA/ASME/SAE/ASEE Joint Propulsion Conference & Exhibit*, page 5005, 2008.
- [57] AV Phelps and Z Lj Petrovic. Cold-cathode discharges and breakdown in argon: surface and gas phase production of secondary electrons. *Plasma Sources Science and Technology*, 8(3):R21, 1999.
- [58] Ioannis Mikellides, Ira Katz, Myron Mandell, and J Snyder. A 1-d model of the hall-effect thruster with an exhaust region. In *37th Joint Propulsion Conference and Exhibit*, page 3505, 2001.
- [59] GJM Hagelaar and LC Pitchford. Solving the boltzmann equation to obtain electron transport coefficients and rate coefficients for fluid models. *Plasma Sources Science and Technology*, 14(4):722, 2005.
- [60] S.F. Biagi. Biagi database. LXcat. URL:www.lxcat.net/Biagi.
- [61] François Vidal, Tudor Wyatt Johnston, Joëlle Margot, Mohamed Chaker, and Olivier Pauna. Diffusion modeling of an hf argon plasma discharge in a magnetic field. *IEEE transactions on plasma science*, 27(3):727–745, 1999.
- [62] Kazunori Takahashi, Daiki Sato, Koichi Takaki, and Akira Ando. Development of a compact magnetically expanding plasma source with a strong magnetic field. *Plasma Sources Science and Technology*, 22(5):055002, 2013.
- [63] Jón Tómas Guðmundsson. *Notes on the electron excitation rate coefficients for argon and oxygen discharge*. Raunvísindastofnun Háskólans.
- [64] M. Hayashi. Hayashi database. LXcat. URL:www.lxcat.net/Hayashi.
- [65] O. Zatsarinny and K. Bartschat. Bsr database. LXcat. URL:www.lxcat.net/BSR.
- [66] Mirko Magarotto, Marco Manente, Fabio Trezzolani, and Daniele Pavarin. Numerical model of a helicon plasma thruster. *IEEE Transactions on Plasma Science*, 48(4):835–844, 2020.
- [67] Rosie Dunford, Quanrong Su, and Ekraj Tamang. The pareto principle. 2014.